Neural Interfacing with Dorsal Root Ganglia: Anatomical Characterization and Electrophysiological Recordings with Novel Electrode Arrays

by

Zachariah Sperry

A dissertation submitted in partial fulfillment
of the requirements for the degree of
Doctor of Philosophy
(Biomedical Engineering)
at the University of Michigan
2019

Doctoral Committee:

Associate Professor Timothy M. Bruns, Chair
Associate Professor Cynthia A. Chestek
Assistant Professor Scott F. Lempka
Associate Professor Parag G. Patil
Assistant Research Scientist John P. Seymour

Zachariah Sperry

zsperry@umich.edu

ORCID iD: 0000-0002-5219-4965

Dedication

This thesis is dedicated to the memory of my uncle, Pete Aumann. A scientist and mathematician, Uncle Pete was a cerebral man who found great joy in learning and teaching others. He taught me to play and enjoy chess, to patiently engage with challenging mental puzzles, and to take up every opportunity to use my mind for the improvement of our world. He was proud of me pursuing my doctorate, because he knew it would teach me the kind of persistence and scholarship that he so valued. But my uncle also faced many challenges in his life, including bipolar disorder and Crohn's disease, and he died as I was completing this degree. The diseases he suffered from have no cure today, but the knowledge I have gained as a biomedical engineer gives me hope that one day we will overcome the obstacles in our way. Even within the particular field of neural engineering, promising new therapies are being proposed and developed every year for his particular conditions. As the next chapter of my career begins, I am excited to be a part of these discoveries, and to provide real solutions for people like Uncle Pete. For all the trials he faced, he persisted in his motto "Get busy living!" In his memory, I plan to do just that.

Acknowledgements

No research thesis is completed in a vacuum. This work would not have been possible without the incredible support and encouragement of my wife Christine, who moved to Michigan from Minnesota so I could complete this degree. I also want to acknowledge my parents and sisters, who have always supported, believed in and inspired me to be the best biomedical engineer I can be.

I would also like to thank the members of the Peripheral Neural Engineering and Urodynamics Laboratory (pNEURO Lab), particularly my fellow graduate students (Aileen Ouyang, Lauren Zimmerman, Ahmad Jiman, and Elizabeth Bottorff) and my PhD advisor Dr. Tim Bruns. Other critical collaborators include Dr. Scott Lempka, Dr. John Seymour, Dr. Euisik Yoon, Dr. Hillel Chiel, Dr. Paras Patel, Robert Graham, Anastasia Ostrowski, Grant Kulik, Nicholas Peck-Dimit, and Michelle Frazier. My summer internship was funded and supported by Medtronic's Pelvic Health and Gastric Therapies team, including Dr. Lance Zirpel and Dr. Katie Bittner. I am also grateful to my doctoral committee members for their guidance throughout this process.

Research reported in this work was supported by the Craig H. Neilsen Foundation (Grant # 314980) and by the National Institute of Biomedical Imaging and Bioengineering of the National Institutes of Health (Grant # U18EB021760), the Michigan Institute for Clinical &

Health Research, which is funded by the National Center for Advancing Translational Studies of the National Institutes of Health (Grant #'s UL1TR000433 and UL1TR002240), the National Science Foundation (Award # 1653080), Seed Funding for Innovative Projects in Neuroscience from the Michigan Brain Initiative Working Group (MiBrain), and the Rackham Predoctoral Fellowship Program. The content is solely the responsibility of the author and does not necessarily represent the official views of the funding organizations.

Table of Contents

List of Tables

List of Figures

List of Appendices

Abstract

Dorsal root ganglia (DRG), the hubs of neurons conducting sensory information into the spinal cord, are promising targets for clinical and investigative neural interface technologies. DRG stimulation is currently a tertiary therapy for chronic pain patients, which has an estimated prevalence of 11-40% of adults in the United States. In pre-clinical studies, combined neural recording and stimulation at DRG has been used as part of closed-loop systems to drive activity of the limbs and the urinary system. This suggests a role for clinical DRG interfaces to assist, among other patient groups, the nearly 300,000 spinal cord injured patients in the United States.

To maximize the utility of DRG interfaces, however, there remains a strong need to improve our understanding of DRG structure. Neural interface technologies for both stimulation and recording rely heavily on the spatial organization of their neural targets. To record high-fidelity neural signals, a microelectrode must be placed within about 200 μm of a neural cell body. Likewise, effective neural stimulation is believed to act on a subset of DRG axons based on their size and target. The spatial organization of DRG, however, has not been previously quantified. In this thesis, I demonstrate a novel algorithm to transform histological cross-sections of DRG to a normalized circular region for quantifying trends across many

samples. Using this algorithm on 26 lumbosacral DRG from felines, a common preclinical DRG model, I found that the highest density of neural cell bodies was in the outer 24% radially, primarily at the dorsal aspect. I extended this analysis to a semi-automated cross-DRG analysis in 33 lower lumbar DRG from 10 human donors. I found that the organization of human DRG was similar to felines, with the highest density of cell bodies found in the outer 20-25% of the DRG, depending on spinal level. I also found a trend toward lower small-axon density at the dorsal aspect of L5 DRG, a key region for stimulation applications.

To take advantage of this quantitative knowledge of DRG organization, future neural interfaces with DRG will require more advanced technologies. Standard silicon-based electrode arrays, while useful for short-term DRG recordings, ultimately fail in chronic use after several weeks as a result of mechanical mismatch with neural tissue. In this thesis, I demonstrate sensory recording from the surface and interior of sacral DRG during acute surgery using a variety of flexible polyimide microelectrode arrays 4-μm thick and minimum site separation 25 to 40 μm. Using these arrays, I recorded from bladder and somatic afferents with high fidelity. The high density of sites allowed for neural source localization from surface recordings to depths 25 to 107 μm. This finding supports the anatomical analysis suggesting a high density of cell bodies in the dorsal surface region where the surface array was applied. The high site density also allowed for the use of advanced signal processing to decrease analysis time and track neural sources during movement of the array which may occur during future behavioral experiments.

This thesis represents significant advances in our understanding of DRG and how to interface with them, particularly related to the way anatomy can inform development of future

technologies. Going forward, it will be important to expand the anatomical maps based on organ function and to test the novel flexible arrays in chronic implant experiments.

Chapter 1

Introduction

Human history is in many ways a continuous narrative of frontier exploration, from Polynesian sailors navigating the Pacific 6,000 years ago to more recent forays into Earth's atmosphere and beyond. No matter the frontier, crossing the boundary between the known and unknown requires the development of, and a dialog between, maps and vehicles. Whether star knowledge guiding outrigger canoes to new islands or orbital physics guiding rockets to the Moon, no exploration can succeed without the right vessel and the right map. The human nervous system with all its scientific mystery and medical promise is a true modern frontier. The motivation behind this thesis was the development of new anatomical maps and bioelectrical vehicles to explore a small but significant corner of this frontier: the dorsal root ganglia.

As nerves branch off from the spinal cord at each spinal level, they are initially segregated within the spinal root into dorsal and ventral regions containing sensory or motor axon, respectively. Primary sensory neurons in the dorsal spinal root are psueudounipolar, meaning they consist of a single long axon stretching from the cord to a peripheral target, with the cell body connected the main axon at a T-junction. These cell bodies are contained within a region of the dorsal root called the dorsal root ganglion (DRG), and range in size from about 20

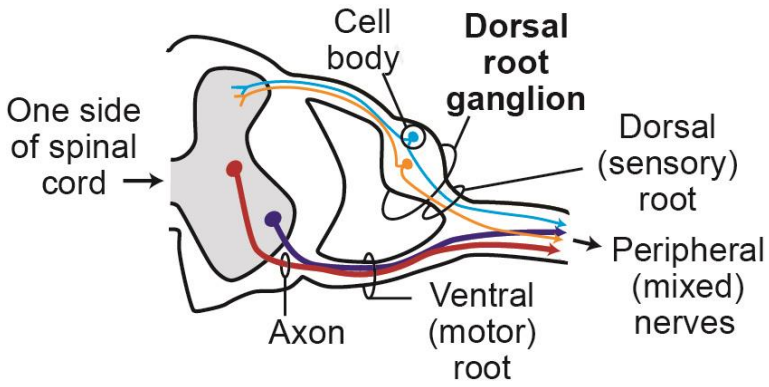

FIGURE 1: Diagram showing transverse section of spinal cord and roots, dorsal side up. Pseudounipolar sensory neurons are depicted traversing the dorsal root, with cell bodies in the dorsal root ganglion (DRG).

to 100 µm in diameter, depending on fiber type [1]. The axons range in size from 0.2 to 20 µm in diameter, with small unmyelinated C-fibers having the smallest diameter (0.2-1.5 µm) and myelinated Aα-fibers having the largest (12-20 µm). DRG also contain satellite glial cells surrounding the neural somata, though their role in environmental maintenance and cell-to-cell communication is not yet well understood [2], [3]. The DRG and ventral root (VR), which contains motor axons, are surrounded and separated by a layer of connective epineurial tissue. FIGURE 1 depicts the DRG with reference to the spinal cord and roots.

DRG interfaces are presently used as a third-line clinical treatment for chronic pain, which affects an estimated 1.5% of the population [4], [5]. Stimulation applied with a large lead (contact area on the order of 1 mm^2) near the DRG appears to show greater pain relief than a similar lead applying more conventional spinal cord stimulation and allows for a reduction in pain medication. However the overall effect of >50% pain relief in ~80% of patients still leaves room for improvement [4].

While not currently in clinical use, targeted DRG neural interfaces using microelectrodes (contact area on the order hundreds of μm^2) of have the potential to restore function to some

of the approximately 17,000 patients who suffer an SCI each year [5]. While an SCI patient's most visible symptom may be limb paralysis, equal or higher priority is often given by patients to development of new therapies addressing impairment of respiratory, bladder, bowel, or sexual functions [6], [7]. Significant effort in the field of neural stimulation has been directed toward functional solutions for SCI patients, and microstimulation of DRG could contribute to this effort by using the same neural interface technology for recording to selectively activate primary somatosensory afferents, a step towards restoring sensation [8]–[11], and providing modulation of bladder pressure through activation of spinal reflex pathways [12], [13]. DRG recording and decoding has been previously demonstrated in animal studies both acutely and chronically for monitoring skin sensation, limb position, and bladder pressure using penetrating microelectrode arrays inserted into DRG, sometimes as sensory feedback for stimulation applications [13]–[20]. As action potentials propagate from the periphery through the main axon of a DRG neuron, they also enter the unmyelinated cell body and generate a large current sink that can be detected with microelectrodes within about 100-200 μm [21]. While SCI represents perhaps the most obvious therapy target for this DRG microelectrode interface, patients with non-SCI pathologies (ex. bladder dysfunction, fecal incontinence, peripheral neuropathy) could also benefit.

DRG interfaces also have value in advancing our understanding of neurophysiology. The physiology of complex autonomic and reflex circuits, such as those of the bladder and gut, involves many different neurons across several distinct nerves. Separately accessing each nerve can be unwieldy. In contrast, the DRG at each spinal level serves as a nexus for multiple nerves and therefore allows access to many different neuron types at a single location. Some of the

nerves and nerve plexi of the autonomic system (including the pelvic plexus) are challenging to interface with because of their very small size peripherally before they join at the spinal root. A DRG interface could mitigate this problem.

Detailed anatomical information about the neural target is required in order to guide the development of any neurotechnology, including DRG interfaces for clinical or research use. Studies of DRG anatomy typically focus either on gross morphology or on fiber counts and sizes related to different neuron types. In human DRG, for instance, cadaver dissections and *in vivo* imaging studies have been used to define DRG lengths, diameters, and offshoot angles at all spinal levels [22]–[27], generally with motivation related to the development or treatment of pathological pain. A number of studies have also used automated or manual histological analysis to count human DRG nerve fibers and cell bodies, sometimes by size, across different spinal levels [28]–[30]. There is an intermediate gap in the literature, however, when it comes to describing quantitatively the spatial organization of cells within human DRG. A few older texts make reference to a "central fiber stream" of DRG axons or to superficial cell bodies, implying a predominance of cell bodies around the dorsal edge, but no further analysis is made [31], [32]. Some animal studies (rats and felines, primarily) have attempted to address this gap with nerve tracing or electrophysiological recordings. These studies have suggested a variety of topographies and somatotopies within the DRG, including most commonly a rostral-caudal organization reflecting the location of receptive fields and spinal cord targets [33]–[37]. These studies were often contradictory, however, and overall maps describing cell body and axon density within DRG are still missing from the literature.

Maps like these would be useful for the development of new interface technologies with DRG. Neural recording at the single-unit level requires the placement of electrodes within about 150-200 μm of the cell body of interest [38], [39]. While the number and density of recording channels available for neural recording is increasing as technology improves, targeting electrode sites to regions with a high density of cell bodies could be a strategy to maximize the types of signals recorded. Maps of cell body location could also inform the development of alternative recording methods, such as DRG surface recording [40], [41]. Axon maps would more likely have an impact on the design of stimulation technologies. Models of clinical DRG stimulation suggest that it causes action potential generation starting in axon segments, except in the specific case of cathodic C-fiber stimulation with potentials starting in the soma [42]. They also suggest that within typical clinical ranges (0.2-1 μA), fiber activation is highly dependent on fiber size (Aβ fibers [6-12 μm] preferentially activated over C-fibers), and effective stimulus may only penetrate about 2 mm into the dorsal surface of the DRG [42]. Models of DRG microstimulation using penetrating electrodes, in contrast, suggest that small fibers can be recruited at low currents (<10 μA) within 200 μA [43]. For either type of stimulation, if the spatial distribution of fiber and cell body types is non-random, then a map would be a useful tool to predict and design for the desired outcome.

Chapters 2 and 3 of this thesis are concerned with quantitative mapping of the spatial densities of neurons in lumbosacral DRG. Chapter 2 focuses on methodological development and exclusively describes cell bodies in medial cross-sections of lumbosacral feline DRG. Chapter 3 builds on this analysis with improved and automated analyses to describe cell body and axon densities across the length of human L4 and L5 DRG. The key finding of these chapters

was that both species' DRG had the highest density of neural cell bodies in the dorsal outer 25%, which has implications for the design of future neural interfaces for both stimulation and recording.

In the second half of this thesis, my goal was to leverage and extend the histological mapping to electrophysiological recordings using novel microelectrode arrays. Most studies in DRG utilize penetrating microelectrode arrays, often Utah arrays inserted into the tissue with a pneumatic insertion tool [8], [9], [18], [19], [44], [45], [10]–[17]. While effective for limited recording periods (up to a few months in chronic DRG studies [10], [13]), these electrodes have several shortcomings. First, penetrating arrays have the potential to cause tissue damage and encapsulation, thought to be the result of damage caused by the initial insertion and, more importantly, by micromotion of the very stiff silicon electrodes relative to the neural tissue [46]–[48]. Second, we must consider the observation that the majority of DRG cell bodies are localized around the DRG periphery, particularly at the dorsal aspect below a sub-100 μm thick epineurium [49], [50]. Utah array electrodes sample from a single depth with each shank, and commercial models are inserted below this potentially critical region.

These problems may be overcome with the application of a high-density flexible recording interface, either at the DRG surface or inserted with a temporary shuttle. Polymer substrates serve as better mechanical matches to neural tissue and have been used for insertion into peripheral nerves as intrafascicular recording arrays [51]–[53]. The biocompatibility benefits of thin flexible devices are increasing their prominence in the field of neural interfaces, though issues of water intrusion, delamination, and securement still need to be solved for chronic use [54]. While a previous set of experiments demonstrated surface

single- and multi-unit neural recording from DRG, the arrays used were not based on a flexible interface and required downward pressure to detect neural signals [40], [41].

With improvements in microfabrication techniques, it is now possible to produce high site-count high-density implantable microelectrode arrays, in some cases approaching or exceeding 1000 sites with site spacing on the order of 20 μm, though these arrays have so far utilized a stiff silicon backing and have not yet been utilized in DRG recording and typically do not record from all sites in parallel [55], [56]. High-density recording arrays have several advantages over their low-density counterparts. Most obviously, high-density probes can sample at more locations in a given tissue volume, potentially increasing the number of neurons which can be observed. Additionally, electrode site spacing on the order of neural cell diameters can record from a single unit with high fidelity on multiple sites, allowing for triangulation of neurons [57] and tracking their location over time if the array shifts in acute or chronic experiments [55]. New automated software tools are needed in order to take advantage of these capabilities in the very large data sets that result from high-density, and a variety are now available in open source packages [58]–[60].

Chapters 4 and 5 of this thesis are concerned with neural recording from feline DRG using novel high-density flexible polyimide arrays in acute anesthetized procedures. Chapter 4 focuses on recording single-unit activity from the surface of DRG, using invertebrate ganglia as an additional high-throughput testbed. Chapter 5 focuses on implant of arrays into the DRG interior with shuttles and novel analysis of high-density DRG signals using specialized neural spike sorting software. The key finding of these chapters was that recording and oversampling

of neural potentials with high density arrays can be used to map sensory modalities within DRG, which could be used to target future research and therapies.

Overall, this thesis provides several significant advances in our understanding of DRG anatomy and how to successfully interface with them using high-density microelectrodes. My analyses of DRG spatial anatomy and electrophysiology contain important implications for the design of future clinical and research interfaces with this important neural site. While future studies of DRG will surely enhance the maps and tools presented herein, research like this will continue to play an important role in exploring the great modern frontier presented by the human nervous system.

Chapter 2

Quantitative Models of Feline Lumbosacral Dorsal Root Ganglia Neuronal Cell Density

(previously published in the Journal of Neuroscience Methods, October 2017 [49])

Abstract

Dorsal root ganglia (DRG) are spinal root components that contain the cell bodies of converging primary sensory neurons. DRG are becoming a therapeutic target for electrical neural interfaces. Our purpose was to establish methods for quantifying the non-random nature and distribution of neuronal cell bodies within DRG. We identified neuronal cell body locations in 26 feline lumbosacral DRG cross-section histological images and used computational tools to quantify spatial trends. We first analyzed spatial randomness using the nearest-neighbor distance method. Next we overlaid a 6 × 6 grid, modeling neuronal cellular density in each grid square and comparing regions statistically. Finally, we transformed DRG onto a polar map and calculated neuronal cellular density in annular sectors. We used a recursive partition model to determine regions of high and low density and validated the model statistically. We found that the arrangement of neuronal cell bodies at the widest point of DRG is distinctly non-random with concentration in particular regions. The grid model suggested a radial trend in density, with increasing density toward the outside of the DRG. The polar transformation model showed

that the highest neuronal cellular density is in the outer 23.9% radially and the dorsal ±61.4° angularly. To our knowledge, DRG neuronal cell distribution has not been previously quantified.

Introduction

The dorsal root ganglion (DRG) is a part of the spinal root which contains the cell bodies of converging peripheral sensory neurons. DRG offer a potential neural interfacing location for prosthetics and physiology studies that aim to interact solely with sensory neurons. Although DRG have been well-studied overall, few studies have quantitatively investigated the cell-body distribution of DRG. Anatomical analyses of DRG are dominated by morphological studies of human and animal roots.

Human studies focus on the overall size and alignment of DRG in cadaver dissections [22], [61], [62] fixed specimens [63], and imaging studies [25]–[27], generally towards clinical pain applications.

The majority of animal studies have focused on characteristics of individual DRG neurons, such as conduction velocity and action potential generation [64]. In addition to studying DRG anatomy and characteristics of individual neurons [50], [65]–[67], animal studies have included population-based analysis of DRG neurons which have provided insight into total cell counts [68]–[70], relative ratios of larger and smaller neurons [69], and somatotopic and/or topographic arrangement of cell bodies [34]–[36], [71], [72]. However, reported DRG parameters can have large variations. For example, the cell body volume ranges from 1 to over 150 cubic micrometers, greater than a 100 fold variation [70]. Cell count studies which only choose to include cells portraying the nucleolus have increased bias as well [15]. To decrease bias, a smaller counting unit must be used, such as smaller comparison regions.

The relative location of neuronal cell bodies within the DRG has not been quantified. There are anecdotal references to superficial cell bodies [32], [73] and occasional figures showing cross-sectional areas [32], [74], [75] from various sources. Of note, several studies have examined cross-sectional areas of cell bodies but have not related them to DRG cell distribution. Instead, these studies focus on the relationship between cell size and conduction velocity [65], central and peripheral branch differences [66], and myelin sheath thickness [74]. Studies have not been completed which incorporate cross-sectional areas of neuronal cell bodies and neuronal cell body location to provide specific insight into DRG cell body distribution.

A limitation to DRG morphology and cytology studies is the few models developed to guide DRG research. McLain developed a qualitative model to provide a comparison to injured ganglia, however a quantitative model of the DRG has not been developed [76]. There is a need for a greater understanding of DRG cellular morphology and cytology, increased quantitative measurements for DRG cell body counts and volume, and a model that provides a better understanding of cell body distribution. In this work we establish methods for determining and modeling the distribution of neuronal cell bodies within DRG, using mid-DRG cross-section images from feline lumbosacral levels. This two-dimensional analysis provides key insights and demonstration of the approach and can be expanded into three-dimensional analyses if desired.

Methods

We present three methods for assessing neural structure randomization and distribution, applied to DRG neuronal cell bodies in this study: an assessment of spatial

randomization, a Cartesian grid model of neuronal cell body distribution without tissue, and a polar transformation model of neuronal cell body distribution. Statistical tests within each section are used to determine the significance of the respective distributions. All MATLAB scripts are available in the Open Science Framework repository (DOI: 10.17605/OSF.IO/Q9UJ7, https://osf.io/q9uj7) [77].

After experimental use for other objectives, fifteen male adult felines (average weight of 4.9 ± 0.6 kg, average age: 1.0 ± 0.2 years) were euthanized via an intravenous 85-100 mg/kg overdose of sodium pentobarbital. Two animals were perfused transcardially with one liter of phosphate buffered saline followed by one liter of 4% paraformaldehyde (PFA) prior to tissue removal. In the remaining animals, tissue was removed promptly after euthanasia. During prior surgical procedures, a lumbosacral laminectomy to expose spinal roots was performed, thus post-mortem access was prompt. Care was taken to ensure the dorsal root ganglion were not harmed due to surgical intervention through standard surgical techniques. Only vertebrae were removed during the laminectomy procedure, with no surgical tools inserted into or damaging DRG. One or more lumbosacral DRG (seventh lumbar – L7; first, second, or third sacral – S1, S2, S3) from one or both sides were isolated and removed from the animal by transections at the junction with the spinal cord and distally on the whole spinal root. During tissue explant, care

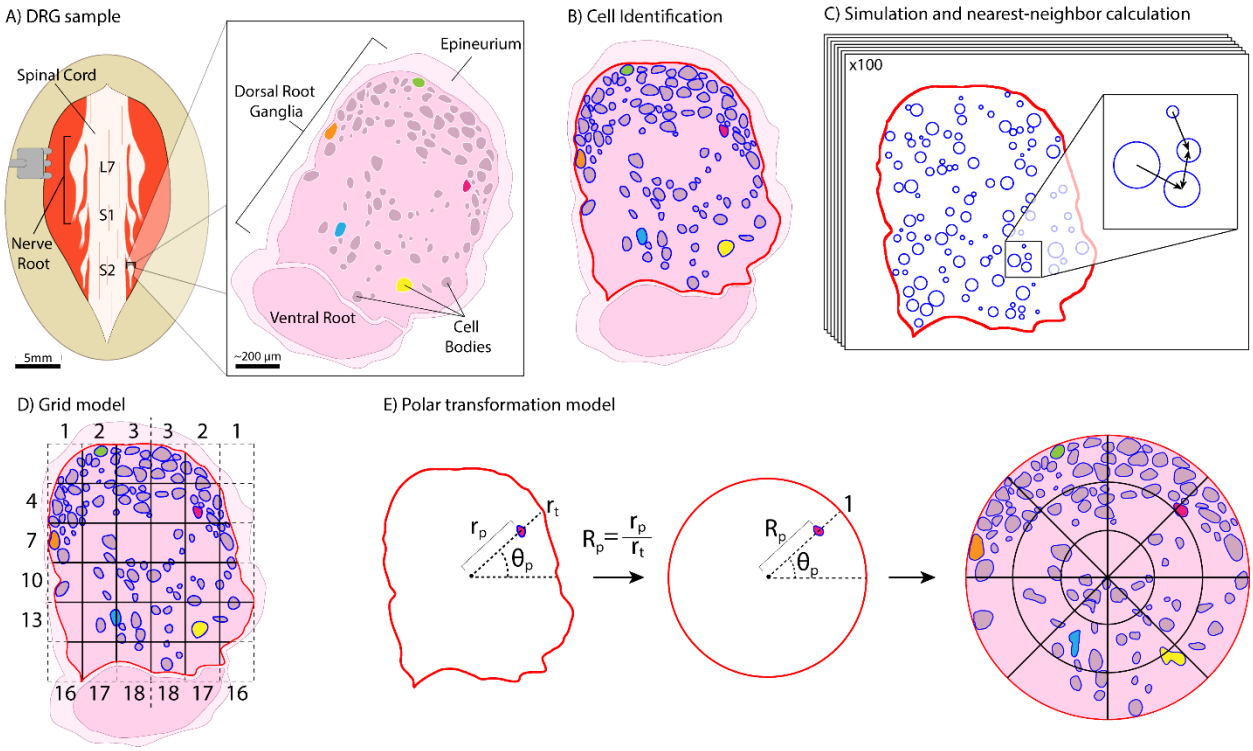

FIGURE 2 : Representation of tissue collection and analysis methods. (A) Medial tissue slice taken from feline DRG at spinal levels L7-S3. Tissue stained with hematoxylin and eosin, allowing cell bodies to be distinguished from the background. Cell-body containing region is DRG. Several cell bodies highlighted in non-histological colors for clarity through processing steps. (B) Tissue slice oriented with the DRG on top and ventral root underneath. Cell and DRG borders demarcated in blue and red, respectively. (C) MATLAB algorithm used neuronal cell size data and DRG border location to generate 100 random simulations of non-overlapping cell arrangements for comparison to actual arrangement. [inset] Demonstration of nearest-neighbor distance calculation, with arrows pointing toward nearest neighbor of each cell. (D) Division of demarcated DRG into 6x6 grid for calculation of neuronal cell density in each grid square. DRG border takes priority over grid for determining square boundaries. Squares numbered from left to right then top to bottom, with numbers reflected across the vertical axis. (E) For transforming each pixel: angle θ_p from centroid-horizontal; distance r_p from centroid to pixel; distance r_t from centroid to DRG border along θ_p. Transformed polar coordinate is (R_p, θ_p). [right] Transformed DRG, with a 3x8 radial grid (24 annular sectors) overlaid here for ease of visualization, though a 44x44 radial grid (1,936 annular sectors) was used. Neuronal cell density is calculated in each annular sector, as previously in grid squares.

was taken to not apply any pressure on DRG and to limit handling to proximal and distal nerve roots. Each sample was fixed in PFA at room temperature for at least one week. Not all DRG were removed or used in this analysis from each animal due to surgical limitations or other experimental needs. The University of Michigan Institutional Animal Care and Use Committee

approved all animal work, which was carried out in accordance with the National Institute of Health Guide for the Care and Use of Laboratory Animals.

After fixation, roots were cut orthogonally to the mid-axis plane at the largest width (FIGURE 2(A)), and embedded in paraffin with the cross-section plane facing up. A microtome (Finesse ME+, ThermoScientific, Waltham, Massachusetts, United States) was used to create a four micrometer thick tissue slice from each sample, which was fixed on a slide and stained with hematoxylin and eosin using standard techniques (FIGURE 2 (A)).

The DRG slides were imaged with an inverted microscope (IX83, Olympus, Shinjuku, Tokyo City, Tokyo, Japan), with the brightfield setting at 10 times magnification and Nikon (Minato, Tokyo City, Tokyo, Japan) Element BR 3.2 Software. Any dorsal root ganglion which appeared damaged were not included in samples for analysis. The image was uploaded to the ImageJ (https://imagej.nih.gov/ij/, RRID: SCR_003070) plug-in for ObjectJ (https://sils.fnwi.uva.nl/bcb/objectj/index.html, Vischer, N. & Nastase, S. University of Amsterdam), on a desktop PC.

The image was rotated such that the dorsal root was at the top of the image and the ventral root was at the bottom of the image, ensuring the DRG was oriented in a dorsal-upright position for all analysis (FIGURE 2 (B)). Pixel dimensions were kept constant to ensure accurate scaling. For clarity, the 2D images will be referred to simply as DRG, though the goal of this work was to represent only mid-root cellular distributions with no implied stereotaxic claims.

DRG stained with hematoxylin and eosin have neuronal cell bodies which are visually distinct from the background, but the contrast is too poor to rely on automatic image segmentation. Automated cell identification with other staining methods could be used with

our methods. Therefore, image processing began in ObjectJ with manual demarcation of the borders of each neuronal cell body (in blue) and the DRG itself (in red). Neuronal cell bodies were identified due to morphological size differences as neuronal cell bodies are larger than other cells within the DRG [27]. Within ObjectJ, two objects were created: Cell Trace and Edge ROI (region of interest). The Cell Trace object was defined as an area tool to trace the borders of each neuronal cell body in blue and calculate area. The Edge ROI tool was defined as an area tool to trace the border of the DRG in red. The DRG border was taken to be within the epineurium (FIGURE 2 (B)).

Assessing Spatial Randomness

Our first step in analyzing spatial distribution was to determine whether the DRG sections contained a statistically non-random distribution of neuronal cell bodies. The presence of non-randomness is considered prerequisite to making claims about any specific distribution. To quantify randomness, we utilized a nearest-neighbor distance method. For each DRG, the distance from each neuronal cell body centroid to its nearest neighbor was calculated with a script in MATLAB (Mathworks, Nantick, Massachusetts, United States, RRID: SCR_001622). The mean of these values ($\bar{d}_A$) contains information about the randomness of the section, because a random 2D point process will differ from a biased process in characteristics of its distribution, including inter-point distances [28]. However, the DRG must be compared to representative random cell arrangements to have significance.

To produce random distributions for comparison, in MATLAB we simulated 100 random arrangements of neuronal cell bodies for each DRG. These simulations placed circular “neuronal cell bodies” inside the DRG border, equivalent to the number of neuronal cell bodies found in

the original sample. The area of each simulated neuronal cell body was pulled randomly from the areas of neuronal cell bodies in the original sample. Simulated neuronal cell bodies were placed at random locations but, importantly, not allowed to overlap with one another. Mean nearest-neighbor distance was calculated for each simulated arrangement ($\bar{d}_E$) for comparison to the real sample (FIGURE 2 (C)). The ratio $D=\bar{d}_A/\bar{d}_E$ has a value of 1 in the case of total randomness. If D<1, the sample is non-random towards aggregation, that is, neuronal cells are clustered in particular areas. If D>1, the sample is non-random towards equidistant patterning. D has a theoretical range of 0 to ~2.15 [28]. We calculated D for 100 simulations of each DRG to obtain distributions for statistical comparison with a two-tailed Student's t-test. DRG with mean D significantly different from 1 (α = 0.01) were considered to have non-random neuronal cell body distributions.

Grid Model

Following the test for randomness, we proceeded to a search for trends in neuronal cell body distribution. In ObjectJ, a Grid Line object was defined as a line tool to create an overlay grid on each DRG slice. A range of grid sizes were considered from 3x3 to 7x7, but a 6x6 grid was chosen as having a balance between resolution and having cell bodies in most grid squares. Smaller or larger grids may be appropriate for neural structures that vary from the typical sizes of feline DRG (1-2 mm cross-section). Data from ObjectJ was output to spreadsheets (Excel, Microsoft, Redmond, Washington, United States) to determine the number and average area of neuronal cell bodies in each of the 36 grid squares. For squares along the perimeter, the DRG tissue area in each was determined for normalization purposes (FIGURE 2 (D)). From these values we calculated for each grid square a normalized neuronal cell area density (percentage

of the grid square occupied by neuronal cell bodies). Because each DRG was divided into the same number of grid squares, the neuronal cell densities allowed direct comparison across samples. The values were visualized and analyzed statistically using platforms in the statistical software program JMP (SAS Institute Inc., Cary, North Carolina, United States, RRID: SCR_014242). A contour map was produced to visualize trends. Regional divisions, such as ventral/dorsal or outer/middle/inner layer, were used for initial categorization of the grid squares, with cell densities compared using either a Student's t-test or ANOVA with Tukey Honestly Standard Difference (Tukey HSD) test for multiple comparisons ($\alpha = 0.01$).

Polar Transformation Model

While the grid square analysis is useful for determining general trends (see Results), we sought a more detailed and objective analysis, by transforming distributions into a polar model (see Discussion for advantages and limitations of each approach). The demarcated images were loaded into MATLAB for analysis with the Image Processing Toolbox. The images were split into red, blue, and green color channels. Thresholding on the red and blue channels produced binary images highlighting the locations of border pixels. A MATLAB function for detecting connected components in binary images was used to detect and analyze each object, determining the location of the object centroid and all associated pixels. A diagnostic image showing identified regions allowed for necessary corrections to be made to the manual demarcation as necessary to ensure accuracy in image segmentation. The result of this processing is that each histological image could be considered as a large bordered region (the DRG) containing regions of interest (cell bodies) with known properties for analysis.

To prepare for cross-sample comparison, we first mapped the neuronal cell bodies from each DRG to a normalized polar map using a custom MATLAB script with the following steps. The centroid of the overall DRG region was determined to establish an origin. Then, a polar angle θ_p from 0°-360° was calculated relative to the positive horizontal axis for each pixel in the region, identified as either a "neuronal cell body" or a "non- neuronal cell body" pixel. The distance from the origin to each pixel (r_p) was found along this angle, as well as the distance from the origin to the DRG border (r_t). The normalized ratio $R_p=r_p/r_t$, which varies from 0-1, was taken as the polar radius for the pixel. At this point, each pixel could be identified with a polar coordinate of (R_p, θ_p), and lay within a unit circle. The perimeter of the circle represents the DRG border (FIGURE 2 (E)). This normalized mapping step allowed direct comparison across irregularly shaped samples.

To screen for trends in neuronal cell density, we divided each normalized DRG into 1,936 annular sectors, that is, each DRG was divided into 44 regular wedge-shaped sectors which were further divided into 44 regular nested rings. In each annular sector, we calculated neuronal cell area density as the number of neuronal cell body pixels divided by total pixels (neuronal cell body + non-neuronal cell body pixels). The 44x44 division was chosen as the smallest number of divisions which yielded at least one annular sector with 100% neuronal cell density in each DRG, that is, which produced sectors approximately on the scale of the largest neuronal cell bodies. Other divisions may be appropriate for analyzing different neural structures. This process yielded a table of data containing information about the original DRG tissue sample (feline source, spinal level) as well as the polar location and density of each annular sector. We again produced a contour map for visualization of trends across all DRG

samples. Because our particular histological samples do not preserve sagittal (left-right) orientation, we folded the contour map onto itself along the vertical midline to avoid bias in the analysis presented here. Applications maintaining orientation would not need to do this. Averaged annular sectors in this half-circle were assigned a vertical angle θ_v, defined as the angle from the positive vertical axis of the DRG with a range of 0°-180°.

To improve objectivity about the division of the DRG into regions of differential density, we utilized the JMP Partition platform for recursive partition modelling. This classification tool splits a distribution of dependent variable values into sub-populations based on several independent variables. This model produces a "decision tree" which, at each node, selects a split value of one independent variable to maximally separate the population by dependent variable. In our data set, the dependent variable was neuronal cell density and the independent variable was annular sector coordinate (R_p, θ_v). Given the possible inputs, the program first produces a variety of possible models with minimized sum of squared errors. Then it chooses from among the generated models by maximizing the LogWorth statistic, defined as $-\log_{10}$(p value).

To avoid overfitting, 10-fold cross-validation was used in generation of the partition model. This involved randomly splitting the data set into 10 segments, then iteratively training the model with 90% of the data while testing the fit on the remaining 10%. This cross-validation step not only ensured appropriate partitioning but also provided a stop condition for further splits. We continued splitting the decision tree recursively until the next ten best splits did not improve the mean R2 value of the validation data set. Importantly, however, the resulting model does not necessarily imply statistical significance. To test this, we recategorized the

annular sectors into regions following the split values suggested by the partition model. Overall neuronal cell densities in the resulting regions were compared with Tukey HSD tests, allowing us to determine whether the trends suggested by the partition model were statistically significant ($\alpha = 0.01$).

Results

Raw DRG slice images, demarcated DRG slice images, summary spreadsheets, and MATLAB analysis scripts are available in the Open Science Framework repository (DOI: 10.17605/OSF.IO/Q9UJ7, https://osf.io/q9uj7) [26].

DRG Samples

For our evaluation of these methods, twenty-six DRG were analyzed from fifteen adult male cats, with multiple DRG sampled from seven cats. Six DRG were from the L7 level, nine from S1, ten from S2, and one from S3. DRG level was determined by anatomical position. Eight DRG came from the left side of the animal, eighteen from the right side. This imbalance resulted from the accompanying experimental procedures, predominantly on the left side, that sometimes left the DRG unusable for histology. None of the DRG analyzed were directly involved in tests performed on the cat before tissue resection. FIGURE 3 shows an example of a labeled medial DRG section.

Assessing Spatial Randomness

In the assessment of randomness for our samples, we tested the distribution of D for each DRG with a two-tailed Student's t-test, based on the null hypothesis of equality with 1 (representing a totally random neuronal cell body arrangement) and a threshold p-value of

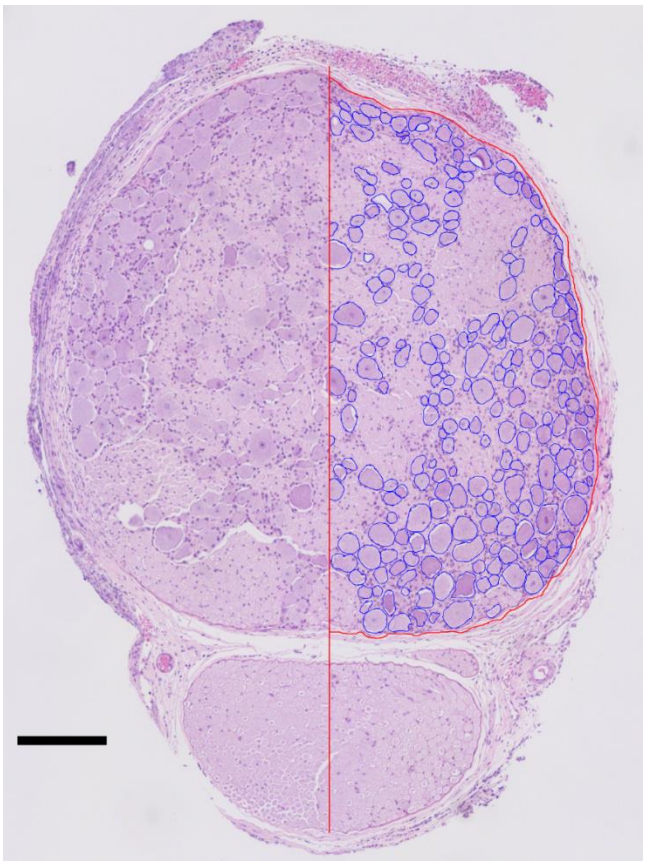

FIGURE 3: Sample hematoxylin and eosin stained medial DRG section used for analysis (Experiment 10, right S1). Left half: raw image. Right half: neuronal cell bodies demarcated in blue, DRG border demarcated in red. Scale bar is 200 μm.

0.01. We found that 24 of 26 DRG had a mean D significantly less than 1, indicating that most of the DRG have a non-random arrangement of neuronal cell bodies (see FIGURE 4 (A) for an example DRG). FIGURE 4 (B) shows a histogram of D across all sampled DRG. Of the remaining DRG, one had a mean D not significantly different than 1, and the other was significantly greater than 1. The Shapiro-Wilk test for normality showed that the distribution was significantly different than normal ($p<0.0001$). The best fit was instead a mixture of 3 normal distributions, which had an estimated-actual quantile fit with $R^2=0.99$ (FIGURE 4 (B, C)). The mean D for the distribution subgroups were 0.58, 0.80, and 0.93. These values were less than one, and a Wilcoxan rank test for non-normal distributions showed that the population mean

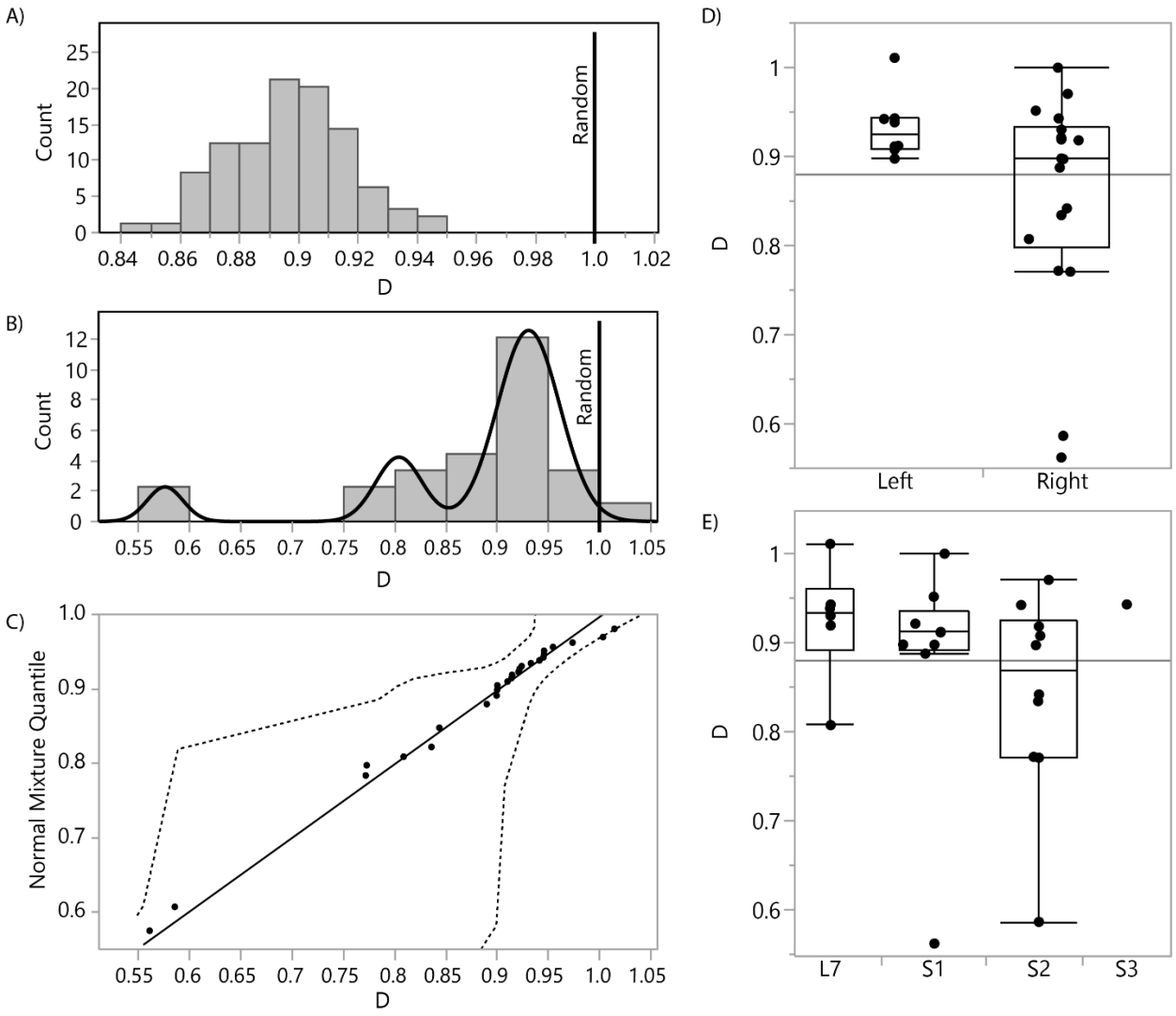

FIGURE 4: Analysis of spatial randomness in DRG (A) Histogram of 100 simulated D values for one DRG, with vertical line at D=1.0 (random). Distribution mean (0.90; standard deviation 0.02) is significantly different than 1. D is the ratio of the actual mean nearest neighbor distance to the simulated nearest neighbor distance. (B) Histogram of mean D values for each DRG, with fitted mixture of 3 normal distributions (means at 0.58, 0.80, and 0.93). (C) Diagnostic plot showing predicted versus actual quantile for each of the D values in (B), based on the normal 3 mixture shown in (B). Dashed lines show 95% confidence interval. (D) Box plots comparing mean D values for each DRG by left or right source, showing no significant difference between groups. Horizontal line represents overall mean (0.88). (E) Box plots comparing mean D values for each DRG by spinal level source, showing no significant difference between groups.

was significantly less than 1 ($p<0.0001$). This indicated that not only are the neuronal cell body arrangements random in our sample set, but they are aggregated. That is, neuronal cell bodies in the DRG are found clustered together in a group or groups in a fashion which is statistically

unlikely to occur in a case of pure randomness. There was not a significantly different degree of randomness across left/right division (FIGURE 4 (D)) or spinal level ($p>0.01$ for each) (Figure 3(E)). Therefore, our next goal was to determine if there was a trend in where neuronal cell bodies tend to aggregate.

Grid Model

We began by analyzing spatial trends in neuronal cell density gleaned from the 6x6 grid model. To visualize this, we used JMP to produce a contour map of mean neuronal cell density relative to grid position (FIGURE 5 (A)). The contour map suggested a primarily radial gradient of density, with lower density in the innermost DRG region and higher density in the outer coronal region. There also appeared to be a slight trend toward higher density in the dorsal

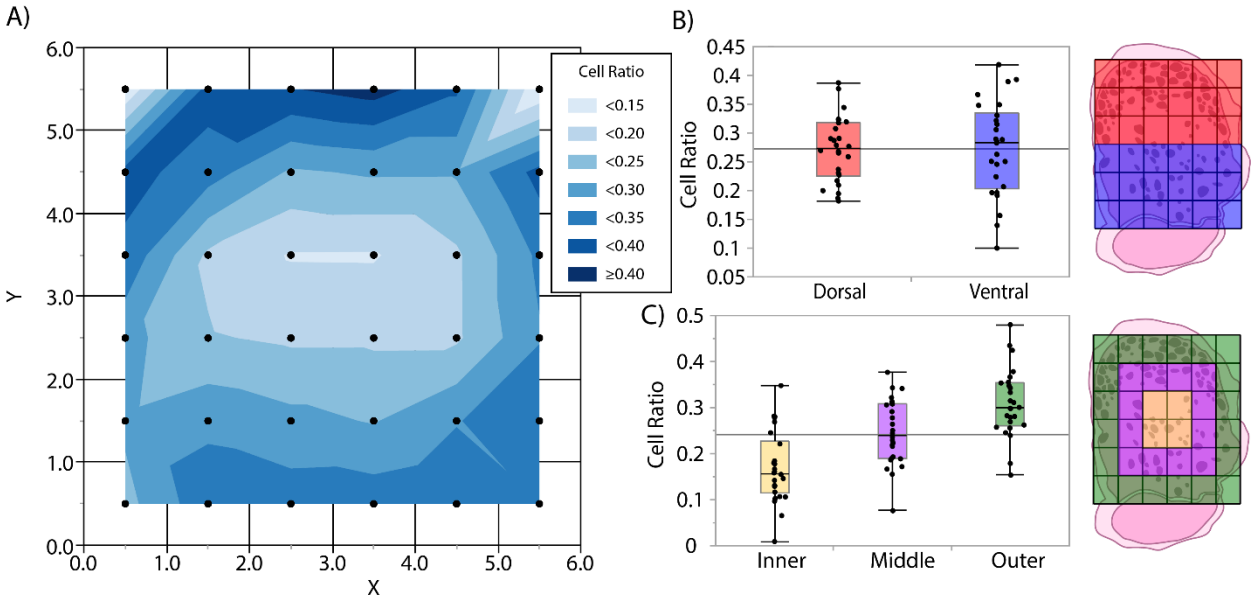

FIGURE 5: Grid model of cell density in DRG (A) Contour map of mean neuronal cell density based on 6x6 grid model. Data represented at center of grid square. (B) Box plots comparing mean neuronal cell density in dorsal and ventral sector for each DRG. No significant difference found between groups. Plot key at right. (C) Box plots comparing mean neuronal cell density in inner, middle, and outer rings for each DRG. All groups significantly different from one another ($p < 0.01$ for each group comparison). Plot key at right.

(top) regions than the ventral (bottom), however no significant difference was observed between dorsal and ventral regions (FIGURE 5 (B)).

We tested the radial gradient hypothesis by dividing the grid into 3 “rings,” an outer, middle, and inner (FIGURE 5 (C)). For each DRG, we calculated mean neuronal cell density in

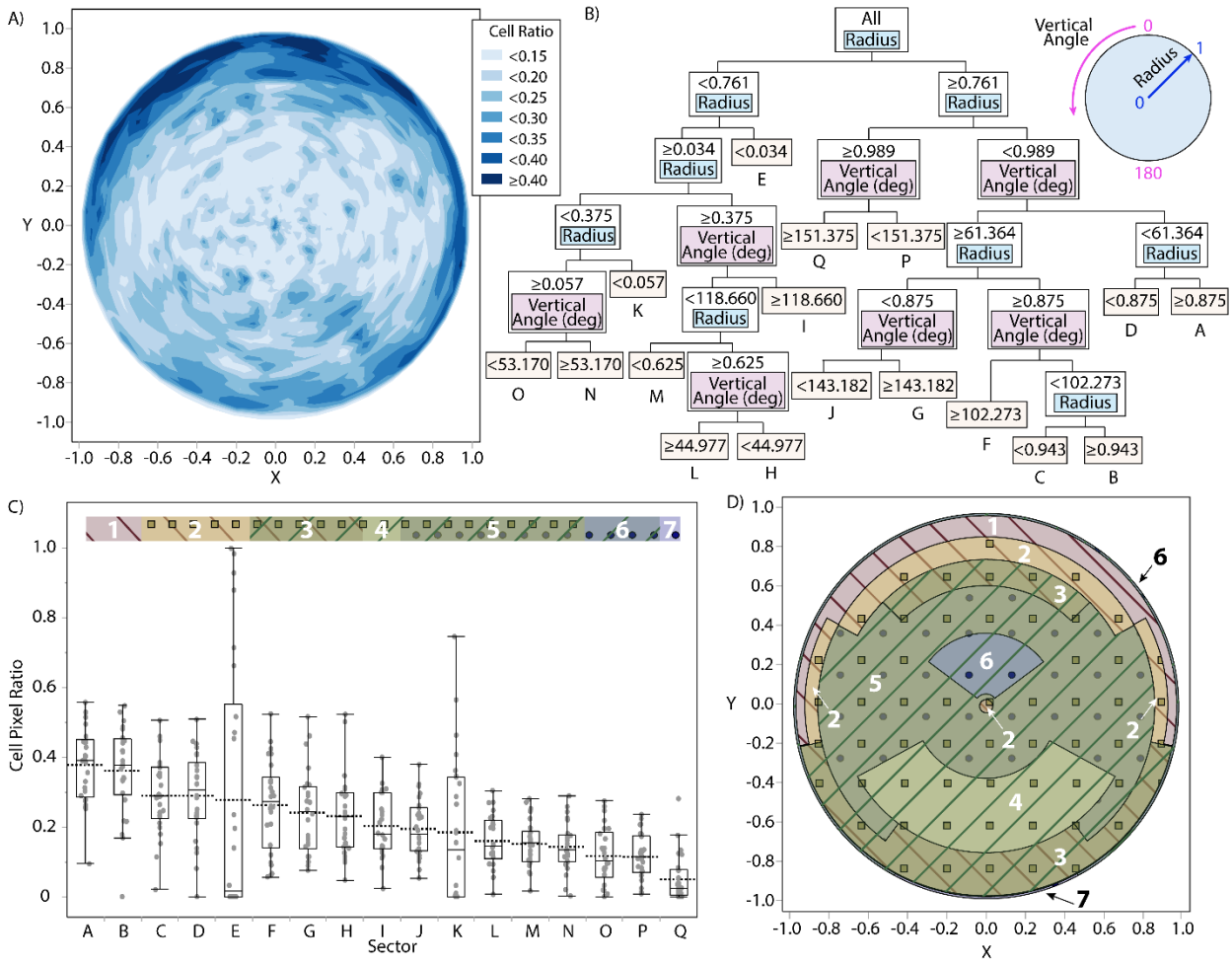

FIGURE 6: Polar model of cell density in DRG (A) Contour map of mean neuronal cell density based on polar transformation model with 44 divisions radially and angularly for full 360° annular sector set. (B) Branching tree diagram representing a partition model of neuronal cell density into annular sectors based on vertical angle and radius, after folding over the 360° data set onto the 0-180° midline to minimize lateral bias. Nine divisions were based on radius, seven on vertical angle. Sectors are labeled from A to Q in order of descending mean (C) Box plot comparing cell density in each sector A to Q per partitions in (B). Comparison bar along top indicates statistical significance between groups: groups not connected by the same pattern (diagonal stripes in one of two directions, squares, or circles) are significantly different from one another. Distinct overlapping regions numbered from 1 to 7 (D) Spatial representation of (B) and (C) with the dataset mirrored across midline to provide circular visualization. Note that outer regions 6 and 7 are very thin outer borders which are difficult to visualize.

each ring, then compared the rings with a Tukey HSD test for multiple comparisons preceded by an ANOVA test for significance. The tests indicated that there was a significant difference ($p < 0.001$) between neuronal cell density in each ring, with density rising with increasing radial distance from the center. The outer ring contained a mean neuronal cell density of 0.30, nearly twice the density of the inner ring (0.17).

Polar Transformation Model

To explore the radial density gradient in depth, we analyzed the polar transformation model. FIGURE 6 (A) shows a contour map of the mean neuronal cellular density for the full 360° annular sector set, as determined by the polar transformation and division into 1,936 (44x44) annular sectors. The partition model of neuronal cellular density by radial and angular location, after folding over the full 360° annular sector set along the vertical midline to a 180° combined set, contained 16 splits (FIGURE 6 (B)), with a testing data set R^2 of 0.0583 and a validation data set R^2 of 0.0577. This shows that, while the model only explains about 6% of the variation in cellular density for our DRG samples, it is consistently predictive. A comparison of the regions produced with ANOVA and Tukey HSD showed significant differences within the set ($p < 0.0001$) which are best described by the box plots of FIGURE 6 (C). FIGURE 6 (D) shows a spatial map representing the differential neuronal cellular densities in the regions determined by the partition model and the Tukey test, mirroring the 180° folded data set to create a full circular visualization. The model suggested that the variable of primary importance is radial distance from the center (82% of model variation explained), and that the primary appropriate division is between the inner low-density 76.1% and outer high-density 23.9%, though the outermost 1.1% is a lower density region. The secondary division is likely due to packing of the

neuronal cells, which naturally leads to low density at the extreme edges. The highest density area within the larger outer ring is above the vertical angle of 61.4°, or alternately the upper 122.8° of the DRG.

To give a sense of predictive value of this model, 13/26 of the DRG had the highest cell density in one of the two highest predicted regions (referred to as A or B, respectively, in FIGURE 6 (C, D)). The only major deviation from this trend was in DRG with the highest density predicted in region E, the very center of the DRG. This region had the highest observed density in 7/26 of the DRG. This region exhibited high variability in neuronal cell density, as it was in the bottom two regions for density in 13/26 DRG. This variability is likely explained by the fact that sectors in this area are relatively small and the presence or absence of a single neuronal cell body in this region could be enough to drastically change the observed neuronal cell density.

Discussion

In this study we established methods for assessing and modeling the distribution of neuronal cell bodies in dorsal root ganglia sections. As such, this is the first study to quantitatively assess DRG neuronal cell body distribution. Using our methods, we established quantitatively that arrangements of neuronal cell bodies in our DRG samples are non-random, and that these arrangements tend toward having clusters of neuronal cell bodies in certain regions. This claim is based on analysis of nearest-neighbor distances in histology compared to reasonable simulations of random neuronal cell body arrangements (FIGURE 4). The results suggest several levels of randomness, reflecting the heterogeneity of the neuronal cell body arrangements analyzed. However, the source of our DRG samples (left/right or spinal level) did not significantly affect the level of randomness.

Having established non-randomness, we developed two methods for modeling DRG neuronal cell density, first a grid model then followed by a polar transformation model. The grid model displays neuronal cell density concentrations of neuronal cell bodies in the outer regions with a higher concentration on the perimeter of DRG then in the central ROIs (FIGURE 5). Outer regions of the DRG for dorsal and ventral regions exhibited higher neuronal cell densities then inner or middle regions. A contour plot analysis exhibited circular ring pattern for neuronal cell density, with an absence of corners. The grid model was relatively straight-forward to generate; however, the outer border does not accurately depict the curved perimeter of DRG and neuronal cell placement in a grid region when the average normalized neuronal cell area and the average normalized DRG area are close was difficult. These limitations and a contour analysis of neuronal cell density supported the creation of the polar transformation model.

The polar transformation model displays the proportion of each annular sector area occupied by neuronal cell bodies (FIGURE 6). There are higher densities on the perimeter, primarily on the dorsal side with lower densities in the central region. This model provides a more accurate representation of DRG, with the round contour and the intuitive application of applying regions in the shape of circular rings, which were supported through statistical analysis of the grid model. However, the polar transformation model includes some distortion due to the circular transformation and irregularly sized sectors. Both computer models demonstrate a characteristic neuronal cell body distribution around the perimeter of the DRG. As a secondary classification, the outer dorsal region exhibited the highest neuronal cell densities for both models.

The results of this study support prior qualitative statements about dorsal, superficial clustering of neuronal cell bodies in DRG [32], [73]. Our mid-section DRG slices also compare favorably to prior examples of cross-sections in the literature, such as in cats [32], [74] and rats [75], which show characteristic neuronal cell body clustering around the periphery. In this study we did not seek to quantify the distribution of neuronal cell body sizes, as our cross-section tissue slices only sample a portion of each neuronal cell body [70]. Although we only focused on feline lumbosacral DRG, we expect our methods will yield similar observations at other spinal levels and in other species [74].

In addition to broadening our understanding of DRG anatomy, the results obtained from our methods provide quantitative information to aid in the design of electrodes for interfacing with DRG for recording or stimulation applications. There are no electrodes specifically designed to accommodate the unique geometry and neuronal cell-body distribution of DRG. Some DRG interfacing applications require cell-selective capabilities and desire the ability to record large signals from cell bodies rather than smaller potentials at axon nodes [13], [15], [19], [44]. These applications may seek to develop microelectrodes that are very superficial in their access to DRG. A recent study with non-penetrating microelectrodes showed promise for recording DRG cellular potentials [41], and we are continuing this work with the development of thin-film arrays that conform to the DRG surface [78]. Alternatively, DRG interfaces primarily for stimulation [8], [10], [12] may target axons. These approaches may seek to develop custom microelectrodes that target central regions of DRG, based on our model. Additionally, this work will also be useful in informing the nascent field of DRG stimulation as a clinical pain therapy [79], [80].

Several aspects of our study design may have impacted our observations. During tissue removal and histological processing, compression of the roots could have occurred. Visual comparison of perfused and non-perfused samples suggests no difference in overall morphology and no obvious tissue shrinkage. If tissue shrinkage occurred during processing, our normalization approaches provide mitigation against broad effects. In some cases, multiple samples were collected from individual animals at different spinal levels. This unbalanced sampling may skew data analysis, though no evidence of this was found. User error may have occurred during manual tracing of neuronal cells and roots. Only medial slices were included in this analysis, which does not account for axial cell density variation across DRG. This is a future area for analysis.

We anticipate several approaches for extending the methods used here. The analysis here focused only on DRG slices sampled at the widest point. A full-DRG model that incorporates slices from the spinal cord to the spinal root will provide a three-dimensional neuronal cell-body distribution. We also plan to identify medial and lateral aspects of roots. Analyses of spinal roots at other levels (cervical, thoracic, lumbar) and in other species, including humans, will elucidate the consistency of cellular distribution across these other sources. The incorporation of cell tracing technology [72] would give an ultimate quantification of cellular sources and distribution.

Conclusion

In this study, we developed methodology to assess several properties of spatial organization in DRG and demonstrated its use in medial cross-sections of feline lumbosacral samples. We showed that the arrangement of cell bodies in DRG is statistically non-random,

tending toward clustering of cell bodies. We also use two methods to quantify for the first time the cellular density in DRG. Using both methods, we showed that the outer edge of the DRG has a higher density than the interior. Using the polar transform normalization, we showed that there was a higher density on the dorsal aspect of DRG. As new investigative and clinical technologies are developed to interface with DRG, this anatomical mapping and future uses of the described methodology will provide invaluable information for targeted design.

Chapter 3

Spatial Models of Cell Distribution in Human Lumbar Dorsal Root Ganglia

Abstract

Dorsal root ganglia (DRG), which contain the somata of primary sensory neurons, have increasingly been considered as novel targets for clinical neural interfaces, both for neuroprosthetic and pain applications. Effective use of either neural recording or stimulation technologies requires appropriate spatial position relative to the target neural element, whether axon or cell body. However, the internal three-dimensional spatial organization of human DRG neural fibers and somata has not been quantitatively described. In this study, we analyzed 202 cross-sectional images across the length of 31 human L4 and L5 DRG from 10 donors. We used a custom semi-automated graphical user interface to identify the locations of neural elements in the images and normalize the output to a consistent spatial reference for direct comparison by spinal level. By applying a recursive partitioning algorithm, we found that the highest density of cell bodies at both spinal levels could be found in the inner 85% of DRG length, the outer-most 25-30% radially, and the dorsal-most 69-76%. While axonal density was mostly homogeneous across the DRG length, there was a distinct ow density region in the outer 7-1% radially. These findings are consistent with previous qualitative reports of neural

distribution in DRG. The quantitative measurements we provide will enable improved targeting of future neural interface technologies and DRG-focused pharmaceutical therapies and provide a rigorous anatomical description of the bridge between the central and peripheral nervous system.

Introduction

Dorsal root ganglia (DRG) are regions of the posterior spinal roots which contain the cell bodies of all primary sensory neurons innervating a specific dermatome of the body or end organ [64]. Recently, DRG have been increasingly investigated as sources from which to record control signals for neuroprosthetic devices, for applications ranging from treating bladder dysfunction to providing limb prosthetic control and sensory feedback [18], [19], [81]. Additionally, dorsal root ganglion stimulation (DRGS) is an emerging therapy for chronic neuropathic pain [4], providing a non-addictive alternative to opioids for pain management.

Although these technologies have the potential to provide dramatic improvements in quality of life for a diverse range of patients, preliminary clinical studies have demonstrated limited success thus far. Commonly reported issues include inconsistencies in the quality of elicited sensations and variable amounts of pain relief across patients [82]. These technologies rely on either the accurate recording or delivery of electric currents to specific types of DRG neurons (e.g. recording from bladder afferents, stimulating sensory inputs to reflex circuits). However, we have a limited understanding of the three-dimensional (3D) spatial distribution of primary afferents throughout human DRG. Describing the 3D cellular anatomy of DRG could inform the clinical implementation of these technologies (e.g. DRGS electrode placement relative to the ganglion), which may lead to improved and more consistent clinical outcomes.

DRG contain both the cell bodies and portions of the axons of primary sensory afferents. Neural recording technologies detect neural activity through the voltages generated by the transmembrane currents generated by neural signal propagation [44]. The largest transmembrane currents, which would contribute to the bulk of the recorded signal, are thought to originate from the cell body and axon initial segment of recordable cells [83]. In contrast, extracellular stimulation technologies are thought to primarily induce neural activation in axons [84], with modeling studies suggesting that DRGS electrodes primarily activate the axons of large myelinated tactile afferents [42]. Although the specific roles of subgroups of primary afferents are complex, DRG cells can be roughly broken into functional groups based on cell body and axon size [67]. C-fibers are small unmyelinated cells that typically conduct thermal or noxious sensation [85], [86]. Myelinated A-fibers, which are typically mechanoreceptive or proprioceptive, are larger than C-fibers, typically have thinly- to thickly-myelinated axons. A-fibers can be further stratified into Aα-, Aβ-, and Aδ-fiber classes which are listed in order of descending conduction velocity and fiber size [87]. Although this classification scheme is commonly used throughout the literature, there is a dearth of studies examining the spatial distribution of these fibers throughout the DRG.

The effectiveness of both recording and stimulating neural interface technologies relies heavily on the spatial relationship between the interface electrode and particular neuron types of interest. However, few studies have examined the spatial organization of neurons in DRG, and to our knowledge, no studies exist in the human literature. Various studies have discussed a weak functional somatotopy for the DRG in animal studies based on nerve tracing, with rostral-caudal, medial-lateral, and ventral-dorsal divisions all present to a certain degree [34],

[35], [71], [88]–[91]. In terms of overall structural divisions, anecdotal references include images showing superficial cell bodies or a “central fiber stream” in the DRG [31], [32], [73], and a neural recording study in feline DRG reported the largest density of cell bodies at a depth between 0 and 100 µm [50]. There is a general consensus that most cell bodies are found around the circumferential edge of the ganglion. That idea was supported by our previous study, in which a quantitative analysis of feline lumbosacral DRG showed that the highest density of cell bodies in medial sections could be found in the outer 24% radially and on the dorsal-most side of the ganglion [49]. However, in this previous study, we only examined

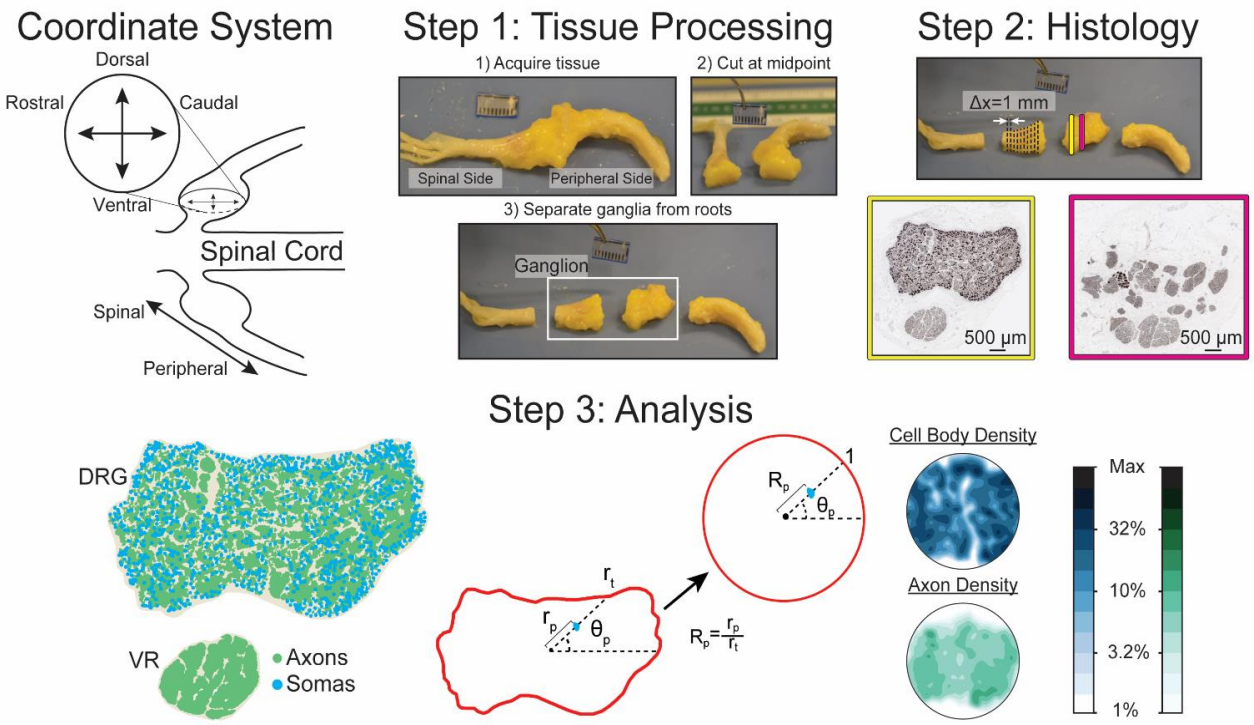

FIGURE 7: Histological processing and analysis of DRG (top left) Illustration of coordinate system for DRG cross-section images. (top center) Initial tissue processing. (top right) Representation of sample locations and NF200 stained samples. (bottom left) DRG cross-section after automated processing, with identified axon and soma locations highlighted. (bottom center) Diagram of polar normalization, demonstrating transformation from perimeter and internal features to unit circle. (bottom right) Contour plots generated from polar normalization of DRG at right, with logarithmic color scale at right.

neuronal distribution in medial sections of the DRG, while clinical neurotechnologies would likely act upon neurons distributed along the entire DRG.

In this work, we sectioned human lumbar DRG specimens at 1 mm increments along the nerve root axis. We stained these sections with neurofilament and imaged the sections for high-contrast identification of neural cell bodies and axons. We developed software to automatically segment and characterize the spatial location and size of neural elements. Finally, we used a recursive partitioning algorithm to model the 3D spatial densities of the neural elements. We also analyzed high-level donor demographic and anatomical trends in our data set. These analyses provide key insights for future neural interface technologies and therapies with human DRG.

Methods

Gross Tissue Processing

This study utilized human tissue donated by de-identified deceased individuals and was therefore determined to be "Not Regulated" by the University of Michigan Institutional Review Board [HUM00109152]. Bilateral human lumbar spinal roots from the L4 and/or L5 spinal levels were collected by the National Disease Research Interchange (NDRI, Philadelphia, PA) from deceased donors within 72 hours of aortic cross-clamp. Donors were excluded if they had a history of diabetes, cancer, herpes zoster, a peripheral nerve condition, spinal cord injury, previous spine surgery, or opiate abuse. The tissue was stored in 10% neutral-buffered formalin and shipped at ambient temperature. Upon receipt, we used calipers to measure the DRG portion of each root at 1 mm increments to determine the gross tissue dimensions. We then removed two 1 cm segments constituting the approximate proximal (i.e. nearest the spinal cord) and distal (i.e. nearest the peripheral nerve) half of the DRG and placed the segments in

histology cassettes (FIGURE 7, Step 1). We placed the cut side face-down in the cassette to preserve DRG orientation across slides. When necessary, we removed additional segments to obtain samples of the entire DRG region. We stored the cassettes in 70% ethanol to halt fixation, and shipped them an external histopathology lab (Histowiz Inc., Brooklyn, NY) for histological processing.

Histological Processing & Imaging

The histopathology lab embedded the tissue samples in paraffin (Leica EG 1150 H&C) and cut 4-5 μm thick sections at 1mm steps (~20 sections per DRG) (Leica RM2235 microtome). They then mounted the sections on slides and stained with a 1:3000 dilution of rabbit monoclonal antibody for neurofilament heavy polypeptide (NF200, ab40796, Abcam, Cambridge, UK) and counterstained for hematoxylin which stains nuclei in both A- and C-type fibers in humans [92], [93]. They imaged the slides at 40x with a brightfield slide scanner, with a resolution of 4 pixels per micron (Leica Aperio AT2). The resulting images had neural cell bodies and axons visible in dark brown and cell nuclei visible in blue (FIGURE 7, Step 2). Other DRG cellular types were also visible, including satellite cells and some endothelial vascular cells. The neural cellular elements were typically arranged into at least 2 fascicular regions. We considered the regions containing cell bodies (or continuous with cell-body containing regions across images) as DRG. We considered all other regions as ventral root (VR). To the extent analyzed, the VR was considered separately from the DRG. We screened images for quality issues, including excessive tearing or folding, and poor-quality regions were excluded from analysis.

Image Processing Software and Validation

Lumbar DRG contain on the order of 35,000 neurons [28], so to identify each neural element we developed a custom semi-automated graphical user interface (GUI) using MATLAB and its Image Processing Toolbox (MathWorks Inc., Natick, MA). After image load, the GUI allows the user to identify the DRG, VR, and non-neural outer tissue, then calculates an optimal rotation to align the DRG above the ventral root in the upper half of the image. In order to validate the GUI results, four validation images were selected pseudo-randomly from the final image set, to balance for inclusion from different donors, spinal levels, and sidedness (right v. left). A 1 mm square region containing both axons and cell bodies was randomly selected from each validation image. Following consultation from a neuropathologist, the first three authors each traced the neural cell elements in the validation sub-images using the ImageJ (https://imagej.nih.gov/ij/) plug-in ObjectJ (https://sils.fnwi.uva.nl/bcb/objectj/index.html, Vischer, N. & Nastase, S. University of Amsterdam).

For automated processing, all validation images were first converted to grayscale and white balanced against background luminescence for each color channel (red=R, green=G, and blue=B). These grayscale images were converted to binary (black and white) using a threshold determined to minimize the difference between the initially detected object number and the number of objects determined by each human validator. The best threshold across all images was 0.78, so this was used going forward. We discovered that a simple threshold tended to split large lightly stained cell bodies into many smaller objects, but that intact cell bodies could be recovered by utilizing the ratio between R and B channels. Specifically, R/B-B/R threshold of 0.5 consistently returned an image with intact cell bodies. This step was effective because the

neurofilament stain tended to have a high R and a low B, while hematoxylin had a strong B and weak R. This RB ratio transformation was noisy outside of the cell bodies, so only objects with area greater than 600 μm^2 were retained (roughly corresponds to circular objects with diameter 14 μm). The logical disjunction of the RB ratio image and the original binary image (RB Ratio OR Binary), denoised with a morphological "open" and with holes filled, served as the final image for automated neural element identification with MATLAB's Image Processing (MathWorks, Natick, MA, United States) toolbox.

To compare the automated system and human performance, we found the pixel overlap between the output images and calculated the precision and recall of the automated system, using the human segmented images as ground truth. Precision is the ratio between true positives and total positives (true positives + false positives) and is a measure of how often the program incorrectly labeled a pixel as belonging to a neuron. Recall is the ratio between true positives and ground truth positives (true positives + false negatives) and is a measure of how often the program missed a neuron pixel it should have labeled. Both ratios range from 0 to 1, with a higher value being a better score [94], [95].We extracted the shapes and locations of all neural elements in the original image from the resulting binary image for analysis.

Image Analysis

Following parameter optimization and comparison of GUI results to human performance, we analyzed each image containing at least 10 visible soma [96] in the GUI to determine neural element size, shape, and location. In-plane axons were identified as elements exceeding an eccentricity of 0.9 (i.e. axons that were predominantly elliptical rather than circular) and excluded from population size analysis. We defined mean diameter as the average

of the major and minor axis. Based on values previously reported [87], we used a mean diameter cutoff of 20 µm to distinguish larger axons from smaller cell bodies. We found that objects larger than 110 µm in diameter were typically detritus and were eliminated from the data set. We identified neural cell nuclei in the GUI as blue hematoxylin regions surrounded by brown neurofilament, and only nuclei-containing soma were used for cell body population size analysis. We included cell bodies without nuclei for general density mapping.

Note that for the purposes of this study, we will refer to the three spatial dimensions of the DRG as follows: the axial position refers to the location of an image along the nerve trajectory, and may be either spinal (close to the spinal cord) or peripheral (away from the spinal cord); cross-sections are oriented with the dorsal side up and the ventral side down; the axis perpendicular to both these axes, and horizontal in cross-sections, is the rostral-caudal axis. We determined this final label by considering the *in situ* anatomy of lower lumbar nerve roots, which exit the spinal cord slightly more perpendicular than parallel [97], and therefore to align the third axis with the rostral-caudal bodily axis. If the nerve roots were slightly more parallel to the spinal cord, it would be appropriate to refer to our rostral-caudal axis as lateral-medial respectively. A previous computational modelling study of lower lumbar DRG also used this nomenclature, shown visually in the Coordinate System section of FIGURE 7, [42].

Cell Density Mapping

In order to quantify neural cell densities across DRG, we normalized the location of each identified cell body and axon within an image to polar coordinates using a method similar to Ostrowski et al. (2017) [49]. We set the centroid of the user-defined DRG region as the origin for determining the polar angle of neuron *n* (θ_n). We defined θ_n to equal 0 at the vertical (i.e. dorsal)

normal vector calculated from the user-defined DRG region. We determined radial location (r_n) by calculating the ratio of the distance from the DRG centroid of neuron *n* and the distance from the DRG centroid to the DRG edge along θ_n. The end result is a circular map with the circumference representing the DRG edge and all neurons located inside the circle. In cases where we observed multiple ganglionic regions (i.e. multiple cell body-containing fascicles) in a single slice, we combined all regions into a single region with a compact boundary. We calculated cellular densities by binning normalized neural centroid locations into a grid of annular sectors, which are the shapes formed by slicing a circle into both rings and wedges, then dividing by the non-normalized area of that sector (the original image area it contained).

A shortcoming reported by Ostrowski et al. was a very high variance in calculated densities in sectors at the center of normalized DRG, apparently the result of very small sectors produced by using wedges of constant angular size [49]. We overcame this issue by instead using sectors of roughly constant area by varying the number of annuli and the number of sectors used in annuli of different radius (i.e. inner annuli have fewer sectors). Given that the largest expected cell bodies in human and other large mammal DRG have a diameter of about 100 µm [67], [98], we chose annulus width and sector area to accommodate approximately 4 large cell bodies packed in each sector. We chose this size after trial and error as a compromise between fine and coarse resolution for the final maps. FIGURE 7 Step 3 shows a summary of image analysis steps.

To determine axial position of each image, we fit a 3rd degree polynomial curve to the DRG fascicle areas considering the known distance between sequential images. We took the axial position corresponding to the maximum value of the fit curve as 0 µm (i.e. the middle of the DRG). We assigned a negative axial position value to images on the spinal side of the

midpoint, and a positive value to images on the peripheral side. We did not assign an axial position to images without a clear center (fascicle areas with no peak value).

Donor Demographic Trend Analysis

We performed all statistical analyses for this study using JMP Pro 14 statistical software (SAS Institute, Cary, NC). We tested the effect of various donor demographic and anatomical characteristics on mean neuron count and density in each DRG. We evaluated the two-factor effects (sex [male/female], side [left/right], and spinal level [L4/L5]) with a Student's t-test. For all tests, we set the significance threshold at p=0.01. We evaluated the effect of donor size by calculating body-mass index (BMI), sorting donors into "normal," "overweight," and "obese" categories (group divisions at 25 and 30 [99]), then performing an analysis of variance (ANOVA) test for significance followed by a Tukey honest significant difference (HSD) test. We evaluated the effect of donor age by fitting a line to the density (or count) versus donor age data and assessed the significance of the parameter estimates.

Spatial Density Modeling

We used JMP to fit separate partition models for normalized densities by spinal level (L4 and L5) and neural element type (soma and axons), for a total of four models. Partition models split a distribution of dependent variables (e.g. cell body density) into sub-populations of distribution based on the values of one or more independent variables (e.g. axial location). This splitting operation is performed recursively, and splits distributions at values of independent variables which maximizes model fit. The result of a partition model is a decision tree that maximally captures sub-populations of distributions within a dependent variable (e.g. identifying regions of large or small cell body density based on axial location in the DRG). We

used ten-fold cross-validation of the model at each split to avoid overfitting. We terminated splitting at the stage when 10 additional splits failed to improve the model R^2 by at least 0.05. We additionally restricted the model to only produce groups containing more than 5% of data points, leading to a theoretical maximum of 20 groups in the model. As in Ostrowski et al. [49], we used radial location and vertical angle as model inputs. We defined vertical angle as the angle measured from the top (dorsal-most) point of the circle, reflected across the midline. For our partition models, we also added axial position as a model input. We assessed the output models by performing an ANOVA and Tukey HSD test on the measured densities in the identified spatial regions. Where relevant, results are presented as mean ± standard deviation.

DRG Reconstruction

We reconstructed the 3D profiles of individual ganglia regions by converting manually-traced 2D profiles of DRG, VR, and compact outer tissue to .svg files in MATLAB, then stacking and interpolating (lofting) between the curves using the CAD program Audodesk Fusion 360 (Autodesk, San Rafael, CA), slightly adjusting image alignment as needed. We used these 3D reconstructions to analyze the mean geometric properties (e.g. aspect ratio, length, width) of root regions (e.g. dorsal root, ventral root).

Results

Donors and Specimens

A total of 34 DRG were collected from 10 human donors (TABLE 1 provides demographics for each donor). This included 7 males and 3 females, of which 7 were Caucasian, 2 Hispanic and 1 Black. Ages ranged from 25 to 59 yrs (47.2 ± 10.3 yrs). BMI ranged from 24 to 38 kg/m^2 (30.1 ± 4.5 kg/m^2). Based on typically reported ranges, 2 of the donor BMIs were

considered “Normal,” 4 were considered “Overweight,” and 4 were considered “Obese”. Seven of the donors died from natural causes (cardiovascular or stroke), and 3 died from external causes (trauma or asphyxiation).

Bilateral L5 DRG were collected from all donors, and bilateral L4 DRG were collected from all but 3 donors (D3, D5, and D8). In all but D10, the DRG were identifiable as either left or right upon receipt. Therefore, D10 was excluded from al left-right analyses, but was used when comparing features across levels (i.e. L4 vs. L5). All but one DRG collected had images suitable for inclusion in this study. Tissue slices in all images from Donor 1’s Right L5 DRG were torn and therefore unusable. DRG collected and used are reported in TABLE 1.

TABLE 1: Detailed donor information. F=female, M=male, C=Caucasian, H=Hispanic, B=black. ICH=intracranial hemorrhage. All DRG collected are listed in “DRG” column, first letter is side (L=left, R=right, X=not specified). Number of images included from each DRG is included in parentheses, with “-i” indicating inclusion of an incomplete DRG (i.e. a DRG that produced one or more images that could not be analyzed with the GUI).

Donor	Age (yr)	Sex	Wt. (kg)	Ht. (m)	BMI (kg/m^2)	Race	Cause of Death	DRG
D1	25	F	70	1.64	24.2	C	Cardiovascular	LL5(4), RL5(0)
D2	46	M	81	1.67	27.2	C	Arrhythmia	LL4(5), RL4(5-i), LL5(6), RL5(5-i)
D3	57	M	91	1.62	32.4	C	ICH/Stroke	LL4(6-i), RL4(5-i), LL5(5-i), RL5(5)
D4	49	M	112	1.69	36.5	H	Head Trauma	LL4(3-i), RL4(8), LL5(7), RL5(4-i)
D5	50	F	94	1.52	37.9	C	ICH/Stroke	LL5(6), RL5(6)
D6	54	M	97	1.76	29.0	C	ICH/Stroke	LL4(6), RL4(8), LL5(8), RL5(8)
D7	59	M	93	1.74	28.6	C	Head Trauma	LL4(5), RL4(5), LL5(3), RL5(7)
D8	46	M	88	1.81	24.9	C	Head Trauma	LL5(10), RL5(9)
D9	51	F	92	1.64	31.2	B	Cardiovascular	LL4(5), RL4(7), LL5(8), RL5(9)
D10	35	M	87	1.67	29.2	H	Asphyxiation	XL4(4-i), XL4(5), XL5(8-i), XL5(7)

The majority of DRG in our data set (28/33) could be defined as monoganglia, that is, at some point we observed an image containing a single compact DRG fascicle. All of these DRG split at either the spinal or peripheral side into multiple fascicles, and in some cases were split into two primary fascicles throughout most of the region of interest. The remaining 5 DRG were biganglia, that is, the minimum number of observed DRG fascicles was two. It is possible that these DRG had a merged region in between images not captured by our sectioning, but the maximum length of this region would necessarily be less than 1 mm due to our sampling method. Of the biganglia, 3 were L4 DRG and 2 were L5 DRG. FIGURE 8 shows four samples of

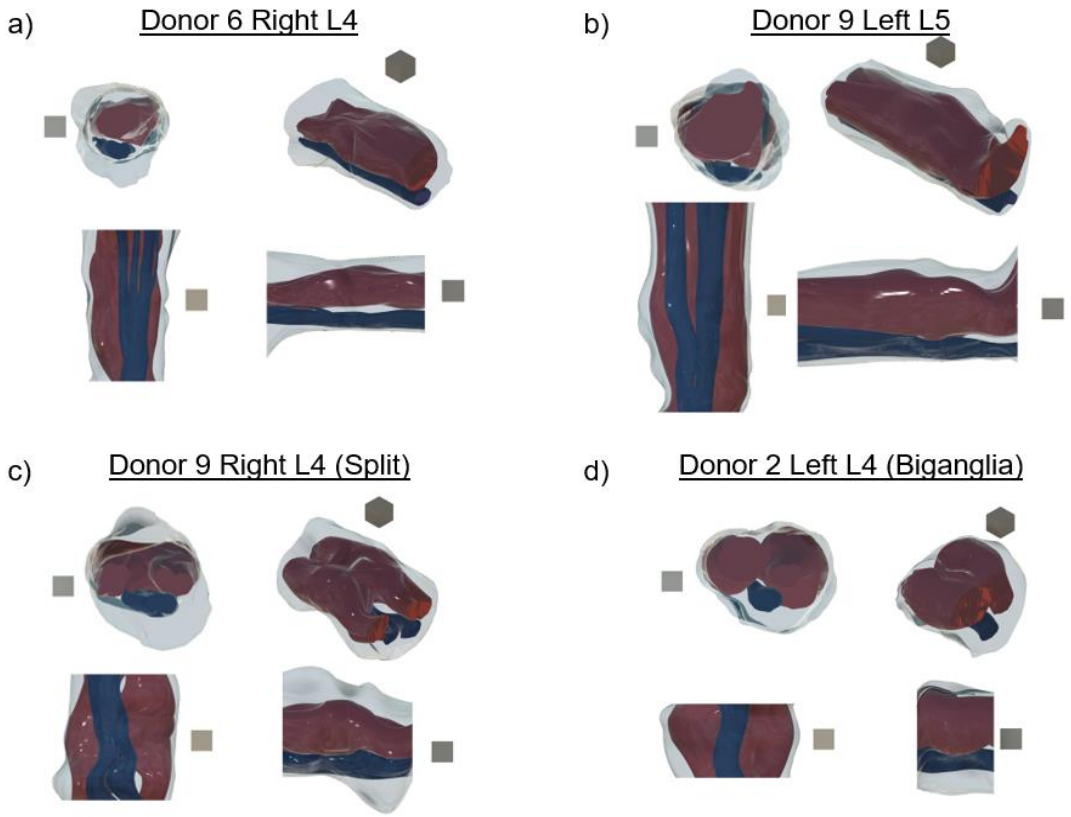

FIGURE 8: Four views of reconstructed DRG specimens. Dark red is DRG region, blue is VR, grey is epineurial tissue. In each group views are (clockwise from top left): Axial (spinal face visible), isometric (spinal face right), rostral (spinal face right), and ventral (spinal face down). Blocks shown for scale have 1 mm edges. (a) L4 monoganglia (b) L5 monoganglia (c) Near-biganglia (d) Full biganglia

donor specimens reconstructed from histological images (one each of monoganglia L4 and L5, a near-biganglia, and a full biganglia).

The number of images used from each DRG ranged from 3 to 10 (6.1 ± 1.8; 202 total), varying due to anatomical differences and the quality of the final images. We imaged 17 complete DRG, identified based on a distinct continuous axial region with soma-containing images bounded by images with only axon-containing images. An additional 7 DRG were considered "nearly complete," with the region of soma-containing images bounded on one side by axon-only images and on the other by highly fascicular images with few cell bodies. The remaining 9 DRG were incomplete (i.e. some regions of the tissue did not have images of sufficient quality to be analyzed with the GUI), but still had images useable for the study. Completeness and number of images used is also reported by DRG in TABLE 1.

Measurements and Reconstructions

Within the complete DRG, there was a non-significant trend toward L5 being longer than L4 ($p=0.0244$). L4 DRG had length 5.2 ± 1.9 mm while L5 DRG had length 7.1 ± 2.4 mm, measured as the length of the soma-containing region. Within the DRG containing a peak area, there was no apparent difference between L4 and L5 in maximum rostral-caudal width, and the overall width was 5.8 ± 1.0 mm. In these same DRG, there was a non-significant trend toward L5 having a larger maximum dorsal-ventral width than L4 ($p=0.0228$). L5 had a maximum dorsal-ventral width of 4.5 ± 1.2 mm while L4 was 3.7 ± 0.8 mm.

Our polar model transforms the DRG fascicular area to a perfect circle of radius 1, but it is useful to understand the typical shape of our actual samples. We found that the actual mean aspect ratio of the DRG fascicular regions (as rostral-caudal width over dorsal-ventral width)

was 1.52 ± 0.47, significantly different than the unit aspect ratio of a perfect circle (Student's t-test, $p<0.0001$). When considering the number of DRG fascicles, we found that the mean aspect ratio of biganglia DRG fascicle cross sections (1.78 ± 0.44) was significantly higher ($p=0.0004$) than for monoganglia DRG (1.47 ± 0.45). This feature of the DRG fascicle cross sections does not extend to the full tissue cross-section including VR, which had an aspect ratio of 1.04 ± 0.21 which, while significantly greater than 1 ($p=0.0039$), does not have a meaningfully larger value. Our polar model does not rely on any assumptions of aspect ratio, but these geometric trends may be of interest for future models of DRG.

GUI Image Processing and Comparison to Human Performance

Precision of the algorithm was 0.92 ± 0.04 and recall was 0.81 ± 0.05. While this is short of perfection, these values are consistent with other well-performing cell segmentation programs (Al-Kofahi, Lassoued, Lee, & Roysam, 2010; Peikari & Martel, 2016; Wienert et al., 2012). In comparison, the inter-human precision was 0.84 ± 0.06 (significantly lower than the algorithm, $p=0.0021$), and inter-human recall was 0.86 ± 0.07 ($p=0.1075$). These values suggest that the algorithm is behaving overall like an average human validator, and on the basis of

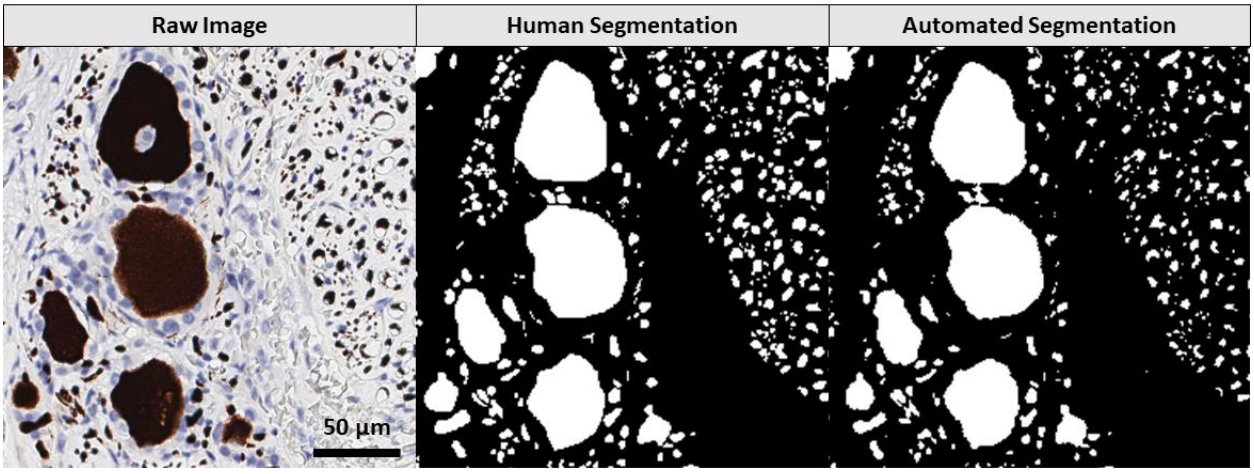

FIGURE 9: Sample of GUI output (left) Raw portion of validation image. (center) Binarization of human segmented image. (right) Binarization of automatically segmented image.

precision and recall would likely be indistinguishable. The absolute difference in object count between human and algorithm was 5.43 ± 4.21 % (non-absolute difference: 1.45 ± 6.89 %, not significantly different than zero (p=0.4806)). The standard deviation of inter-human count for a given image as percentage of the mean was 5.43 ± 4.21 %. Ultimately, the goal of the program was not to perfectly label all cells but to reduce the time to adequately label an image so that trends could be quantified. Each human annotation of a 1 mm^2 image took approximately 6-10 hours depending on the number of objects, and there was considerable variation in duration between annotators. The same images took only ~1 minute for the program. This time saving, along with the positive performance metrics, meant that the program was a significant improvement over manual image labeling.

FIGURE 9 shows a portion of a raw validation image between the automated and human segmentation for comparison. In the full version of this image, the program identified 5277/5359 objects, or an error of -1.53%. Precision in this image was 0.95 and recall was 0.80. A note on human versus automated performance is the tendency of human segmenters to label an object with a border larger than the actual object (oversegmentation). This explains the evident difference in some object sizes between the two images.

Neural Counts and Densities

We observed several trends in cell body and axon count related to spinal level. L5 DRG had significantly higher mean axon count in each image (33643 ± 11007) as compared to L4 (27868 ± 10846), with p=0.0002. However, the mean density of axons did not differ significantly by spinal level, and the combined mean was $2.36 \times 10^{-3} \pm 8.50 \times 10^{-4}$ axons per μm^2. There was no significant difference in the number of cell bodies in each image by spinal level, though there

was a slightly higher mean cell body density in L4 ($3.78x10^{-5} \pm 1.98x10^{-5}$ cells per μm^2) than in L5 ($3.24x10^{-5} \pm 1.71x10^{-5}$ cells per μm^2), with p=0.0492. The combined mean number of cells per image was 469 ± 303. The apparent disparity between a difference in fiber count and a non-difference in by-image cell count appears to be the result of the additional length of L5 to contain the additional cell bodies. From this point, all figures and models will consider L4 and L5 separately.

Comparing the spinal and peripheral sides of each DRG (splitting at the center axial location), we observed that the peripheral side had significantly more axons than the spinal side at both spinal levels (difference at L4: 6002 ± 5917 axons, p=0.0033; L5: 7758 ± 6398 axons, p=0.0002). This trend was true of 24/29 individual DRG where axial location was determined. For large fibers, this represents a mean increase of 4007 ± 4118 fibers (or 62.16 ± 76.24%) from the spinal to peripheral side, and an increase of 2964 ± 2825 small fibers (15.4 ± 15.5%). This trend was not accompanied by a significant increase in per-image cell body count. However, when considering cell bodies by size, there was a significant increase in confirmed (nucleated) large cell bodies on the peripheral side versus the spinal side (9 ± 15 cells, or 51.5 ± 77.7 %). The large cell body trend was true of 21/29 DRG, although there was not enough data to determine if this trend was related to DRG level.

It should be noted that large cell bodies represented only about 32.4 ± 18.0% of nucleated cell bodies, and that nucleated cells represented 27.3 ± 8.6% of all cell bodies identified in each image. Medium and small cells respectively represented 43.7 ± 12.6% and 23.9 ± 11.3% of nucleated cells identified. No axial trend was observed in either axon or cell

body density (rather than count) at any size. Possible reasons for these observations are enumerated in the Discussion section.

The most significant trend related to patient demographics was that obese donors had a higher L5 DRG axon count (38298 ± 8783) than normal patients (30934 ± 8522), p=0.0047. Overweight donors overlapped both groups (33113 ± 9609). This trend was also observed in L4, although there were no normal BMI L4 donors (obese: 31171 ± 10383; overweight 26499 ± 9280; p=0.0219). Obese donors had a higher cell body count in each L4 image than overweight donors (p=0.0367), and higher than overweight and normal donors at L5 (p=0.0073 and p=0.0404 respectively). There was no significant cell body count or density trend related to BMI. Female donors had both higher mean L5 cell body count and cell body density than males in each image (p=0.0179 and p=0.0019, respectively).

FIGURE 10 shows the mean polarized densities of cell bodies and axons for each spinal level with axial position divisions at 1 mm intervals. While a full spatial description of VR axons is outside of the primary scope of this study, a few observations are relevant in comparison with the DRG. We counted 5983 ± 1474 axons in L4 VR, and 6417 ± 1564 axons in L5 VR, although the difference was not significant. There was no relationship between axon count and axial location. In each image, the mean number of large axons was 62.6 ± 35.8% the number of small axons, significantly smaller than parity ($p<0.0001$), with no relationship to spinal level. Compared to the DRG, in which the same ratio was 42.4 ± 16.5% and also significantly different than parity ($p<0.0001$), the ratio was significantly higher ($p<0.0001$). This matched our qualitative observation that it was possible to visually discern a VR fascicle from a DRG fascicle based solely on the different axon population size.

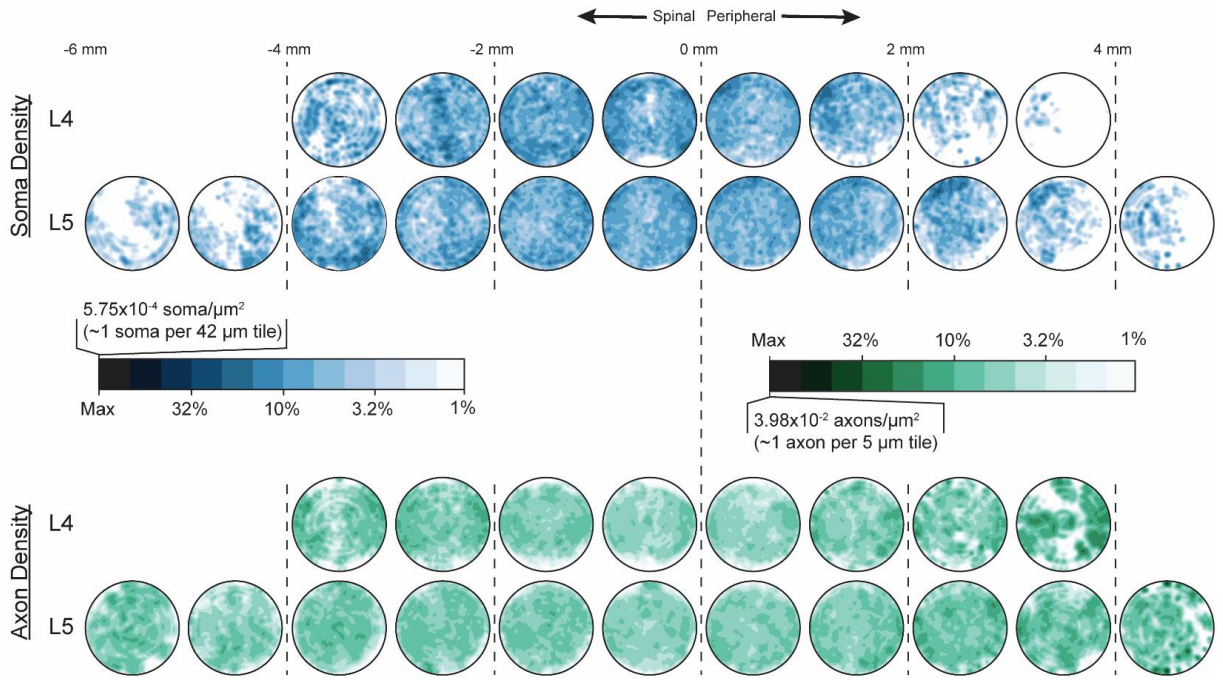

FIGURE 10: Polarized mean cell body and axon spatial densities (blue and green, respectively) in each millimeter of L4 (upper) and L5 (lower) DRG fascicular region. Inset scale left provides reference for color, which is on a logarithmic scale decreasing from maximum density to 1% of maximum. Inset cartoon right shows the anatomical context of each polar graph.

Considering the sizes of the identified axons, there was a sharp drop-off in counted axons with mean diameter below 2 µm (only 0.018% of identified axons). We therefore concluded that our imaging and analysis method was not capable of consistently measuring unmyelinated C fiber axons, which have a typical diameter <1.6 µm [87]. We also may be undercounting small myelinated fibers (Aδ), which have a minimum diameter of 1 µm [87]. This was likely a result of a de-noising step in our image analysis, which could not distinguish very small axons from other cellular detritus. The mean axon diameter was 4.37 ± 1.79 µm. The mean cell body diameter was 44.94 ± 15.13 µm.

The axon and cell densities for each level were modeled using a recursive partition algorithm which had radial, axial, and angular position as inputs. TABLE 1 summarizes the performance of the partition models and the contribution of each input variable to the overall

model as a proportion of the total R^2. For the cell body models, axial position was the most important variable, while the radial position was most important for the axon models. Both the L4 cell body and axon models had a higher R^2 than the corresponding L5 models, although as in Ostrowski et al., the trends described by the model represent a relatively small portion of the overall variation [49]. The axon models also had higher R^2 than the associated cell body models. FIGURE 11 summarizes the measured densities in each spatial region identified by the recursive partition algorithm models, as well as describing the statistical relationships between regions. Each model successfully identified regions with significantly different neural densities, with a minimum ratio of ~2x between highest and lowest density regions (L5 cell bodies) and a maximum ratio of ~7x between highest and lowest density regions (L4 axons). FIGURE 12 shows a spatial representation of the data from FIGURE 11.

TABLE 2: *Summary of DRG density models by neural element and spinal level. R^2 values indicate the amount of variance captured by the partition model for a neural element (i.e. cell bodies or axons) at a given spinal level. Proportion columns indicate the relative contribution of a given variable (e.g. axial position, radial distance from center) to the overall model on a scale from 0-1; proportions for a given model sum to 1.*

Neural Element	Spinal Level	R^2	Axial Proportion	Radial Proportion	Angular Proportion
Cell Bodies	L4	0.0659	0.57	0.21	0.22
	L5	0.0453	0.60	0.28	0.12
Axons	L4	0.1399	0.04	0.61	0.35
	L5	0.0942	0.14	0.81	0.05
Small Axons	L5	0.0835	0.17	0.76	0.07
Large Axons		0.1003	0.26	0.70	0.04

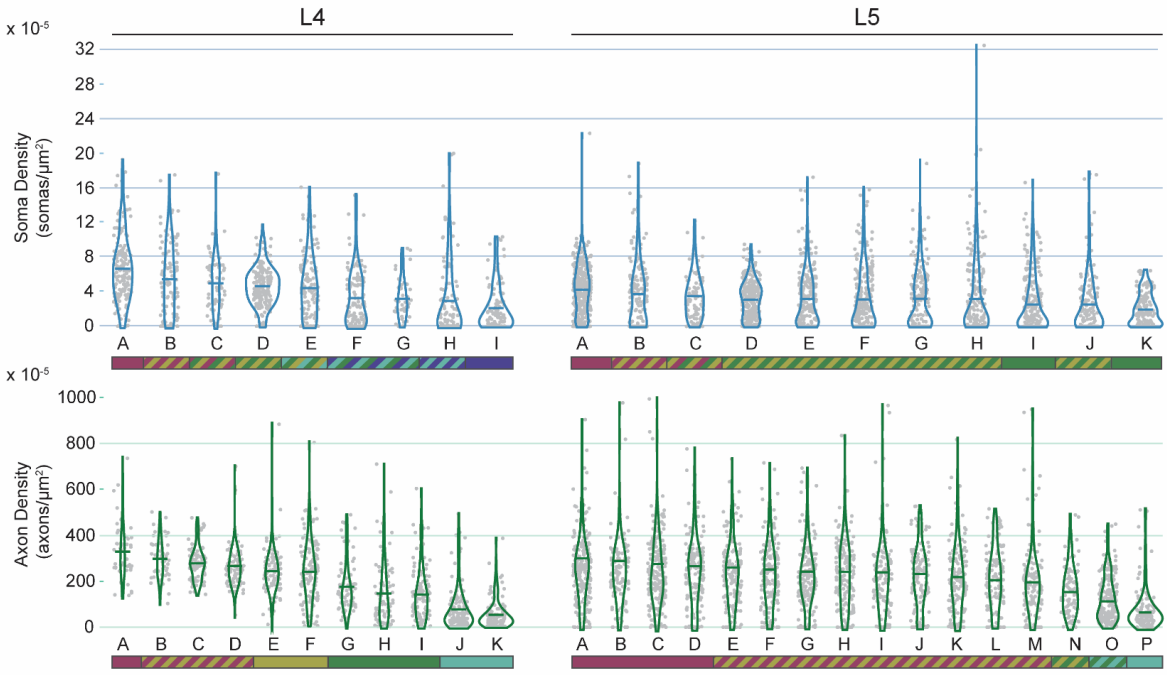

FIGURE 11: Regions from spatial partition models of cell body and axon densities (top and bottom respectively)in L4 (left) and L5 (right) DRG. Data is summarized with a violin plot and a mean bar. Letters are unique to each box plot, although the mean in each group is descending left to right. The colored bar below each plot represents statistical significance. Groups not connected by the same color (either solid or striped) are significantly different from each other. For example, in the top left graph, group A is significantly different from all groups other than B and C, which share its magenta color.

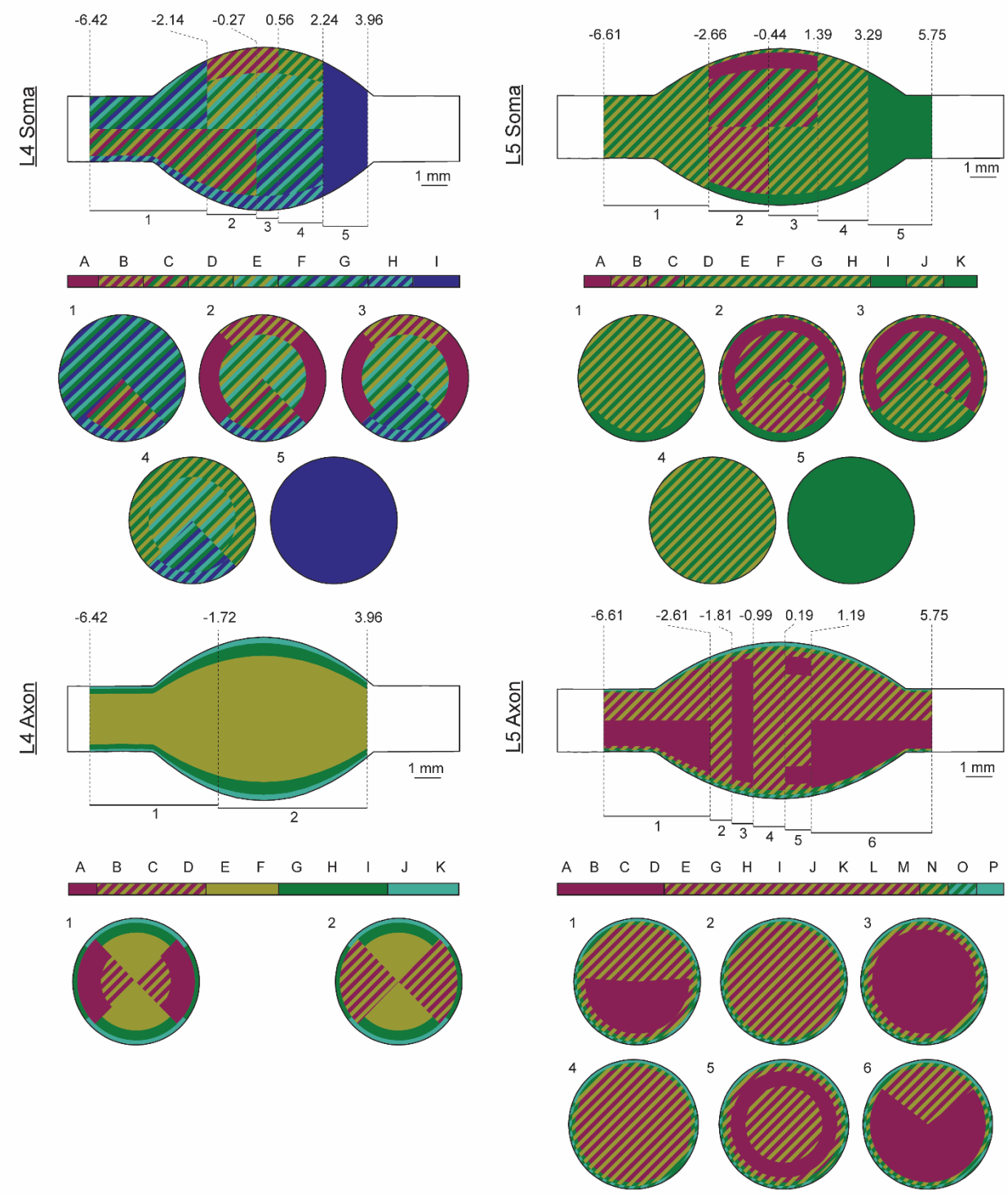

FIGURE 12: Spatial representations of the densities in the DRG partition models. Cell bodies (top) and axons (bottom), L4 (left) and L5 (right). The top of each group is a view of the DRG with the spinal side left and dorsal side up. Within each uniquely described axial region, a slice with corresponding number label is shown below, with dorsal side up (e.g. for L4 somas, slice 1 represents neural densities at axial locations between -6.42 and -2.14 mm from the middle of the ganglion). Values along the axial axis of the DRG have units of mm. Color bars beneath the DRG represent the overlapping groups shown in FIGURE 11 for reference.

Axial position was the strongest contributor to the cell body models. In L4, the highest densities were in the inner ~4.4 mm, and in L5 the highest densities were within the inner ~6 mm. These values both correspond to about 85% of the mean full length of the soma-containing region. For L4, the highest density region was in the dorsal-most 76% angularly and the outer-most 30% radially. The lowest density region (in the inner axial portion of the DRG) was the ventral-most 24% angularly and the outer-most 18% radially. For L5, the highest density region was similarly in the dorsal-most 69% angularly and the outer-most 25% radially, although the outer-most 5% radially was characterized by slightly lower density. The lowest density region was the ventral-most 31% angularly and the outer-most 14% radially. For both levels, the interior was a more homogeneous region. In contrast to the cell body models, radial position was the most important component of the axon models at both levels. Taken together, the highest density regions in the model were within 89% (L5) to 93% (L4) radially. The outer 11% and 7% (respectively) had significantly lower densities. In L4, the medial angles (43°-136°) had the highest density, while in L5 angle played almost no role in the final model.

We also considered differences in modeled densities with neural element size. There were not enough nucleated cell bodies to make size models at either level. At L4, the small and large axon density models were almost identical to the overall axon density model. In L5, however, considering fiber sizes separately changed the model in a few significant ways. The contribution of each input variable to each model and the density distribution in the large axon model were fairly similar to the overall axon model (see TABLE 2 for variable contributions and model R^2). For large axons, the model predicted low density regions throughout the outer-most 8% radially, particularly in the dorsal- and ventral-most 30-35% angularly, and a homogeneously

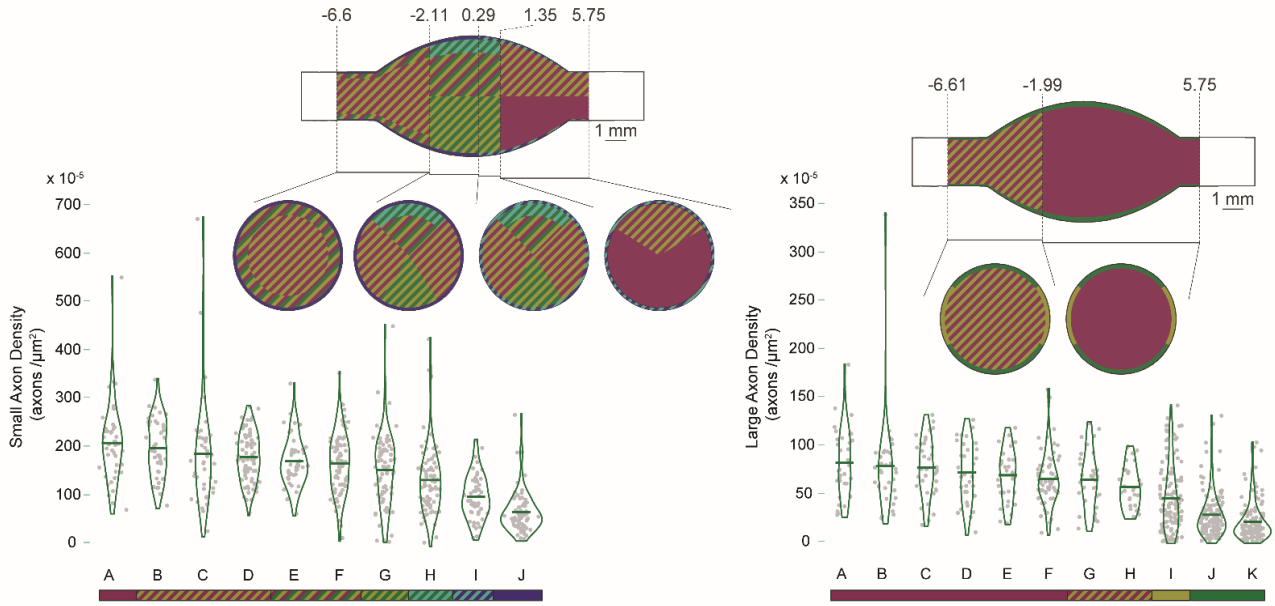

FIGURE 13: Small and large axon density models for L5 (left and right respectively). See FIGURE 11 and FIGURE 12 for specific information on the types of figures shown.

higher inner 92% radially. The small axon model, while retaining an outer low-density region (outer-most 6%), had a unique low-density region at the medial dorsal aspect (-2.11 to 1.35 mm axially, dorsal-most 25% angularly, 28% radially). This dorsal region is particularly important for DRGS applications, so a paucity of small axons in the area may be an important characteristic for ongoing research in the area. FIGURE 13 shows both models as violin plots and spatial models. The decision trees for both models are available in Appendix B.

Discussion

In this study, we analyzed 202 cross-sections across the full span of 33 human L4 and L5 DRG collected from 10 donors. To our knowledge, this represents the largest such collection of human DRG images included in a single study. Additionally, while this study was limited to a description of DRG, the full library of images produced includes over 900 images of human spinal roots, both stained and unstained, for use in potential future studies. We utilized a

custom semi-automated GUI to aid in this analysis and greatly reduce processing time compared to manual image segmentation. This GUI, which relied on the high contrast neural staining provided by the use of NF200 (rather than hematoxylin & eosin), represented a significant improvement relative to our previous study of the feline DRG [49].

Considering our donor demographics, the main effect we found was that the overall number of axons increases categorically with increasing BMI. This translates previous findings in rats suggesting that DRG neuronal numbers increase with body size [100], [101]. As obesity is a common comorbidity to chronic pain, obese patients receiving DRGS may have different neuroanatomical makeups than non-obese patients. It is currently unclear if increased axon counts would have an impact on DRGS outcomes. Future clinical studies should examine the effect of patient demographics, including BMI, on DRGS outcomes. In contrast to previous studies, we did not find evidence that neuronal numbers increase with age [100]. However, our study was likely underpowered to determine this relationship because our sample only included two donors under the age of 35.

A high-level anatomic trend that we observed was the significant increase in axon and cell body number in peripheral DRG compared to the spinal side. This trend is likely related to axonal branching of DRG neurons which has been observed in rat and cat studies, with branching ratios similar to those in our data [69], [102]–[104]. Other explanations may include our underestimation of the number of small C-fiber axons present in our tissue samples, particularly considering that unmyelinated axons account for approximately two-thirds of axons in the DRG [105]. Alternatively, it has been observed that the peripheral side of pseudounipolar DRG neuron axons are slightly larger than their spinal counterparts [21]. Lee and colleagues

demonstrated that nearly 13% of spinal axons in A-fibers have diameters less than 2 microns, suggesting they would not be detected by our algorithm [67]. We found approximately 22% more fibers on the peripheral side of the DRG than the spinal side, a slightly larger portion than Lee and colleagues' findings would suggest. It is possible that because our analysis could not detect very small fibers, there is a population of cells which can only be detected on their peripheral side.

We found a mean 33643 ± 11007 axons in L5 DRG and 27868 ± 10846 in L4 DRG. These counts are consistent with a recent study by Liu et al. which counted human dorsal root fibers and found 34455 ± 2740 in L5 and 31175 ± 2740 in L4 [28]. In both cases, our mean counts are slightly lower, which may be a result of the variance in our data or our undercount of small unmyelinated fibers. However, both our study and Liu et al. stained spinal root tissue with NF200 and used computer programs to determine the number of fibers present, suggesting Liu and colleagues may have also underestimated the number of unmyelinated fibers. Davenport and Bothe reported 59,000 cells in human L3 DRG, with 25,000 unmyelinated fibers contributing to their total population [106]. Davenport and Bothe's estimation of the number of unmyelinated fibers in lumbar DRG approximately accounts for the difference in their estimate of total cellular population with the estimates made by our study and Liu et al. This suggests that both our study and Liu et al. accurately captured the population of many axons in DRG but underestimated the number of unmyelinated axons.

For our primary quantification of human DRG spatial organization, we utilized a recursive partitioning algorithm to model axon and soma densities in normalized DRG cross-sections by axial, radial, and angular position. We found that the highest somatic densities were

within about 2 mm of the widest point of L4 DRG and within 3 mm of the widest point of L5 DRG. Within these regions, both the highest and lowest cell body densities were found in the outer-most 20-25% radially, with the dorsal-most 75% having the highest overall density and the ventral-most 25% having the lowest overall density by angle. We found that axial position had a very minimal effect on axon density, which was much more affected by radial position. The outer ~10% at either level had a very low axon density, while the interior ~90% was relatively high.

Our findings related to soma density are consistent with our previous findings in Ostrowski et al. in feline lumbosacral DRG. That study found the highest density of cell bodies in the outer 25% radially and on the dorsal aspect [49]. As this was a study including DRG from a different spinal region (sacral), it suggests that our general characterization in human lumbar DRG can potential be extended to other spinal levels.

In the VR, we counted 6417 ± 1564 axons at L4 and 5983 ± 1474 axons at L5. These values are again similar to, but slightly lower, than the values reported by Liu et al. (8567 ± 1396 and 7878 ± 1386, respectively) [28].

Implications for Clinical Neurotechnologies

The location of different types of neurons within the DRG is vital to designing clinical neurotechnologies with the goal of treating disease. For example, dorsal root ganglion stimulation (DRGS) delivers electrical stimulation to the DRG with the goal of providing patients with pain relief. Presently, the physiological mechanisms of DRGS-induced pain relief are unknown, though previous studies have suggested that DRGS targets large myelinated DRG neurons [42], while other studies have suggested DRGS targets small unmyelinated afferents

[107], [108]. As the mechanisms become clearer, precisely targeting the cells responsible for pain relief, while avoiding cells that convey painful sensations, will be vital to the success of DRGS and to patient livelihood. Our results indicate that large axons are homogeneously distributed throughout human DRG. However, our data indicate that the density of smaller myelinated axons is lowest in the dorsal region of the middle of the DRG. Therefore, DRGS applied near the middle of the ganglion may simultaneously target the pain-relieving large axons, while minimizing the activation of small myelinated nociceptive fibers.

For neurotechnologies that record signals from the DRG, the location of cell bodies is crucial to obtaining an adequate signal, as cell bodies and their initial segments produce most of the transmembrane currents that lead to recordable neural signals. Such technologies would need to be placed in close proximity to those structures to ensure obtaining a viable signal [38]. Our results support previous findings in cats [49] that cell bodies typically organize around the dorsal aspect of the ganglion. However, our results further demonstrate that this phenomenon is present not only at the most medial portion of the DRG, but over a span of several millimeters around the middle of the ganglion for human lumbar DRG. Therefore, to maximize the likelihood of achieving a viable signal, technologies seeking to record signals from the DRG should target the dorsal-middle portion of the DRG, unless future work should determine a particular somatotopy for the desired sensory modality.

Limitations and Future Work

While our results provide a unique quantitative description of human DRG anatomy, there were several limitations to our study design. Firstly, we collected a histological slice at 1 mm increments along the nerve root axis. Human lower lumbar DRG on average range between

7.8 and 11.58 mm in length along the nerve root axis [1], meaning we were limited to between approximately 7 and 11 samples per DRG. Ideally, we would have sectioned an entire DRG with 5 μm slices, to enable a complete reconstruction of the entire cellular population of a ganglion. However, this would dramatically increase the cost of processing even a single DRG, which would have limited us from making comparisons across lumbar levels and across donors. Therefore, we believe that sacrificing slice resolution to enable statistical comparisons was an appropriate choice for our study, as we wanted to gain a rough picture of the stereotactic distribution of neurons in the DRG. Future studies should consider sectioning multiple DRG at a higher resolution, as the monetary and time costs of high-throughput histological processing decrease. Newer tissue clearing and light sheet microscopy techniques may offer opportunities to image DRG cells with minimal sectioning required.

Secondly, we collected DRG from 10 individual donors. As described above, we sacrificed spatial resolution along the nerve root axis to obtain specimens from multiple donors. However, with a sample size of 10 donors, it is unlikely that we are sufficiently powered to make strong statistical claims relating demographic data to the number and distribution of primary afferents in human DRG. Previous work in rats demonstrated an increased number of DRG neurons with increased age and body size [100], [101], and we were able to demonstrate body size differences (but not age differences) in our human data set. A previous study showed that sensory neuron count in human cervical DRG linearly increased with DRG volume , but DRG volume was not shown to correlate with any demographic data (e.g. height, weight) other than a significant sex difference in DRG volume [109] , a parameter we did not directly quantify.

Staining our slides with only NF200 precluded us from making strong conclusions about the functional distribution of afferents in lumbar DRG. NF200 stains for cytoskeletal proteins present in all primary afferents in humans [92], [93]. We believe that NF200 was the most appropriate choice in stain, as it provided sharp contrast between neural elements (which appeared brown in brightfield microscopy) and background tissue. However, the presence of NF200 did not assign a specific sensory function to a neuron (e.g. mechanoreception, nociception). Without information about sensory function, we were unable to make strong claims about the presence of functional somatotopy in human DRG. Co-staining our slides with other neurochemical markers more indicative of sensory function (e.g. TRPV1 or peripherin to stain small nociceptors [110]) would provide more convincing evidence of sensory function, and would allow us to test for the presence of functional somatotopy. Future work may utilize co-staining as an opportunity to examine out both sensory function and anatomical distribution of primary afferents.

Finally, the morphological operations our algorithm used to identify cell location may have individually or in tandem limited our ability to detect the location of very small axon fibers (i.e. < 2 μm in diameter). Unmyelinated C-fiber axons can be as small as 0.2 μm in diameter in cats [67]. The morphology operations our algorithm used to accurately detect the location and diameter of stand-alone neural structures occasionally filtered out objects below 2 μm. However, the range of C-fiber axon diameters in humans is currently unknown. Therefore, it was difficult to estimate how many small neural structures were not captured by our framework. With algorithmic adjustments and images scanned at higher magnification,

however, it may be possible to examine C-fiber population distributions using the same GUI and methods described herein.

Conclusion

The spatial distribution of neural elements in human DRG is important to clinical neurotechnologies seeking to treat neurological disease. We developed a semi-automated algorithm to identify the location of different neural elements in human DRG. We demonstrated that, at lower-lumbar levels, cell bodies preferentially organize around the dorsal-most region of the ganglion, while axons are homogeneously distributed throughout the interior 90% of the ganglion. We also presented a method to reconstruct 3D-models of human DRG based on histological images. Future studies could extend our identification algorithm to probe the presence of functional somatotopy in human DRG or use 3D-model reconstructions as an *in situ* platform for developing novel DRG-interface technologies.

Chapter 4

Flexible Microelectrode Array for Interfacing with the Surface of Neural Ganglia

(previously published in Journal of Neural Engineering, June 2018 [111])

Abstract

Dorsal root ganglia (DRG) are promising nerve structures for sensory neural interfaces because they provide centralized access to primary afferent cell bodies and spinal reflex circuitry. In order to harness this potential, new electrode technologies are needed which take advantage of the unique properties of DRG, specifically the high density of neural cell bodies at the dorsal surface. Here we report initial *in vivo* results from the development of a flexible non-penetrating polyimide electrode array interfacing with the surface of ganglia. Multiple layouts of a 64-channel iridium electrode (420 μm^2) array were tested, with pitch as small as 25 µm. The buccal ganglia of invertebrate sea slug Aplysia californica were used to develop handling and recording techniques with ganglionic surface electrode arrays (GSEAs). We also demonstrated the GSEA's capability to record single- and multi-unit activity from feline lumbosacral DRG related to a variety of sensory inputs, including cutaneous brushing, joint flexion, and bladder pressure. We recorded action potentials from a variety of Aplysia neurons activated by nerve stimulation, and units were observed firing simultaneously on closely spaced

electrode sites. We also recorded single- and multi-unit activity associated with sensory inputs from feline DRG. We utilized spatial oversampling of action potentials on closely-spaced electrode sites to estimate the location of neural sources at between 25 µm and 107 µm below the DRG surface. We also used the high spatial sampling to demonstrate a possible spatial sensory map of one feline's DRG. We obtained activation of sensory fibers with low-amplitude stimulation through individual or groups of GSEA electrode sites. Overall, the GSEA has been shown to provide a variety of information types from ganglia neurons and to have significant potential as a tool for neural mapping and interfacing.

Introduction

Dorsal root ganglia (DRG) are spinal root components that hold significant promise as neural interface sites, particularly for open- or closed-loop sensory neuroprostheses. DRG are elongated thickenings of the dorsal spinal roots at each spinal level that contain cell bodies for afferent neurons entering the spinal cord. Cell bodies are particularly useful for neural recording because of the large extracellular voltage fluctuation that occurs around the soma during action potential propagation [44]. Neural signaling involving these cell bodies often remains intact below the level of a spinal cord injury (SCI), so with a proper electrode interface it is possible to record and decode the sensory signals contained within the firing rates of the electrical impulses. Neural decoding has been previously demonstrated both acutely and chronically for monitoring skin sensation, limb position, and bladder pressure using penetrating microelectrode arrays inserted into DRG, sometimes as sensory feedback for stimulation applications [13]–[20].

As a therapeutic technique, a DRG neural interface has the potential to restore function to some of the approximately 17,000 patients who suffer an SCI each year [5]. While an SCI patient's most visible symptom may be limb paralysis, equal or higher priority is often given by patients to development of new therapies addressing impairment of respiratory, bladder, bowel, or sexual functions [6], [7]. Significant effort in the field of neural stimulation has been directed toward functional solutions for SCI patients, including functional electrical stimulation (FES) for direct activation of paralyzed muscles; epidural spinal stimulation for restoration of motor behavior; intracortical stimulation to restore natural touch perception; and stimulation for axonal regeneration [112]–[114]. Microstimulation of DRG could contribute to this effort by using the same neural interface technology for recording to activate primary somatosensory afferents, a step towards restoring sensation [8]–[11], and providing open-loop modulation of bladder pressure through activation of spinal reflex pathways [12], [13].

DRG interfaces also have value in advancing our understanding of neurophysiology. The physiology of complex autonomic and reflex circuits, such as those of the bladder and gut, involves many different neurons across several distinct nerves. Separately accessing each nerve for recording can be unwieldy. In contrast, the DRG at each spinal level serves as a nexus for multiple nerves and therefore allows interface with many different neurons from a single location. Recordings from single sacral feline DRG, for example, has benefited research into lower urinary tract physiology through access to both pelvic and pudendal afferents [13], [20], [115]. Further, some of the nerves and nerve plexi of the autonomic system (including the pelvic plexus) are challenging to interface with because of their very small size peripherally before they join at the spinal root. A DRG interface would mitigate this problem.

Despite the promise of such an interface, there are currently no technologies designed specifically for interfacing with the DRG's unique morphology. In the peripheral nervous system, interfacing is typically accomplished with different types of cuff electrodes, which encircle a nerve branch to insulate the tissue-electrode interface. The current technological standard is a flexible split cylinder of fixed diameter which opens around a nerve and has electrode contacts (typically platinum, platinum/iridium, or stainless steel) on the interior surface [116]. This would be an impractical approach in the DRG, however, as it is surgically difficult to lift the DRG from its anatomical position within the spinal canal. The DRG also does not have a constant diameter, but tapers at either end into the spinal nerve. If the surgical problem is overcome, newer built-to-fit or self-sizing cuff designs could be used. In terms of signal quality, however, cuff electrodes typically present poor selectivity for individual fascicles or neurons [116]. The flat interface nerve electrode (FINE) cuff attempts to overcome this issue by gently reshaping the nerve profile from circular to roughly rectangular. With the fascicles arranged closer to the nerve surface, selectivity is improved for stimulation and for recording of compound action potentials [117]–[119]. While this design appears suitable for chronic peripheral nerve interfaces, based on 3-month implants in felines, it is unknown whether the reshaping approach could be adapted for the soma-containing DRG.

Most studies in DRG utilize micro-wires, Utah-style electrode arrays or floating microelectrode arrays, inserted into the tissue with a pneumatic insertion tool [8], [9], [18], [19], [44], [45], [10]–[17]. While effective for limited recording periods, these electrodes have several shortcomings. First, penetrating arrays have the potential to cause tissue damage and encapsulation. This has been shown in brain and peripheral nerves to be the result of damage

caused by the initial insertion and, more importantly, by micromotion of the very stiff silicon electrodes relative to the neural tissue [46]–[48]. Chronic Utah array studies in DRG suggest a maximum lifetime of a few weeks to a few months, probably due to a greater degree of motion in the spine than in the cranium [10], [13]. The DRG has a curved surface, while the backing of Utah electrode arrays is flat. More importantly, it has been observed that the majority of DRG cell bodies are localized around the DRG periphery, particularly at the dorsal aspect below a sub-100 μm thick epineurium [49], [50]. While it may be possible to assemble short, stiff, multi-site silicon-based devices to access this population of neurons, it is likely that these would have difficulty penetrating through the thick epineurial layer.

These problems may be overcome with the application of a flexible non-penetrating interface. Recording neural activity from the surface of neural structures is a well-established technique. In the brain, micro-electroencephalogram (μ-ECoG) arrays shrink the size and spacing of standard ECoG technologies for recording from large neuron populations at the cortical brain surface. One novel approach to improve conformability to the brain surface was the application of a 2.5 μm-thick polyimide mesh array using dissolvable silk backing. This device was capable of recording optically evoked potentials, though the signal-to-noise ratio (SNR) was somewhat low so recordings had to be averaged [120]. Minev et al. presented a hybrid design for use on the surface of either brain or spinal cord, using a 120 μm-thick silicone substrate to achieve mechanical properties similar to the underlying neural tissue. This design, capable of ECoG recordings (motor cortex) and driving motor behavior through stimulation (lumbosacral spinal cord) was shown in chronically implanted rats to be superior to stiff 25 μm thick polyimide in terms of avoiding mechanical tissue damage, inflammatory response, and

effect on animal motor performance. This study suggested that very thin polyimide, on the order of single microns, might share some of these advantages due to its mechanics [121]. Rodger et al. used a parylene array to record somatosensory evoked potentials from mouse spinal cord, but the electrodes were not suitable for single-unit or multi-unit recording [122]. Polymer substrates serve as better mechanical matches to neural tissue and have been used for insertion into peripheral nerves as intrafascicular recording arrays [51]–[53]. Additionally, the biocompatibility benefits of thin flexible devices will continue to increase their prominence in the field of neurointerfaces, though issues of water intrusion, delamination, and securement will need to be solved for chronic use [54].

The shortcomings of standard arrays and increasing research in the application thin films for neural recording provide an opportunity for evaluation of a thin-film electrode arrays for DRG interface. In this study, we study a Ganglionic Surface Electrode Array (GSEA). Surface DRG recordings have been previously reported in both felines and humans [41]. The results were promising, demonstrating that it is possible to obtain single- and multi-unit neural recordings from the DRG surface. The devices used in that study, however, were adapted from other neural technologies not intended for DRG, which not only did not conform to the DRG surface but required application of active pressure to obtain recordings. This could be problematic in any experiment, particularly a chronically implanted system. Here, we demonstrate fabrication of a custom-designed interface for the DRG surface, having iridium electrodes embedded in a flexible polyimide substrate, and show that it is capable of recording single- and multi-unit sensory signals from the surface of feline lumbosacral DRG. We also

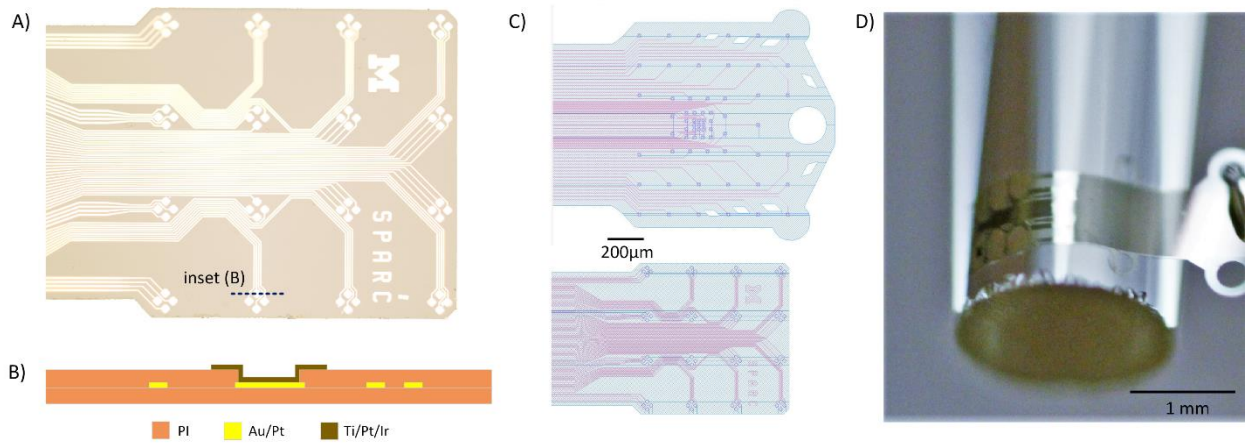

FIGURE 14: Surface array layout A) Microscope image of a finished array. B) Fabrication stack diagram of electrode site (Ti/Pt/Ir) and traces (Au/Pt). C) Schematic layouts of tested arrays. D) Array curving to surface of 2 mm diameter rod.

utilized the buccal ganglia of *Aplysia californica* (Pacific sea slugs) as an important part of our electrode development and testing.

Methods

Ganglionic Surface Array (GSEA) Fabrication

The GSEA was fabricated in the Lurie Nanofabrication Facility at the University of Michigan. The process required four masks and used a 4" silicon wafer as the mechanical substrate. The device substrate was a thin, biostable PI made of BPDA-PDA (3,3',4,4'-biphenyltetracarboxilic dianhydride with *p*-phenylene diamine) [54]. This variety of polyimide was chosen because of its high yield strength, flexibility, and low water absorption [123]. A lower polyimide layer, specifically PI-2610 (HD Microsystems, Wilmington, DE) was spun on at 2.2 µm thick. Lift-off patterning of thin metal interconnect lines allowed for 2.5-µm-wide traces with very high yield. Next the top polyimide layer was spun on, PI-2610 with the same thickness as the lower layer to place the metal traces in a neutral plane. A thin adhesion layer of titanium dioxide was also used above and below the metal stack. The outer structure of the arrays and

the contact openings were patterned with a hard mask and O_2 plasma etching. Using liftoff patterning, a stack of titanium-platinum-iridium was deposited on the top of the polyimide array and into the contact to form the microelectrode metal interface. Both the O_2 etching step and the inclusion of titanium in the metal stack are based on improved metal-polymer adhesion reported by other groups [123]. Impedance of functional (<1 MΩ) 420-μm^2 sites was 515 ± 206 kΩ pre-implant in 10% saline and 503 ± 225 kΩ when applied to a nerve structure (measured using Ripple Grapevine system (Ripple LLC, Salt Lake City, UT)). FIGURE 14 shows the fabrication stack diagram, tested layouts, and an example GSEA.

In vitro Invertebrate Testing

The nervous systems of *Aplysia californica* serve as relatively simple and inexpensive models for testing neural technologies prior to and in parallel with vertebrate *in vivo* experiments [124], [125]. Like vertebrates, *Aplysia* have ganglia containing neural cell bodies and surrounded by connective tissue (~100 µm thick), though this tissue has somewhat different mechanical and electrical properties than vertebrate epineurium [73]. Surface-based multielectrode approaches have previously been used to record from invertebrate ganglia, though only stiff planar arrays have been demonstrated [126]–[128]. The buccal ganglia, responsible for both afferent and efferent innervation of the feeding apparatus, is a particularly well-studied component of the *Aplysia* nervous system and was the *in vitro* ganglia chosen for this study [129]–[131].

Aplysia californica were purchased from the NIH/University of Miami National Resource for Aplysia Facility (160 ± 50 g). Animals were housed in a 40-gallon saltwater tank at 16 °C. To isolate buccal ganglia, a single *Aplysia* was first anesthetized with one-half of its body volume in

~0.3 M $MgCl_2$. Incisions were made in the head region to expose the buccal mass, which contains the mouth parts and associated neural tissues including the buccal ganglia. The ganglia were pinned out in an agar or Sylgard-filled dish (Dow Corning, Auburn, MI) using insect pins, and the dish filled with an isotonic saline solution to just cover the ganglia.

A suction electrode, consisting of chloridized silver wire and isotonic saline inside 0.050-inch polyethylene tubing, was placed near the second buccal nerve, and a syringe was used to pull the nerve into the electrode. Electrical stimulation (Isolated Pulse Stimulator Model 2100, A-M Systems, Carlsborg, WA) through this electrode was used to elicit verified neural activity [132] . A GSEA was placed on the surface of the ganglia for recording action potentials through the Ripple Grapevine processor. In some experiments, a foam-tipped plastic spear was used to press the GSEA onto the surface of the ganglia.

The ganglia were stimulated electrically through the first suction electrode with square waveforms of varying frequencies and pulse-widths to elicit neural activity. Although a variety of stimulus signals were attempted, a typical stimulus was 2Hz, 300µA, 1ms biphasic pulse [132]. Signals were recorded using Ripple Trellis software.

In vivo Feline Testing

Intact, domestic, short-haired adult cats (Liberty Research, Inc., Waverly, NY) were used in non-survival experiments in this study with one cat used per experiment. All procedures were approved by the University of Michigan Institutional Animal Care and Use Committee, in accordance with the National Institute of Health's guidelines for the care and use of laboratory animals. Prior to use, animals were free-range housed with 0–3 fellow felines in a 413 ft^2 room with controlled temperature (19–21 °C) and relative humidity (35–60%), food and water

available ad lib, and a 12 h light/dark cycle. Enrichment was provided by toys and daily staff interaction.

Animals were initially anesthetized with a ketamine (6.6 mg/kg)-butorphanol (0.66 mg/kg)-dexmedetomidine (0.033 mg/kg) intramuscular (IM) dose, intubated, and then maintained on isoflurane anesthesia (2-4 %) during surgical procedures. Respiratory rate, heart rate, end-tidal CO_2, O_2 perfusion, temperature, and intra- arterial blood pressure were monitored continuously using a Surgivet vitals monitor (Smiths Medical, Dublin, OH). Intravenous (IV) lines were inserted into one or both cephalic veins for drug and fluid infusions. Intravenous fluids (1:1 ratio of lactated Ringers solution and 5 % dextrose) were infused at a rate of 5-10 mL/kg/h and increased up to 30 mL/kg/h during surgery as needed. Via a laparotomy, a dual-lumen suprapubic catheter was placed for bladder access. Following a medial incision over the lower lumbar and sacral spine, a laminectomy was performed to expose the lumbosacral spinal cord and DRG (typically L7-S2). Electrode impedances were measured prior to placement in 0.9% saline. A micromanipulator on a magnetic stand was used to support and position the GSEAs, which were lowered into place on the dorsal surface of different DRG, and impedance was taken again. No adhesive was used to secure the GSEAs, which were held down only by surface tension to the moist tissue or with manual pressure via a cotton or foam applicator. The reference wire was inserted into the intraspinal space or nearby muscle. The ground wire was connected to a 12-gauge stainless steel needle inserted under the skin on the left or right flank. With the GSEAs in various positions on the different DRG, neural activity was recorded at 30 kHz using the Ripple Grapevine NIP and associated Trellis software. We simultaneously monitored bladder pressure at 1 kHz through the bladder catheter with a

pressure transducer (DPT-100, Utah Medical Products, Midvale, UT) and analog amplifier (SYS-TBM4M, World Precision Instruments, Sarasota, FL) also connected to the NIP for synchronization.

Various sensory stimuli were applied to activate a range of afferents, though not every kind of stimulus was used in every experiment. To activate skin afferents, the skin was brushed using a cotton applicator in the dermatome associated with the DRG of interest. For L7, this included different regions of the back and legs. For S1 and S2, this included regions of the tail, the anus, and the scrotum (for male cats) [14], [133]. These trials typically involved brushing in bouts of 10 s with 10 s rest periods between bouts. To activate proprioceptive afferents (L7 only), the ankle or knee joint was manually bent. To activate lower urinary tract afferents, room or body-temperature saline was infused through the indwelling catheter in separate boluses of 5 mL until 30 mL had been introduced. Any fluid not voided was removed from the bladder via the in-dwelling catheter.

In some experiments, electrical stimulation was applied (biphasic, 1:2 charge balanced, cathode-leading, 200 μs pulse-width) at low levels (15-300 μA, 7.5 μA resolution) to the DRG through one or more electrode channels, and the animal was observed for corresponding responses.

After completion of all testing, animals were euthanized with an intravenous dose of sodium pentobarbital (390 mg/mL) while under deep anesthesia, followed by bilateral pneumothorax.

Data Analysis

Single-unit action potential timing was calculated in Plexon Offline Sorter (Plexon, Dallas, TX) from the raw neural data by first digitally filtering (high-pass, 250 Hz) then manually applying a negative threshold slightly below the noise floor prior to manual sorting to capture all potential units. For *Aplysia* recordings, spike windows of 3-6 ms were used due to the longer spike duration of these neurons relative to vertebrate action potentials, for which 1.7 ms windows were used. Detected spikes were manually sorted out from noise signals, aided by principal component analysis, in Plexon Offline Sorter, and exported to text files for analysis in MATLAB (Mathworks, Nantick, MA). Low-SNR multi-unit activity is defined here as threshold crossings without a distinct action potential shape which still correlate with an input stimulus. These were detected using a custom MATLAB script with a per-channel threshold set at ±3 times root-mean square (RMS) of the high-pass filtered neural data. Neural data statistics were calculated with JMP (SAS Institute Inc., Cary, NC). Aggregate action potential characteristics were calculated for each unit, including peak-to-valley amplitude and signal-to-noise ratio. Because many of the *Aplysia* trials were contaminated with stimulation artifact and large high-density neural spiking, noise used to characterize SNR was calculated from the median of the raw signal amplitude rather than RMS, as shown in Equation 1 (the expression being multiplied is an estimate of the standard deviation of the background noise, where x is the 250 Hz high-pass filtered signal including stimulation artifact and spikes, and 0.6745 is an empirical correction) [134].

$$Noise = 3 * median\left\{\frac{|x|}{0.6745}\right\} \quad (1)$$

For feline single units, SNR for single- and multi-unit activity was calculated as the ratio of mean peak-to-peak amplitude of the sorted waveform to 3 times the root mean square (RMS) of the noise (filtered signal with unit regions removed). When neural activity was elicited by sensory stimulus, firing rates were calculated using a custom MATLAB script every 0.5 s with a 1 s triangular kernel, and rate was correlated to the stimulus. Due to the high density of our electrode sites, units were often recorded simultaneously on several channels. An unsupervised consensus clustering algorithm developed by Bruno et al. was used to group units by putative source, and detected clusters with identical or similar activity were manually combined [135]. This gave an efficient way to associate the units firing across multiple channels and consider them in aggregate. The spatial extent of these clusters was calculated by multiplying the vertical and horizontal spatial range of active electrodes.

Because the relationship between stimulus and neural firing rates is expected to be monotonic but not necessarily linear (and in the case of bladder pressure, has been shown to have a distinctly non-linear hysteresis [115]), the Spearman correlation coefficient was calculated to determine the strength of the relationship [136]. The brushing, catheter sliding, and joint-bending stimuli in feline experiments were modeled as binary signals corresponding to on/off periods for correlation. Bladder pressure was correlated with neural firing rate directly. When possible, highly significant and convincingly correlated activity ($R > 0.7$ for non-bladder trials, $R > 0.5$ for bladder trials, $p < 0.01$, visually similar) was mapped back to the location on the DRG from where it was recorded to start building a somatotopic map. The cutoff value was chosen to be higher than the correlation of an input stimulus with a baseline recording.

In some feline trials, simultaneous spikes from a presumed single neuron were observed on multiple closely spaced channels. To demonstrate the potential of the GSEA for neuronal mapping, a technique from Lee et al. 2007 was used to estimate neuron source location from features of the simultaneously detected waveforms [137]. The method models the neuron source as a single point located in Cartesian space relative to a tetrode. Equation (2) describes the relationship of the potential V(t) detected at the electrode with the unknown actual source current I(t), the assumed homogeneous conductivity of the medium sigma (σ), and the distance of the neuronal source from the electrode $r_i(x, y, z)$, where (x, y, z) are the three unknown coordinates of the source location:

$$V(t) = \frac{I(t)}{4\pi\sigma * r_i(x,y,z)} \quad (2)$$

Four known values of V(t) must be used to solve this equation's four unknown values. Essentially, the distance from each electrode to the neural source is calculated, and the intersection of these distances is the location estimate. The mean peak voltage of the detected spike on each electrode was used as the feature for calculation, as this is assumed to be most representative of soma firing. No estimate of σ is necessary aside from the assumption of homogeneity, as it cancels out in the final calculation. More details of the linear algebra used for this estimation can be found in Lee et al. 2007 [137]. In some cases, the spikes were detected on a pentrode (5 electrodes), which gave four sets of tetrodes (4 electrodes) for estimation of the source location. In these cases, the mean of the four estimates was used to estimate location, with the standard deviation of each coordinate used to give a sense of the error. Note that since these estimates are not independent, their standard deviation cannot be relied on mathematically, only as an estimate. Additionally, the algorithm used fails if all

electrodes are co-planar. To resolve this issue, one of the electrodes in each pentrode used for calculation was assumed to be slightly out of plane on a spherical surface with radius 100-2500 μm, with real solutions below the electrodes considered to be potentially valid estimates. Increasing radius of curvature gives a "flatter" pentrode. Based on surgical measurements and publications, we assumed the range of S2, S1, and L7 DRG radii are 400±200, 630±200, and 800±200 um respectively, and that the GSEA conforms within this range even if the surface bending is not perfectly conformal [49]. Our estimated range leaves room for slightly larger or smaller curvature.

Results

Invertebrate Results

In total, recordings were attempted in eighteen healthy isolated *Aplysia* buccal ganglia. After several unsuccessful attempts to obtain recordings without altering the ganglia sheath, it became clear that sheath thinning would be necessary to obtain neural recording. Sheath thinning was carried out successfully in seven *Aplysia* ganglia, of which four yielded action potential recordings. This is a much higher success rate than only one of eleven non-thinned ganglia yielding recordings. In total, we report five *Aplysia* ganglia yielding sortable single-unit action potentials (on at least one electrode channel following stimulation of the buccal nerve). The mean number of channels active in successful trials was 19 (range 1-53), and the mean number of units on an active channel was 2.1, with a standard deviation of 1.5 and a maximum of 8. The median peak-to-peak voltage observed was 66.3 μV, and the largest unit had a mean magnitude of 713.0 μV. Noise on active channels had a mean value of 19.4 μV, leading to an SNR ranging from 1.16 to 30.3, with a median of 3.5.

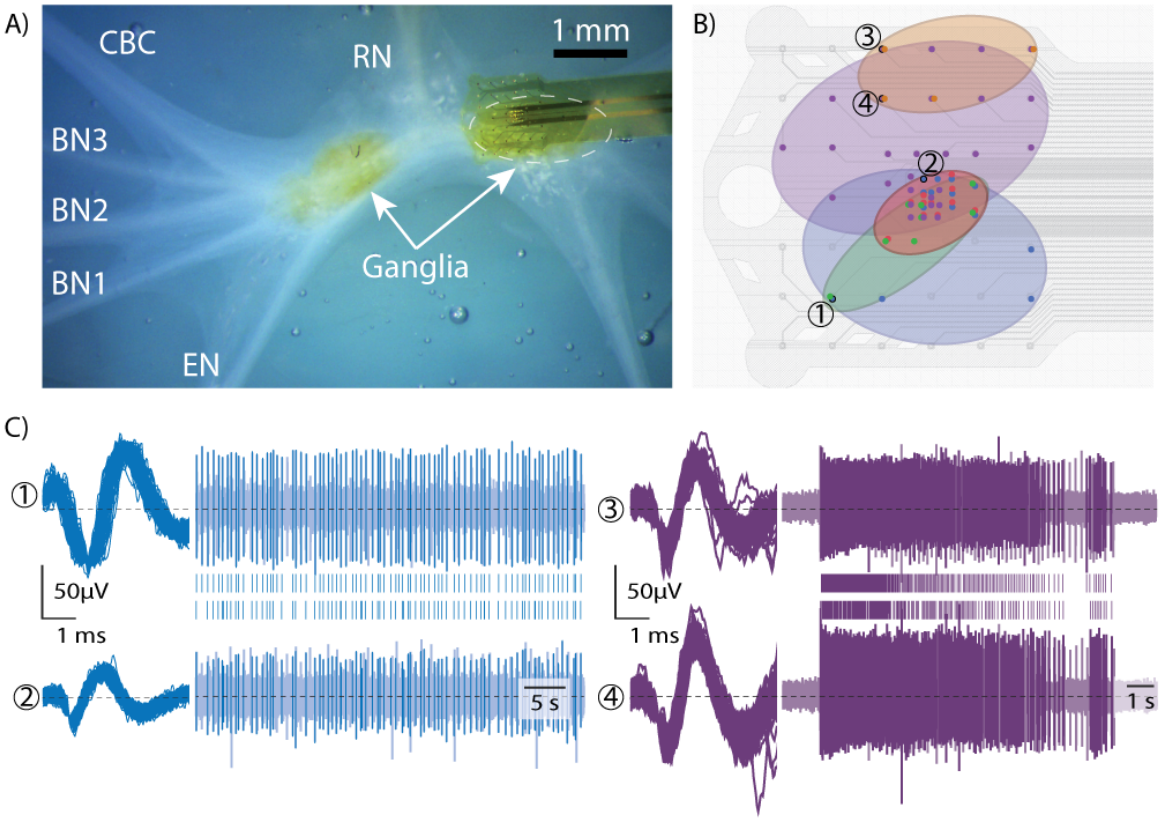

FIGURE 15: Recordings of neural activity from Aplysia buccal ganglia surface A) Brightfield microscope image of array on buccal ganglia, with radular nerve (RN), buccal nerves (BN1-3), cerebral-buccal connective nerve (CBC), esophageal nerve (EN) and ganglia labeled (right ganglion obscured by array) B) Array schematic with 5 regions of similarly firing channel overlaid C) Sample waveforms, raw voltage traces, and raster plots [numbers and colors correspond to those in (B)] Note that the right (purple) unit is on channels with a second unit also recorded, which corresponded to the orange region.

In all but one experiment, individual units were observable on multiple channels. One trial from each experiment was analyzed to summarize the properties of this spatial oversampling. The magnitude of the same unit on different channels varied, with a median ratio of large-channel amplitude to small-channel amplitude of 3.64 (range: 1.38-16.38). The number of channels a single unit appeared on ranged from 2 up to 29, with a spatial range of up to 0.41 mm^2 (median: 0.08 mm^2). For reference, the active surface area of the array was 0.47 mm^2, and the largest cell bodies in *Aplysia* ganglia have a projected surface area of 0.79 mm^2 (1

mm diameter), though most are somewhat smaller (down to 7 μm in diameter, or 38 μm^2) [138].

FIGURE 15 shows the array on the buccal ganglia, a sample trial with spatially oversampled units, and sample waveforms with raw voltage traces and raster plots.

Feline Results

A total of eight cats were used in this study (six male, two female, age: 10–15 months old, 3.9–5.5 kg). In six of eight experiments, we were able to detect single- and/or multi-unit neural activity from one or several DRG, including L7, S1, and S2. Multi-unit activity, defined here as threshold crossings not separable as single units but still correlated with an applied stimulus, was observed in two experiments that also had single units and in three additional experiments for a total of five. In some cases, both single and multi-units were observed during the same trials. Multi-unit activity was observed in response to tail brushing (3 experiments/3 attempted, successful on both S1 and S2), scrotum/genital brushing (1/2, on S2), anal brushing (2/4, on S2), leg brushing (3/7, on L7 and S2), ankle flexion (1/2, on L7), and bladder pressure (1/5, on S2). The neural activity correlation with input was similar for all stimulation types, with a mean of 0.76 and a standard deviation of 0.04. The mean number of active multi-unit channels was 28.5, with a range of 1 to 62. These results are summarized by experiment in TABLE 3, with “Successful Placement” referring to the number of locations at which the GSEA recorded either single- or multi- unit activity. “Active Channels” are calculated on a per trial basis, while the other columns are calculated for each active channel in the experiment. Mean SNR is nearly identical for all multi-unit activity because the threshold for events is set relative to the noise. FIGURE 16 shows samples of this multi-unit activity in response to either

dermatome brushing or bladder pressure, as well as an array map of this activity and an observed somatotopy of the S1 and S2 DRG from recordings in one experiment.

*TABLE 3: Summary of data recorded from feline experiments with neural data (*raw data missing)*

		Single-unit Activity			Multi-unit Activity		
Cat Expt	**Successful Placements**	**Active Channels**	**Mean Peak to Peak (µV)**	**Mean SNR**	**Active Channels**	**Mean Peak to Peak (µV)**	**Mean SNR**
1	2	11.9±3.9	31.1±9.9	3.5±1.1	26.8±4.8	20.1±2.7	1.1±0.0
4	1	-	-	-	39 (1 trial)	32.2±4.2	1.1±0.0
5	1	38 (1 trial)	40.7±6.0	*	-	-	-
6	3	-	-	-	34.7 ± 23.4	26.1±2.2	1.1±0.0
7	2	12.2±5.1	61.9±24.5	3.1±1.1	2.0 ± 1.4	49.3±12.4	1.1±0.0
8	2	-	-	-	26.3 ± 12.6	24.5±3.6	1.1±0.0

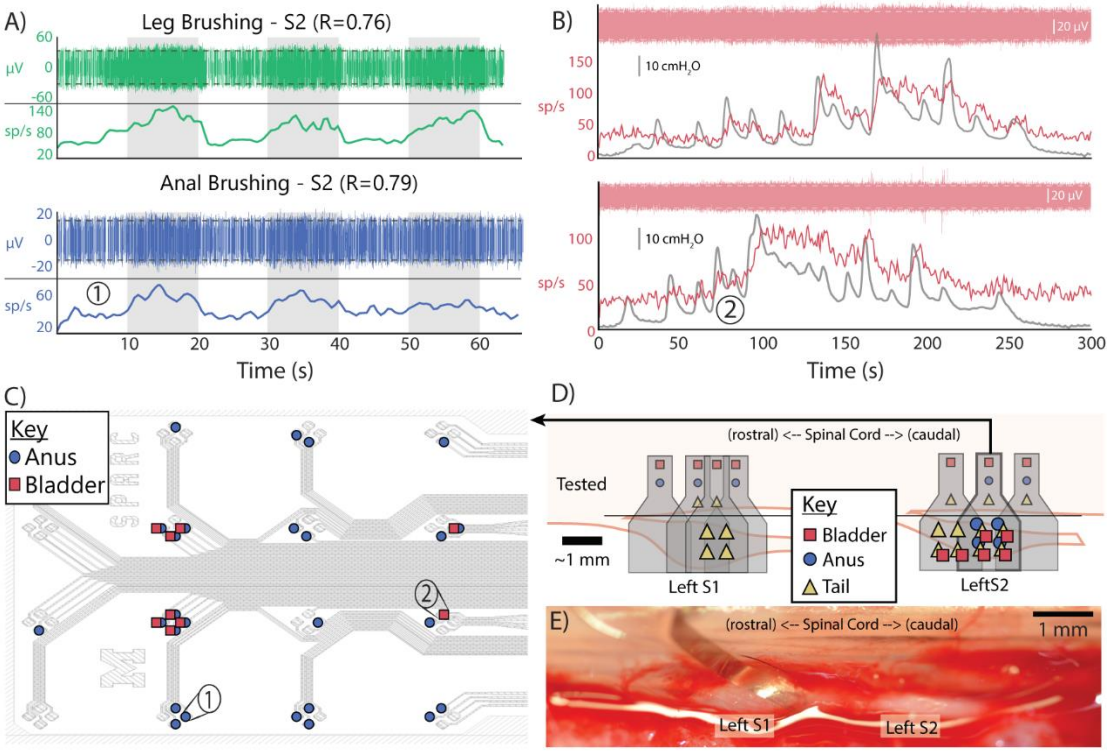

FIGURE 16: Neural recordings from surface of feline sacral DRG A) Multi-unit activity recorded on S2 related to leg brushing in experiment 7 (top) and on S2 related to anal brushing in experiment 6 (bottom). Gray rectangles indicate periods of brushing. Titles indicate correlation. Red dashed lines indicate threshold for unit detection B) Multi-unit activity recorded on S2 related to bladder pressure in two trials of same experiment, including raw data, firing rate, and pressure trace. C) Array map of multi-unit activity from one experiment, indicating channels of bottom figures in (A) and (B). D) Map of detected multi-unit activity in one experiment on left S1 and S2. Gray shapes indicate approximate array locations. Colored shapes above black line indicate inputs tested at each array location. Colored shapes over the DRG indicate detected activity by array quartile. E) In vivo surgical image of array on caudal left S1.

In experiment 6, multiple placements on two neighboring DRG (left side) all yielded multi-unit activity significantly correlated with sensory input, including anal brushing (max correlation: R=0.79), tail brushing (max correlation: R=0.77), and bladder pressure (max correlation: R=0.85) (FIGURE 16 (D)). In this experiment, different stimuli elicited neural activity in different regions of the DRG. Specifically, anal brushing and bladder pressure correlated activity were observed only on the medial region of the S2 DRG, while tail brushing correlated activity was observed on the distal region of the S1 DRG and across the entire S2 DRG.

Single units were elicited in three experiments (1, 5, and 7), with an average of 12.5 ± 10 units per trial on 15 ± 8 channels (out of 64). Sortable single-units ranged in amplitude from 17.3 μV to 158.7 μV, with SNR ranging from 1.1 to 7.3 (observed peak-to-peak noise 31 ± 16 μV). These units were elicited on L7 from joint bending (1 experiment with single units/2 attempted), on L7 from leg brushing (2/7), and on S1 or S2 from tail, anal, or genital brushing (1/5). In one experiment, single units were observed in response to changes in bladder pressure (1/5). The units were observed on a tetrode of sites spaced 30 μm from each other. Correlation of this unit with bladder pressure ranged from 0.49 to 0.61. Though this unit was oversampled on a tetrode, source localization estimates did not converge.

In 5 trials during experiment 1, single units were observed on five pentrodes (five electrodes with 25 μm pitch), allowing for source localization calculations. In 3 of these trials, this activity was detected on two pentrodes. The range of pentrode curvatures for a realistic source location estimate (real and below the electrode plane) was 100 to 2500 μm. In every case the estimated distance of the neural source increased with increasing estimates of the radius of curvature (flatter pentrode). Standard deviation of the estimated location also

increased with curvature, but the rate of change of estimates decreased with curvature. For example, the difference between estimated location for 100 µm and 250 µm was always larger than the difference between 500 µm and 1000 µm. Assuming the flattest curvature in each case, neural sources were detected with estimated depths of 25 ± 1 µm to 107 ± 14 µm and estimated normal distances from pentrode center of 3.8 ± 1 µm to 135 ± 44 µm. FIGURE 17

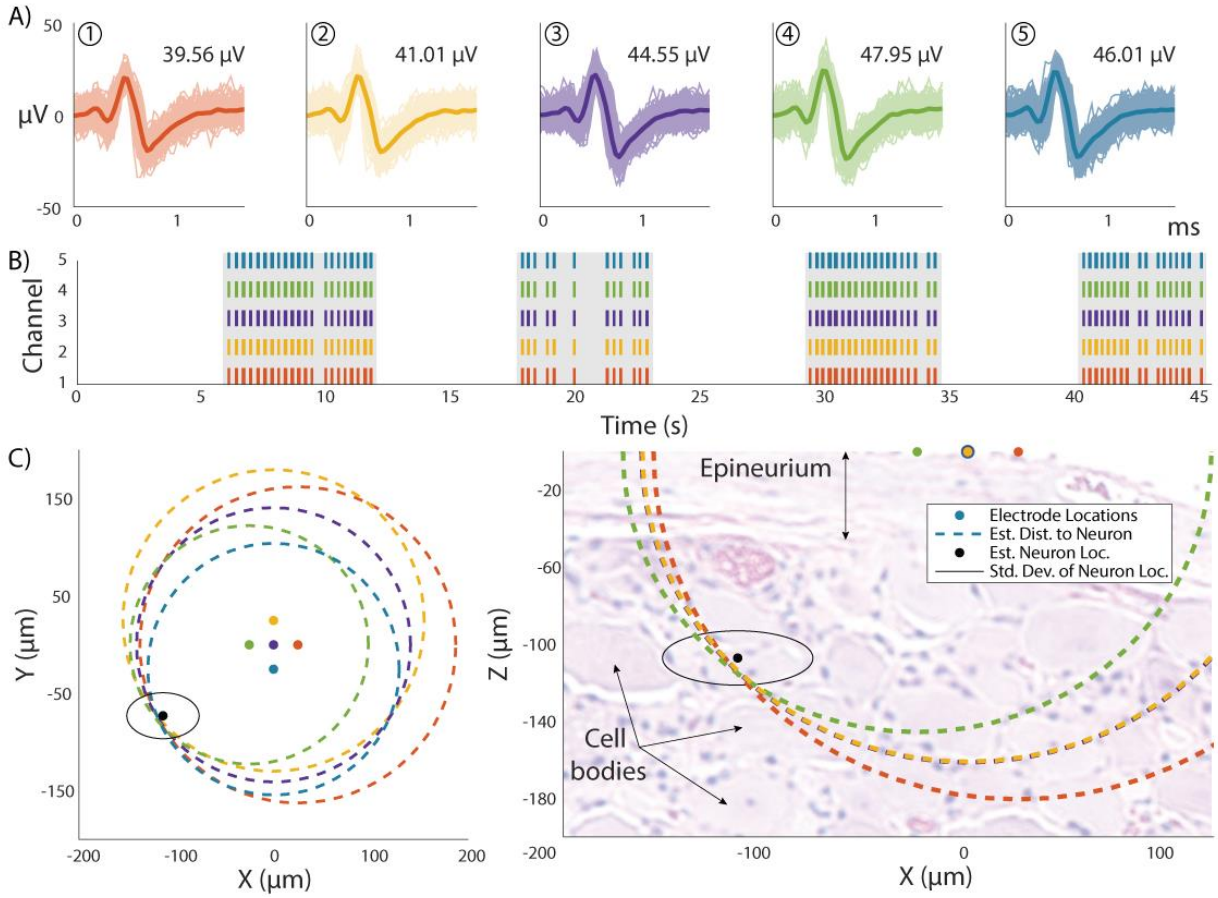

FIGURE 17: 3D source localization from surface DRG recordings A) Single unit detected simultaneously on 5 closely-spaced channels recorded from left L7 DRG responding to leg brushing. Waveforms shown color-coded by channel, with label indicating mean peak-to-peak waveform amplitude. Darker waveform is the mean waveform. B) Raster plot of waveforms in (A), showing simultaneity. Grey boxes indicate periods of leg brushing. (C) Estimate of neural source location. Dashed circles represent estimated distance of source from each electrode (colored circles), and their intersection (black circle) is the estimated source. The black line indicates the standard deviation of the estimate. The left plot is a top-down view through the array. The right plot is a side view axially through the DRG. A representative hematoxylin & eosin-stained DRG (from same experiment) is shown to scale in the side-view. The epineurium and some cell bodies are labeled for reference.

shows the units detected in one of these experiments as well as an estimate of the source location of this unit.

In two experiments (3 and 7), electrical stimulation was applied to sacral DRG through the GSEA. In experiment 3, the right S1 DRG was stimulated. Single-channel stimulation yielded a tail twitch response at a threshold of 300 μA, though this was not present on every channel. With half (32) of the channels stimulated (the maximum for the array connector configuration), the threshold for tail twitching was 22.5 μA. In the second experiment, the GSEA was positioned on left S2. Stimulating on all channels, the threshold for tail-twitching was 45 μA. Stimulating on half (32) or a quarter (16) of the channels, the threshold was 60 μA. The 4-channel threshold was 90 μA, the 2-channel threshold was 120 μA. Rough regional trends in response to stimulation were observed and stimulating channels as close as 250 μm apart yielded different motor responses (tail-twitching or no response).

Raw and analyzed data, and MATLAB scripts used in data analysis, can be found online at [139].

Discussion

In this pilot study of a novel electrode designed specifically for surface-based interface with neural ganglia, we have demonstrated the ability of a flexible thin-film multi-electrode array to both record and stimulate neural activity in invertebrate ganglia (FIGURE 15) and feline DRG (FIGURE 16 & FIGURE 17). Single units detected in *Aplysia* buccal ganglia were often observed on multiple channels simultaneously and had recorded amplitudes of up to 713 μV and typical SNR of 2.63. Single units detected on feline DRG were also observed on multiple channels simultaneously. These single units were often correlated with brushing of associated

dermatome areas or joint flexion. In cases when single units were observed on five closely-spaced electrode sites, we used a source localization algorithm to predict the depth of recorded neurons up to 107 µm (FIGURE 17). We also observed DRG multi-unit activity correlated with dermatome brushing and bladder pressure. In one experiment, data from multiple array placements on multiple DRG allowed for simple somatotopy mapping of neural responses to several different types of sensory stimuli, including dermatome brushing and bladder pressure (FIGURE 16 (D)).

Neural activity was observed in six of eight feline experiments. The two experiments in which no DRG surface recordings were observed were all terminal experiments at the end of chronic implant periods for other objectives [8]. It is possible that a general increase in scar tissue in the region contributed to a lack of results in those procedures.

Previous studies have reported recording from the surface of invertebrate buccal ganglia using glass MEA [126], [127], [140]. These studies were also able to record single-unit activity, with multiple units on single channels and oversampling of units on multiple channels as demonstrated here. While our largest unit (~700 µV) was somewhat bigger than those reported in the previous work (200-300 µV), the typical waveforms were similar in size. A disadvantage of the glass MEA was the need to compress the ganglia against the surface, which by mechanically deforming the neurons could change the native firing characteristics. The GSEA also has the potential to be used in intact buccal mass preparations to study neural network activity together with muscle activity, which would be impossible with a stiff glass MEA [141].

Gaunt et al. (2011) reported single- and multi-unit neural activity recorded from the surface of feline lumbar DRG related to hind limb movement. Our study successfully built on

these previous findings by widening the scope of sensory inputs recorded using the surface array. The largest reported unit had a peak-to-peak magnitude of about 200 μV and SNR of 8.1, which compares favorably with the largest feline unit reported here (magnitude 158 μV, SNR 7.3). While noise was not quantified, the noise in Gaunt et al. appeared to have a peak-to-peak magnitude of between 20 μV and 30 μV, which aligns with the average value of 31 μV observed in this study. Gaunt et al. reported a superior average yield (% active channels) of single unit activity, between 30% and 40% depending on the type of electrode used compared to our average of 23% yield. However, the electrode arrays used in Gaunt et al. had only 16 or 32 electrodes per array, so our 64-channel arrays of similar footprint actually had a greater number of detected single-units.

In terms of multi-unit activity, the GSEA had a mean yield in successful trials of 41%, which is slightly lower than but still comparable to the ~45% reported by Gaunt et al. (not calculated in that study, but estimated based on reported active channel yield and multi-unit/single-unit ratio). The arrays discussed in Gaunt et al. consistently required downward pressure on the array to detect neural signals. While we occasionally used this technique in our research, it was not a necessity in most cases. This represents an improvement in our design [41].

Other than Gaunt et al., observations of single units from surface-based neural recordings with flexible electrode arrays have rarely been previously reported, regardless of target neural location. The only example is Khodagholy et al., who described NeuroGrid, an electrode technology similar to the GSEA but designed for use on the surface of the brain (either neocortex or hippocampus) [142]. While comparison to this study is limited by the

differing application, it is worth noting that the maximum single-unit spike amplitude observed by Khodagholy et al. was approximately 100 µV, comparable to our maximum of 158 µV. Observed RMS noise in their study was 8 µV, which is roughly a peak-to-peak value of 23 µV, slightly lower but still comparable to the 31 µV level in our study. Their noise measurement was taken postmortem, however, which eliminates background biological noise [142].

Other groups have also adapted thin-film technologies for nerve interfacing in peripheral locations. The flexible split ring electrode, presented by Lee et al., is a flat polyimide annulus with gold/platinum electrodes on the inner region to make contact with the nerve. The ring splits at the top to accommodate placement around a nerve, and the inner electrodes bend to make good contact with the nerve surface. In an acute study, this electrode array was demonstrated to evoke compound muscle action potentials and record compound nerve action potentials from the sciatic nerve in rats. This configuration partially solves the problem of attaching a thin film to a nerve, and could hypothetically be adapted for use in DRG with proper sizing and careful surgical technique per the constraints discussed previously [143]. Future implementations of our device could utilize a passive thin-film split ring design to secure the device to the distal and proximal spinal root, with the electrode array remaining on the DRG itself.

A more straight-forward design by Caravaca et al. consisted of a parylene array with a row of tungsten-titanium electrodes of different sizes, both larger and smaller than the sites in this study. This array was demonstrated acutely on the mouse vagus nerve, folded around the nerve to record compound action potentials in response to chemical stimuli. Recording noise was not quantified, but it was reported that the very small sites (225 μm^2) had impedance too

high for recording above the noise floor. While chronic recordings were not reported, histology of 12 week chronic implants suggested limited inflammation around the array [144]. Similarly, Diaz-Butia et al. demonstrated an array of amorphous silicon-carbide insulation with conductive silicon-carbide electrode sites on polyimide backing. This flexible array was shown to record compound action potentials and μ-ECoG on rat sciatic nerve and cortex, respectively [145]. Either of these designs were similar enough to the GSEA to be possibly used on the DRG with similar results.

The primary issue with the use of flexible arrays to record from DRG in this study is the general difficulty of successful and repeatable implant, because of the surgical environment and array properties. Vertebral bone is highly vascularized, and laminectomy can cause bleeding into the implant area. Slow blood pooling impedes visibility of the DRG, making it difficult to place the array and visualize it once in place. The arrays also float on top of the liquid, lifting them from the DRG surface. Bleeding can be controlled to a certain extent with bone wax, absorbent materials, clotting aids, and suction, but each of these have limitations in terms of effectiveness and maintaining visibility of the implant area. Bleeding was highly variable across our experiments and was often a strong predictor of success or failure of the neural interface. Similar implantation challenges would likely be faced by the electrode designs of Caravaca and Diaz-Butia discussed above. The successful application of surface arrays in the brain were likely aided by the lack of significant blood pooling [142]. Vertebral bleeding also occurs for use of DRG-penetrating arrays, though these designs are placed more quickly and secure themselves to the tissue.

The arrays were also difficult to use due to the thin profile and material properties intended to make them superior to penetrating arrays in function. The thin polyimide was difficult to manipulate using forceps without tearing, and so most array placement involved placing the array on a moist surface near the interface target and then sliding it over the DRG of interest. There is a clear tradeoff between device thickness and robust handling. We preferred 4.4-µm thick substrates, but also tested a 3.6-µm thick device and found it more conformal but more easily kinked. Previously, polyimide has been made as thin as 2.5 µm but required a temporary silk coating to manage placement of the recording array [49]. Our concern was this technique would only work here if we could keep the surface dry and quickly secure the array in an accurate position with a microsuture or adhesive. As seen in Fig. 1D, the conformal nature of this material and thickness was good for relatively large DRG, but not ideal. The surface tension of the very light, flexible arrays interacting with fluids will dominate any similar array and even more so for thinner structures. The thinness and weight of the array also made it vulnerable to small air currents and static electricity. We attempted to address this issue by placing Silastic® tubing (DOW Corning, Midland, MI) around most of the array ribbon length to add weight, which worked but came at the expense of array maneuverability. This difficulty in handling was exacerbated by the small size of the target. Feline sacral-level DRG in surgery have an exposed surface area on the order of 0.5-1 mm^2, giving little margin for error in placement. To use these arrays as a tool for mapping the DRG would require the ability to place the array in a repeatable position or positions, which was not possible within the scope of this study. Even with these challenges, through this pilot study we were able to observe a range of neural signals.

We have demonstrated that this type of array, once placed, can successfully record and stimulate neural activity in acute procedures. No method of securing the array was used in any recording, with the exception of some natural fluid thickening around the array that held it in place against light tugging. This is not a problem unique to surface recording, as penetrating arrays in the DRG must have connection wires secured with suture or handled delicately to stay in place in the tissue [13]. A variety of one-off attempts were made to more permanently maintain array position, including application of quick setting elastomers (Kwik-sil™ or Kwik-cast™ (World Precision Instruments, Sarasota, FL)), and cyanoacrylates (Super Glue®-like compounds), both alone and in combination. None of these materials secured the array against the kind of forces that would be experienced in a chronic implant. Further, while recording was attempted after application of these chemicals, no neural activity was ever observed. It is possible that the compounds seeped between the electrode and the tissue surface, blocking conduction. Future design iterations may include eyelets suitable for suturing the array to nearby tissue, such as the spinal cord itself. Khodagholy et al. reported implanting their array stably for 10 days in a rat, with single units maintaining both amplitude and channel location. The study did not report using any kind of adhesive or suture to maintain array position [142]. However, skull-mounted brain implants are subject to much less motion than would be a chronic spinal root implant.

During the course of this study, we evaluated a number of different electrode layouts (Fig. 1D). While the number of experiments with each layout was not sufficient to undertake a formal analysis, we can make a few observations. The GSEAs tested had a range of electrode pitch from 25 µm to just over 1 mm. In the *Aplysia* experiments, the spatial range of single-unit

recording on multiple channels covered about 87% of the active array area. In felines, however, single-units were oversampled only on channels with separation smaller than 35 µm, representing a spatial extent of 900 μm^2 or 0.16% of the active array area of 0.56 mm^2. This is a direct result of differences in cell body size, with the largest feline DRG cell bodies (diameter ~80 µm) hugely dwarfed by the largest *Aplysia* cell bodies (diameter 1 mm) [50], [138]. Related multi-unit activity in felines had a significantly larger spatial extent, up to 100% of the array, so a large active array area also has advantages. This suggests that for vertebrate GSEAs, there should be a balance between maximizing active array area to cover the entire DRG and having sites <35 µm apart to oversample units. Spatial oversampling provides advantages for improved accuracy in spike sorting and for neural source localization, as demonstrated in this study [146], [147].

Future work in *Aplysia* will include simultaneously recording with the GSEA and nerve suction electrodes to establish ground truth validation of which cells are being activated [132]. Further, the GSEA could be used as a mapping tool in an intact preparation of *Aplysia* which includes electromyogram recordings of the buccal mass muscles [141]. It would also be feasible to fabricate an array sized, shaped, and laid out specifically for buccal ganglia recordings, to sample from the entire ganglia or focus on regions of interest to *Aplysia* researchers.

The primary goal of this study, however, was to produce a surface array for acute recording from the surface region of vertebrate DRG. Future work in felines will include performing chronic implants, taking advantage of the less invasive surface-based approach to potentially improve recording life by reducing immune and scarring responses. This potential benefit will depend on whether tissue in-growth occurs under the array, as has been observed

for ECoG arrays, as well as the ability of the array to survive sterilization and long-term implant without delamination [148]. We will also interface with other spinal levels, explore microstimulation further, and continue to investigate electrode geometries. Computational modeling studies will improve our understanding of this interface and suggest design improvements, especially as regards electrical coupling between the GSEA and the epineurium-sheathed tissue. To further leverage the density of our electrode sites, we will use advanced sorting techniques designed for high-density electrode arrays such as those proposed by Jun et al. for their MATLAB JRClust system [58]. We will also perform experiments to validate the proposed source-localization.

Conclusion

We have demonstrated for the first time the ability of a conformable polymer electrode array to record neural signals from the surface of ganglia of different types. We demonstrated the capability of this array to record single-unit action potentials from the surface of *Aplysia californica* buccal ganglia, and the possibility of using the array to map activity throughout the structure. We used this array in acute feline experiments to detect both single- and multi-unit neural activity related to manual stimulation of cutaneous afferents and bladder pressure. We also showed that this type of array could potentially be used to map the sources of neural signals in the DRG with a source localization algorithm. Refinement of the array and handling procedures will allow for repeatable and securable placement necessary before it can be used as a long-term interface. However, because a non-penetrating surface-based approach has significant advantages for neural recording in general and for the specific morphology of the DRG, this approach may have better chronic performance than penetrating arrays.

Chapter 5

High-density Neural Recordings from Feline Sacral Dorsal Root Ganglia with Thin-film Array

Abstract

Dorsal root ganglia (DRG) are promising sites for neural interfacing to record from sensory neurons. Technologies which can monitor sensory activity are useful as research tools toward the development of clinical neural prostheses to treat, for example, bladder dysfunction Current technologies for DRG recording are too stiff to act as effective long-term interfaces, ad do not have sufficient site density to take advantage of advanced high-density neural data analysis techniques. In this study, we performed acute neural recordings in feline sacral DRG using a flexible 60-channel polyimide microelectrode array with site spacing of 30-40 µm. We delivered the array into the DRG with a novel ultrananocrystalline diamond T-profile shuttle designed for high stiffness with small footprint. We recorded neural activity from the DRG during sensory activation, including cutaneous brushing and bladder filling. We successfully delivered arrays in 5/7 experiments and recorded sensory neural activity in 4 of these experiments. Using software designed specifically for analyzing high-density recordings, we identified individual neurons with signals recorded simultaneously across closely-spaced clusters of electrodes. We used this high-density information to efficiently sort the neural

signals and to track individual neurons ad the array was moved through the DRG to simulate the extremes of chronic recording conditions. This study is the first demonstration of flexible electronics delivered into DRG and the first to show high-density recording of DRG afferents with site spacing on the scale of cell bodies.

Introduction

Dorsal root ganglia (DRG) are neural structures with tremendous potential as bioelectrical interface sites, but current technologies available to access, map, and utilize the dense sensory information they contain are limited. As peripheral nerves enter the central nervous system, sensory neurons first coalesce at each spinal level into bilateral dorsal spinal nerves. These nerves, or dorsal roots, each contain a single ganglion, or DRG, which in turn contain the unmyelinated cell bodies of all sensory neurons entering that spinal level. When conducting an action potential, these cell bodies generate a relatively large extracellular potential detectable at single-unit fidelity by nearby recording electrodes [44]. The sensory information that can be decoded from these signals can be used as feedback to control, for example, neural stimulation for bladder control or walking [17], [18], [81], [149]–[151].

However, much remains unknown about neural signaling in DRG. For example, while previous studies have presented some evidence of functional organization within individual DRG, the overall structure-function relationship remains unclear [35], [88]. This relationship has been well-characterized in the brain and spinal cord, allowing for the development of selectively targeted neural interfaces for particular applications. Presently, targeting of DRG is limited to choosing a ganglion at a particular spinal level, for instance, sacral DRG for bladder neuron recording or lumbar DRG for lower limb neuron recording.

The current standard for *in vivo* recording of DRG neurons is the Utah array, a commercially available, silicon-based, penetrating microelectrode array. Previous studies have successfully demonstrated the capability of Utah arrays to record a variety of sensory neurons in the DRG, including populations related to urinary tract function, joint flexion, and skin sensation [12], [17], [18], [81], [149]–[151]. However, the mechanical mismatch between silicon and neural tissue causes tissue damage and scarring *in vivo*, limiting the usefulness of Utah arrays for chronic recording [13] From a neural mapping perspective, a Utah array shank is only capable of recording from a single depth at a given location in the DRG, with a site spacing of no less than 200 µm. Floating microelectrode arrays, a Utah-array like technology with custom shank lengths, is available with a minimum 250 µm site spacing. The smallest site spacing reported for DRG was a stiff silicon probe with 50 µm spacing (a "Michigan" probe) [20]. An ideal mapping technology would be able to record from multiple depths at multiple locations to maximize the number of sampled neurons.

Based on these constraints, a flexible and high-density electrode array would be the preferred interface for mapping within DRG. One way to achieve this is with planar electrode arrays with a thin-film polymer substrate, first described for high-fidelity neural recording in the brain by Rousche et al. (2001) [152]. We previously reported the use of a high-density non-penetrating polyimide array for single-unit neural recording from the surface of lumbosacral DRG [111], as have other studies [40], [41], [153]but biophysical limitations suggest that no units would be recorded below about 200 µm below the surface. Though anatomical analysis suggests that the highest density of somata reside in this outer dorsal region of the DRG [49],

selective DRG mapping or microstimulation will still require a technology capable of recording from the inner space.

In this study, we expand on early results reported in Na et al. to demonstrate the capability of a flexible polymer array for high-density recording and mapping applications in sacral feline DRG [154]. The array was similar in design to the one reported in Sperry et al. (2017) [111], but was delivered into the DRG with a novel structurally-stiffened diamond shuttle. Sacral DRG were targeted because of their potential use as interface sites for bladder neuroprosthetic devices, though the technology could be directly transferred to other spinal levels or neural interface sites. We successfully delivered arrays in 5/7 experiments and recorded sensory neural activity in 4 of these experiments. We used this high-density information to efficiently sort the neural signals and to track individual neurons as the array was moved through the DRG to simulate the extremes of chronic recording conditions.

Methods

The primary purpose of this study was to explore the recording and mapping capabilities of a high-density microelectrode array in feline sacral DRG. Arrays were fabricated in the Lurie Nanofabrication facility utilizing the same process described for the ganglionic surface electrode arrays in Sperry et al. 2018 [111]. In brief, platinum electrode sites were patterned and connected with gold/platinum traces sandwiched in the middle of a 4.5 µm thick flexible polyimide substrate. In this study, each of the 60 sites were approximately square, with an area of 400 μm^2, and arranged in 2 off-set columns. The pitch between electrodes was 40 µm. The active portion of the array was 1160 µm long and tapered from 80 µm wide to 55-µm wide for most of the length of the shank. FIGURE 18 (a) shows a schematic of the array.

Each array was bonded to a custom printed circuit board (PCB) for interfacing with the neural recording system. To reduce site impedance prior to recording, array channels were coated with poly(3,4-ethylenedioxythiophene) polystyrene sulfonate (PEDOT:pSS) as described in Patel et al., with the current adjusted for electrode site area [155]. To verify all deposition and coating steps impedance measurements were taken with a PGSTAT12 Autolab (EcoChemie, Utrecht, Netherlands), controlled by vendor supplied NOVA software. Measurements were obtained by applying a 1 kHz 10 mV_{rms} signal. Custom MATLAB (Mathworks, Natick, MA) scripts were used to determine frequency-specific impedance values. The PCB board was placed in a custom 3D-printed jacket and mounted to a 3D-printed insertion jig (Form2 3D printer, Formlabs, Somerville, MA).

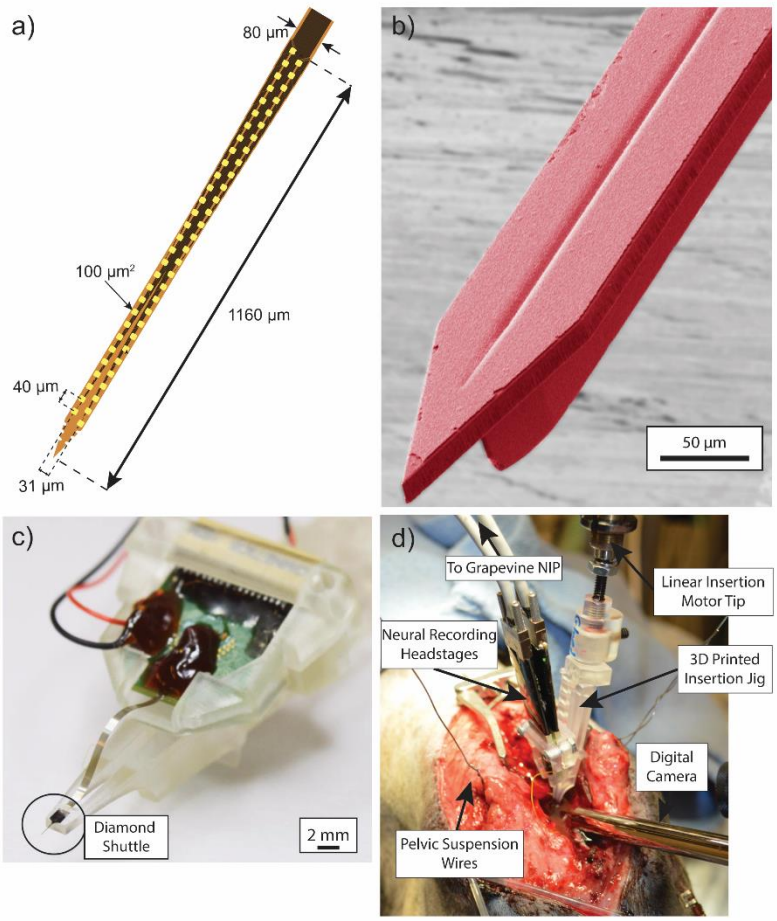

FIGURE 18: Flexible intraneural DRG array (a) Tip of flexible array showing locations of electrode sites (yellow) and dimensions. (b) Diamond shuttle, false color red for visibility. (c) Insertion jig, with location if diamond shuttle highlighted. (d) In vivo *surgical setup over incision site.*

For delivery into DRG, the flexible array was temporarily adhered to an ultrananocrystalline diamond (UNCD) shuttle with water-soluble polyethylene glycol (PEG; 12,000 MW) or ultraviolet-cured cyanoacrylate glue. The shuttle was fabricated with a stiffened T-profile by UNCD deposition over a trench which was etched away to form the final shape (fabrication details and characterization in Na et al. 2018) [154]. The shuttle was 65 µm wide, with a planar 11 µm thickness and the T-profile extending 27.5 µm from the back and having width diminishing from 16 µm to 2 µm. This material and profile increased the buckling load of the shuttle by a factor of 13 as compared to a planar silicon shuttle without the T-stiffened

profile [154]. This design allowed for array insertion without removal of the tough epineurial layer surrounding the DRG, but with presumably less damage to the surrounding tissue. A colorized close-up of the shuttle is shown in FIGURE 18 (b). The shuttle was glued to the end of the insertion jig prior to adhering the array. The combined array, PCB, jacket, shuttle, and insertion jig will be collectively referred to as the insertion assembly. FIGURE 18 (c) shows the insertion jig close-up.

In Vivo Deployment and Neural Recording

Neural recordings were performed in the DRG of intact, domestic, short-haired adult cats (Liberty Research, Inc., Waverly, NY). All procedures were approved by the University of Michigan Institutional Animal Care and Use Committee, in accordance with the National Institute of Health's guidelines for the care and use of laboratory animals. Animals were free-range housed prior to use with 0–3 other male cats in a 413 ft^2 room with controlled temperature (19 °C–21 °C) and relative humidity (35%–60%), food and water available ad lib, a 12 h light/dark cycle, and enrichment via toys and daily staff interaction.

Initial anesthesia was induced with an intramuscular dose of ketamine (6.6 mg kg^{-1})-butorphanol (0.66 mg kg^{-1})-dexmedetomidine (0.033 mg kg^{-1}) intramuscular (IM) dose. Animals were intubated, then maintained on isoflurane anesthesia (2%–4%) during the remainder of the procedure. Respiratory rate, heart rate, end-tidal CO_2, O_2 perfusion, temperature, and intra-arterial blood pressure were monitored continuously using a Surgivet vitals monitor (Smiths Medical, Dublin, OH). Intravenous (IV) lines were inserted into one or both cephalic veins for infusion of drugs and intravenous fluids (1:1 ratio of lactated Ringers solution and 5% dextrose, 5–30 ml kg^{-1} h^{-1}).

A laminectomy (removal of dorsal spinal column bone) was performed to expose the lumbosacral spinal cord and sacral DRG (typically S1–S2). Following laminectomy, the cat's pelvis was suspended from a custom support frame (80/20 Inc., Columbia City, IN) with stainless steel wire and bilateral bone screws in the superior posterior pelvic crest to minimize spinal motion during breathing and bladder filling. A separate stabilizing frame consisting of optomechanical components (Thor Lab, Newton, New Jersey) and custom 3D printed components was assembled around the animal to support a 3-axis micromanipulator (502600, World Precision Instruments, Sarasota, FL) and linear actuator (M-235.5DD, Physik Instrumente, Karlsruhe, Germany). The insertion assembly was mounted to the end of the linear actuator, aimed at either the S1 or S2 DRG, and inserted at 2 mm s^{-1}. Insertion was monitored with a USB microscope camera. FIGURE 18 (d) shows the surgical setup.

The reference wire (and ground wire, when not shorted to the reference on the PCB) was connected to a 12-gauge stainless steel needle inserted under the skin on the flank. Neural activity was recorded at 30 kHz using the Ripple Grapevine Neural Interface Processor and associated Trellis software (Ripple Neuro, Salt Lake City, UT). We simultaneously monitored bladder pressure at 1 kHz through the urethral catheter with a pressure transducer (DPT-100, Utah Medical Products, Midvale, UT) and analog amplifier (SYS-TBM4M, World Precision Instruments, Sarasota, FL).

A variety of sensory stimuli were applied to activate sacral afferent neurons, to map the depth of different neuronal types along the array and to demonstrate the array's potential usefulness for neural prosthesis research. To activate skin afferents, the skin was brushed using a cotton applicator in the sacral dermatome associated with the DRG of interest, including

regions of the tail, the anus, the perineum, the external meatus of the penis, and the scrotum [14], [133]. These trials typically involved brushing in bouts of 10 s with 10 s rest periods between bouts. Visceral afferents of the urethra were activated by sliding a catheter back and forth in the orifice. To activate bladder afferents, saline was infused through the urethral catheter in sequential boluses of 10 mL each.

For measurements of nerve conduction velocity (CV), electrical stimulation was applied (biphasic, 1:2 charge balanced, cathode-leading, 200 μs pulse-width) at low levels (15–300 μA) to the ipsilateral pudendal nerve via an implanted bipolar nerve cuff (2.0 mm inner diameter Silastic 508-009 tubing; 0.4 mm stainless steel Cooner wire contacts [13]). As an alternative stimulation site, a pair of fine-wire electrodes (stainless steel, 50 μm diameter, Model EMT-2-30, Microprobes, Gaithersburg, MD) was inserted near the anal sphincter and stimulated with a similar waveform at a higher amplitude to generate muscle twitch (0.3-4mA).

At the end of each experiment, euthanasia was achieved with an intravenous dose of sodium pentobarbital (390 mg ml^{-1}) under deep isoflurane anesthesia, followed by bilateral pneumothorax.

Data Analysis

In order to efficiently handle the large data sets generated by these recordings, we chose to use the open source IronClust suite for MATLAB, which is specifically optimized for high-density probes that oversample individual neurons [58]. Our spike-sorting workflow using IronClust (developed by James Jun and teams at the Janelia Research Campus and the Flatiron Institute) consists of 1) preprocessing, 2) spike detection & feature extraction, 3) density-graph clustering, and 4) manual clustering. We chose IronClust for its real-time processing speed with

a GPU and its ability to accurately handle the potential probe drift on flexible probes. Each recorded channel was band-pass filtered (300-6000 Hz) and the narrow-band noise peaks were automatically removed in the frequency domain if they exceeded 10 MAD (median absolute deviation) above the median trend curve. Subsequently, the common-mode noise was removed by subtracting each channel by the average across all channels. The remaining motion artifact primarily due to analog-to-digital conversion saturation was rejected by computing the standard deviation of the filtered signals across all channels in each time bin (5 ms duration), and the spike detection was disabled in the time bins exceeding a MAD threshold of 20. The spikes were detected at their negative peaks exceeding 5 MAD threshold [134], and duplicate spikes from the same and neighboring channels were removed if larger peaks were detected within their spatiotemporal neighborhood (50 μm, 0.3 ms). Spike waveforms (1 ms width) surrounding each peak event are extracted from a fixed number of adjacent channels (80 μm). For each spike, we also extracted spike waveforms centered at its secondary peak channel to account for the random jitters of the peak channel due to recording noise and probe drift. Two principal component features were extracted from each channel using a common set of principal vectors for all channels.

In order to handle the probe drift, time bins where the probe occupied similar anatomical locations were grouped together based on the similarity of the 2D histogram of the spike amplitudes and positions. Anatomical snapshots were computed at regular spike-count intervals such that each snapshot contains an equal number of spike events from all channels (20 s average duration). For each snapshot, 2D histogram representing the anatomical features was computed by counting spikes based on their amplitude quantiles (8 bins) and center-of-

mass positions on the probe. Each time bin was grouped with 14 other time bins exhibiting high similarity scores to form a 300 s average duration. *k*-nearest neighbor (k_{NN}, k=30) distances (d_{knn}) were computed between spikes whose peak appeared in channel c and time bin s with the neighboring spikes whose peak or second peak appeared in channel c and time bins that were anatomically grouped with s.

Density-graph clustering was performed based on the k_{NN} [156], [157] by considering a fixed number of local neighbors to achieve a linear scaling. For each spike j, the local density score was calculated ($\rho_j = 1/d_{knn,j}$), and the distance separation score ($\boldsymbol{\delta}_j = d_{min,j} / d_{knn,j}$) was calculated where $d_{min,j}$ is the distance in the principal component feature space to the nearest spike k having a greater density score ($\min(dj_k \mid \rho_k > \rho_j)$). Local density peak points were identified based on a density separation criterion ($\boldsymbol{\delta} > 1$) and the cluster memberships were recursively assigned to the nearest points toward a decreasing density gradient. To minimize false splitting errors due to drift or bursting, units exhibiting similar waveform shapes were merged (Pearson correlation > 0.985). Finally, clusters were manually split, merged, or deleted by using a set of multiple interactive views in the MATLAB-based GUI.

To understand the relationship between sensory inputs and neural activity, we calculated the correlation of either bladder pressure or cutaneous brushing (coded as a continuous binary on/off signal). We used a correlation threshold of >0.4 for bladder pressure or >0.6 for cutaneous brushing to identify related units. A small number of bladder pressure trials, there was a clear visual relationship between the bladder pressure and the firing rate which did not yield a high correlation, and these units were also included. Signal to noise ratio (SNR) was defined as peak-to-peak amplitude divided by the root mean square voltage.

For trials with electrical stimulation, a post-stimulus time histogram (PSTH) was generated for each detected unit. If unit firing had stimulus-locked timing, we used a normal distribution fitted to the PSTH to determine the mean and standard deviation of the delay. To calculate conduction velocity (CV), we assumed a pudendal nerve to sacral DRG length of 9 cm and an anal sphincter to sacral DRG length of 12 cm based on previous measurements [13].

Results

We attempted insertion of arrays in 7 different subjects. In 2 subjects (experiments 2 and 6), no insertions were achieved. This appeared to be the result of fluid on the surface of the DRG wetting the PEG adhesive between the array and the shuttle. This challenge in the first 2 experiments led us to use cyanoacrylate for the remaining experiments. In experiment 7, while insertion of the array was achieved, no neural activity was observed. In each of the remaining 4 experiments, single-unit neural data was successfully recorded, with individual neurons recorded across multiple channels. Impedance of functional electrodes (<1 MΩ; 47 ± 16 channels in 4 experiments) had a median of 142 kΩ (IQ: 364.3 kΩ) implanted. Two of the experiments (1 and 5) had an overall low yield of recorded units, with a maximum of 3 and 6 units recorded respectively. The physical range of channels, physical range of units, number of units, peak-to-peak amplitude, and signal-to-noise ratio (SNR) are reported in TABLE 4.

The median peak-to-peak amplitude of recorded units was typically on the order of 50-60 µV, though the maximum observed cluster center had an amplitude of 1334 µV (a tonically activated unit in experiment 4 with 2.2 ± 0.48 Hz firing rate, modulated to ~3 Hz by anus brushing). The minimum observed single-unit cluster center with sensory correlation had a mean amplitude of 20.5 µV and SNR of 4.21 (bladder-pressure modulated unit in experiment 3,

TABLE 4: Summary of units recorded during all 7 experiments. Grayed out rows were experiments with unsuccessful insertion (2 and 6) or no units recorded (7). Number of driven units is given by unit type: cutaneous (C), bladder (B), electrical stimulation of the anal sphincter (A) or pudendal nerve (P). Number of units by trial, peak-to-peak amplitude, and SNR are given as median with interquartile (IQ) range. For experiment 3, the only experiment with three successful positions of a single insertion, select details about each position are given in rows. See FIGURE 20 for position reference

Expt	**Driven Units**				**All Trial Channel Range (µm)**	**Number of Units**	**Peak-to-peak Amplitude (µV)**	**SNR**
	C	*B*	*A*	*P*			*Median (IQ Range)*	
1	2	2	0	0	300	2.5 (1.0)	61.8 (79.4)	5.0 (2.4)
2								
3 (1)	78	8	22	17	680	27.0 (11.0)	57.3 (64.2)	6.1 (7.6)
(2)	100	14	14	21	1120	24.0 (8.0)		
(3)	57	8	13	20	860	14.5 (4.3)		
4	64	0	21	12	1080	21.5 (14.8)	52.6 (73.4)	5.7 (9.6)
5	5	0	0	0	640	6*	27.8 (38.7)	3.1 (4.2)
6								
7								

correlation 0.64). This was an example of neural activity that might not have been detected using traditional neural unit sorting on individual channels. Other multi-unit activity was observed with smaller mean amplitude, but the unit shapes were poorly correlated.

Bladder pressure related units were observed in 2 of the experiments. An example unit is shown in FIGURE 19 (a), with the waveforms at the five highest amplitude channels shown in FIGURE 19 (d). Cutaneous brushing units were observed in all 4 experiments with neural activity. Units were observed with correlation to scrotal brushing, anal brushing, and brushing the dorsal base of the tail. An example unit related to tail brushing is shown in FIGURE 19 (b), with waveforms also in FIGURE 19 (d).

Units activated by electrical stimulation of the pudendal nerve or anal sphincter were observed in 2 of the experiments. There was no significant difference in the population of conduction velocities elicited by pudendal versus anal stimulation. An example unit is shown in

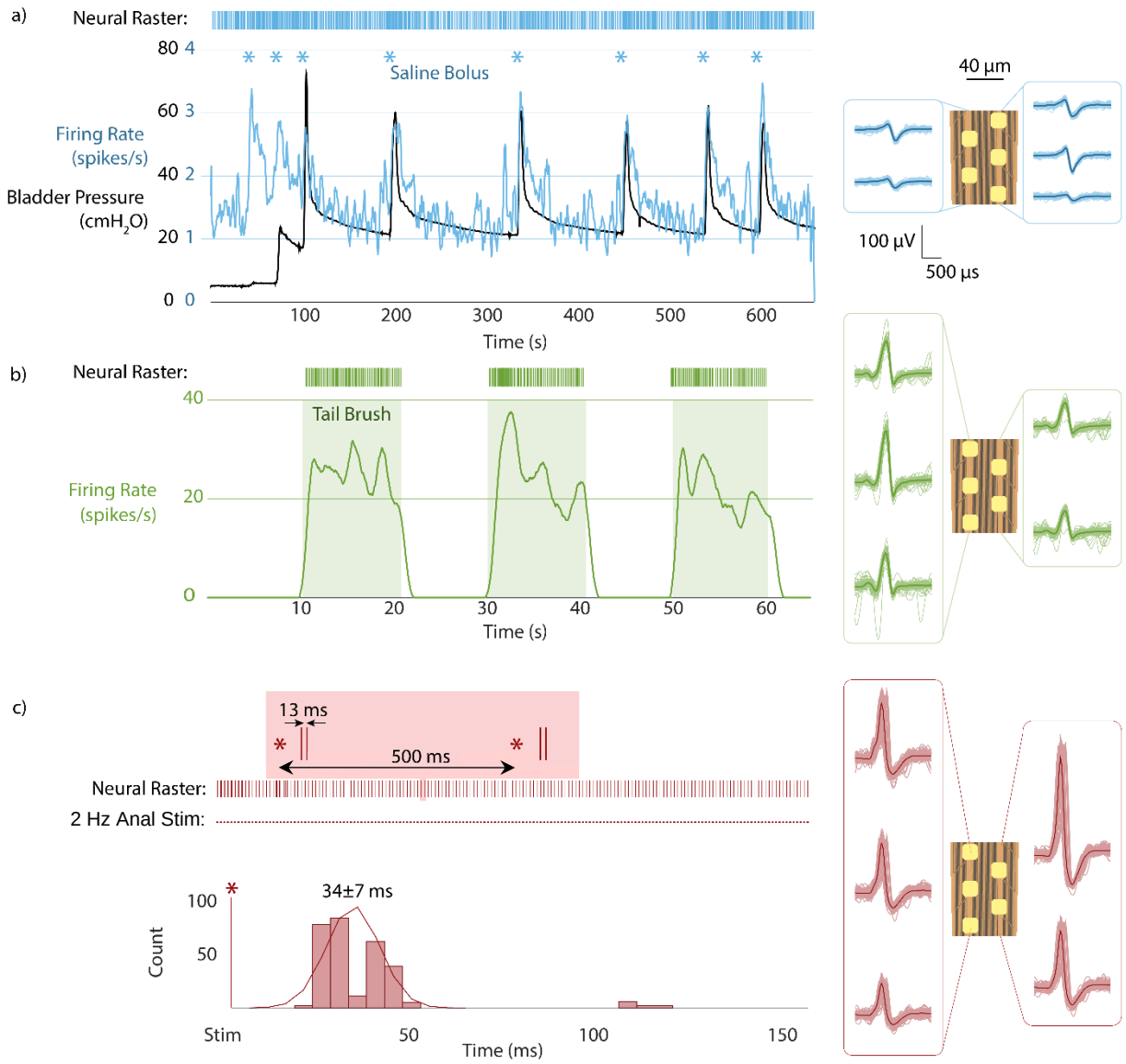

FIGURE 19: Sample of sensory units recorded from sacral DRG (a) Bladder-pressure correlated unit from saline bolus fills. Firing rate shown with recorded bladder pressure. Raster plot shows actual spike times. Waveforms shown at right in relation to channels. (b) Tail-brushing correlated unit (c) Anal sphincter electrical stimulus driven unit (2 Hz, 3.2 mA). Magnified raster plot shows characteristic double-spike with ~27 then ~41 ms stimulus delay. PSTH shown below neural raster.

FIGURE 19 (c) and (d), with associated PSTH showing a delay of 34 ± 7 ms from stimulation to recording. This unit showed a characteristic double spike response to stimulation (anal sphincter, 2 Hz, 3.2 mA), with the first peak around 27 ms and the second around 41ms. The early peak yields a CV of about 4.4 m/s, which suggests an Aδ-type fiber [87]. There are a

number of possible explanations for the second peak. The first peak is most likely a direct activation of the nerve ending by electrical stimulation, and the second likely originates as a result of an ensuing evoked muscle twitch. A variety of single and double-activated units were found in the data set. The longest delay for a directly activated unit was 203 ± 3 ms (CV: 0.44 ±

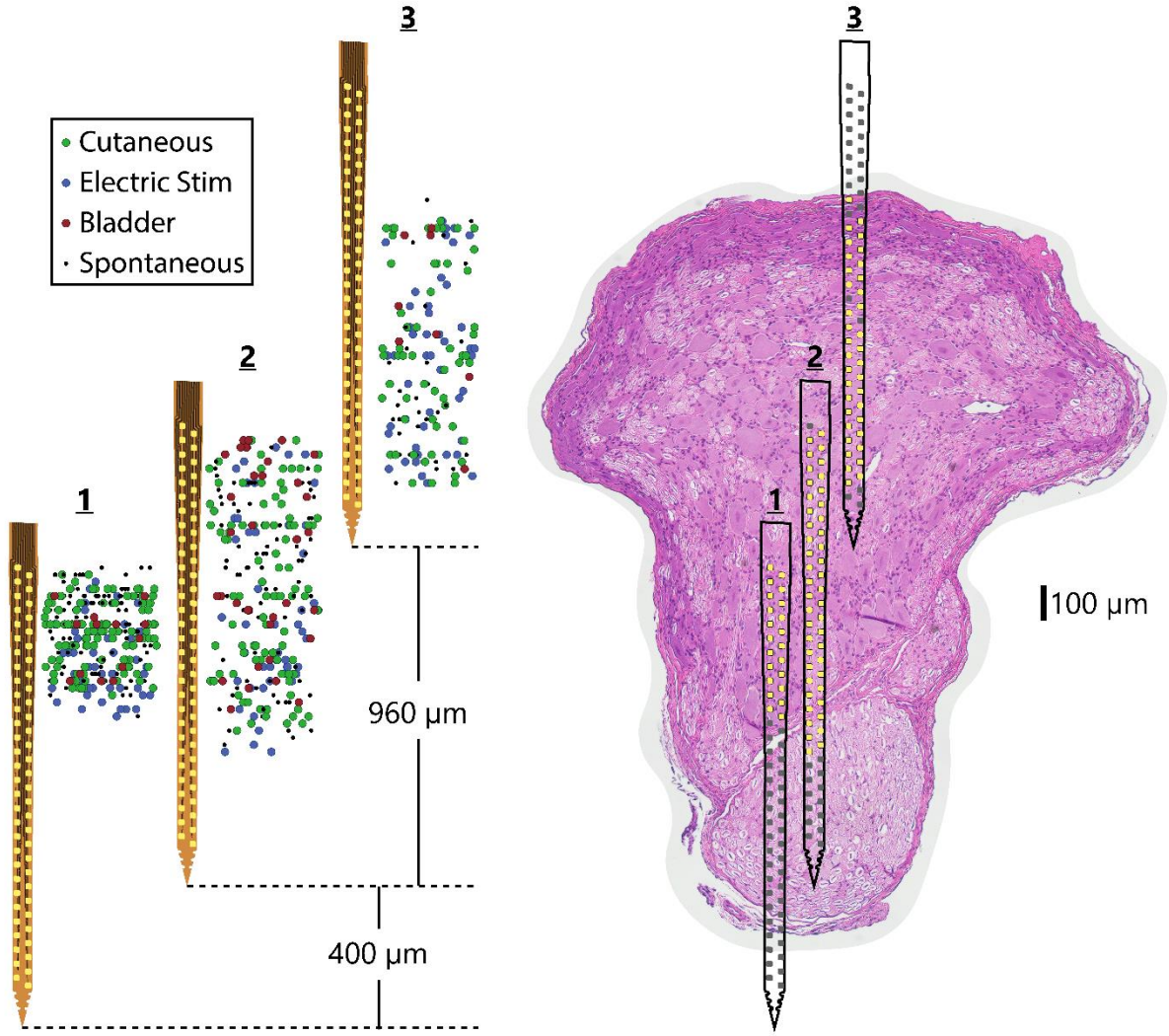

FIGURE 20: Summary of neural units recorded at different positions in DRG (left) Three different vertical positions of the array in one experiment showing the locations of recorded units (note: horizontal position is not relevant, points jittered for clarity). (right) Putative position of the array relative to histology of sacral DRG from same experiment. Lighter pink region at bottom is ventral root (VR), which does not contain sensory cell bodies for recording. Electrode sites with observed activity are highlighted in yellow, rest are gray. Horizontal position of array does not indicate horizontal movement.

.01 m/s, a pudendal activated C-fiber [87]). The shortest delay for a directly activated unit was 7 ± 0 ms (CV: 12.86 ± 0 m/s, a pudendal activated Aδ-fiber [87]). Other units had a less specific activation tied to stimulation. These units (amplitude on the order of 20-30 μV) were more likely to be active in the period 35-75 ms after a stimulus, but with delay standard deviations of up to 42 ms.

In experiment 3, neural activity was recorded with the array at 3 different positions in the DRG, with a full insertion (position 1) followed by retraction to other 2 positions in 80 μm steps (positions 2 and 3). FIGURE 20 (a) shows the modulated and spontaneous activity recorded at each position. Following the experiment, the DRG used was removed, fixed, sectioned axially, and stained with hematoxylin and eosin (H&E) to highlight cell locations. While the exact position of the array relative to the stained section is not known, by comparing the activated regions with the histology we can estimate the position of the array in the DRG and the ventral root (VR) below, from which we do not expect to record any sensory-evoked units. FIGURE 20 (b) shows the putative location of the array relative to the DRG cross section. In the same experiment, we recorded neural activity *during* retraction of the array between positions, while simultaneously brushing the right side of the scrotum. While noise was too high to discern neural activity during the retraction from position 1 to 2, neural activity was recorded from position 2 to 3. FIGURE 21 shows putative movement of 8 units throughout the retraction, including one with an amplitude artifact of breathing motion on the order of 10-20 μm. We observed that the movement of recorded units on the array (~600 μm) does not precisely align with the movement of the array itself calculated from the retraction steps (~960 μm). This is likely a result of slack in the flexible array ribbon.

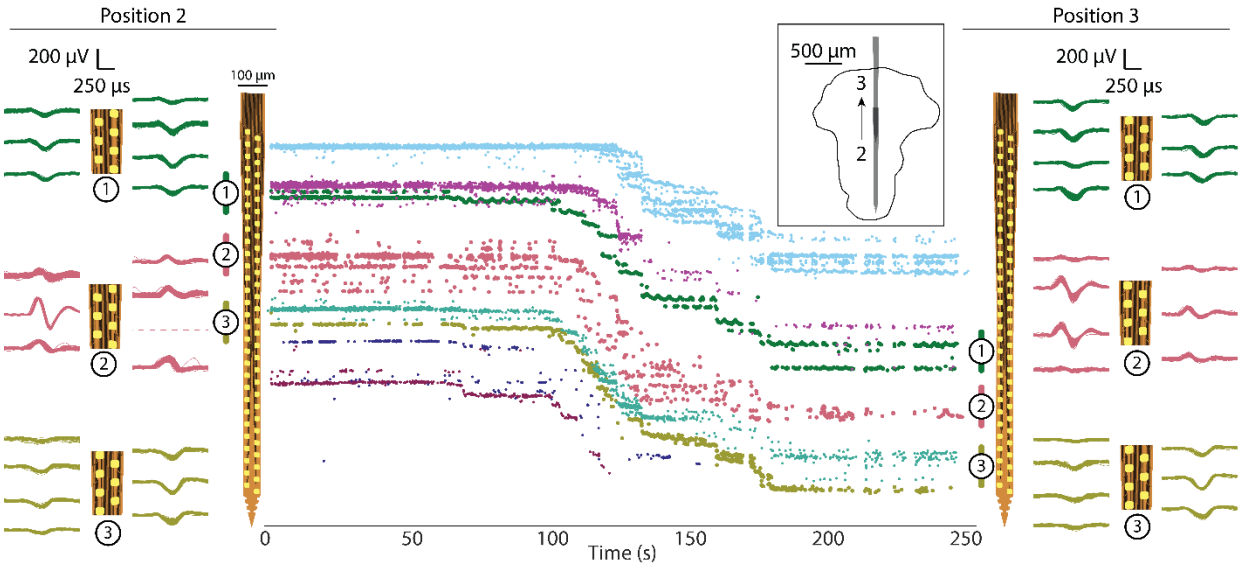

FIGURE 21: Units tracked across array during withdrawal from position 2 to position 3 (see FIGURE 20 and inset). As array is withdrawn from DRG, units move relative to the array (toward the tip). Eight units are shown, with movement of approximately 500-600 µm. Waveforms of several of these units are shown at position 2 (left) and position 3 (right) to show similarity of shape.

Discussion

In this study we demonstrated acute high-density recordings from feline sacral DRG. This study is the first to measure neural signals from inside DRG with flexible recording arrays and sets a new milestone for recording density in the peripheral nervous system. Using a specialized software for sorting high-density neural recordings, we showed that the array was capable of recording neural signals related to bladder pressure and cutaneous brushing in the sacral dermatome, as well as neurons which fire in response to electrical stimulation of the pudendal nerve or anal sphincter. We recorded neural units with peak amplitudes ranging from 20 µV to 1334 µV. This work shows the potential for high-fidelity interfaces with DRG.

A variety of other high-density or special-geometry microelectrodes have been developed for use in the brain [158]. Our work here is an extension of those studies to DRG, examining an over-sampling of local signals to obtain a greater resolution of underling neural

activity. With our high-density probe, we showed that recordings of single units could be achieved on multiple sites for a variety of afferents (FIGURE 19) and tracked using specialized software as the array moved over ~1 mm (FIGURE 21). Units which appeared only on a single channel here would have only a ~15% chance of being recorded with a 400 µm pitch Utah array. One recent technology for high-density recording in the brain is the Neuropixels probe, originally reported by Jun et al. (2017) [55]. This is a stiff silicon electrode array with 960 sites spaced at 20 µm. The array has been demonstrated for high-density single-unit recording in the brains of both head-fixed and chronic freely-behaving mice [55], [159]. While the challenges of implanting, fixing, and recording in DRG are very different from brain, the data processing goals and requirements can be very similar. In fact, the same software suite utilized in our study was also utilized in Jun et al. for faster-than-real-time processing on their very high channel count probes [55].

This study is the also first demonstration of high-density recording at this scale in DRG (40 µm site spacing), and one of very few in the peripheral neural system. Previously, the highest density recordings inside DRG used Utah arrays with site spacing of 400 µm [13], [14], [16], [150], except for a single study with 50 µm-spaced electrodes and no report of unit oversampling [20]. While the types of units recorded from sacral DRG in some of these studies were similar (cutaneous, bladder-related, pudendal-stimulation driven), there was no evidence of unit oversampling on neighboring sites. Higher density recordings have been made from the surface of DRG, down to 25 µm electrode site pitch, [40], [41], [111], [153], but despite the potential advantages of non-penetrating arrays these were fundamentally limited to recording single-unit activity from the shallowest ~150 µm of the DRG. Slightly higher-density recordings

have been reported in the peripheral nervous system. For example, 200 µm pitch Utah arrays have been used to record from the sciatic nerve of rats [160]. Transverse intrafascicular multichannel electrodes (TIME), which penetrate across the nerve axis and could hypothetically be used in DRG, have achieved peripheral nerve recordings with sites spaced at ~230 µm [52]. The recordings achieved in our study therefore set a new milestone for recording density in DRG and the peripheral nervous system.

This study, in conjunction with a report on the focused on the insertion shuttle technology [154], is the first demonstration of flexible bioelectronics delivered into DRG for neural interfacing. Even in an acute experiment, this approach has potential benefits over the standard Utah array, in potentially reducing bleeding or damage from impact of the pneumatic insertion required for Utah array implant [161]–[163]. In chronic experiments, the mechanical mismatch between stiff materials and soft tissue appears to result in tissue encapsulation of the shank tip, killing or pushing away neurons in the immediate 40-150 µm vicinity [48], [162], [164]. Our chosen delivery method, the stiff diamond shuttle with T-shaped profile, was selected based on the unique challenges of delivering a flexible electrode into DRG through the epineurium. In brain implants, flexible probes can utilize less stiff shuttles because the tough dura mater is typically removed in part prior to insertion for animal models larger than a mouse, exposing the significantly softer parenchyma below [165]. In DRG, however, the tough layer of epineurium cannot be easily removed without damage to the underlying neural tissue. Our UNCD shuttle, with its stiffened T-profile, addresses the need for high stiffness this while maintaining a minimal footprint that reduces damage to underlying tissue and blood vessels [154].

The primary analysis suite used in this study, Ironclust, is an open-source MATLAB package specifically designed to take advantage of neural unit oversampling to increase the speed and accuracy of spike sorting [58]. While no specific comparison between manual spike sorting was made in this study, a few general observations can be made from the authors' prior experience with commercial spike sorting software. By considering units identified on clusters of channels, the software saved the effort of separating the same unit on several channels, which was a large time saving. It also mostly eliminated the danger of yield overestimation. One major benefit for those comfortable with coding (the suite is available in a variety of code languages) was the ability to add features and analysis platforms as needed for a particular study. For example, because of this study's focus on unit drift, we added a platform to split units not only in principal component space but also based on spatial center. The open-source nature of the project meant that we were able to integrate useful features into the publicly available package.

This study, while a successful demonstration of high-density flexible penetrating arrays in DRG, also highlighted some important challenges for future studies, especially any that would proceed to chronic implant and recording. The deployment system was designed to temporarily adhere the array to the shuttle with a dissolvable PEG adhesive during insertion followed by removal of the intact shuttle immediately following array release. In practice, however, fluid in the surgical cavity could wet the adhesive and cause the array to peel away from the shuttle before insertion. While the system achieved successful delivery in experiment 1, all successful deliveries in following experiments were achieved with permanent cyanoacrylate adhesive to avoid inadvertent early wetting. A future design could use an array with a small loop at the tip

to go over the shuttle, which would drive in the array even if the adhesive started to dissolve. The stylet approach has a long history and recently demonstrated on a microscale in the so-called “neural sewing machine” [166].

Another issue with our approach was that, due to large breathing motions following insertion, we not able to successfully withdraw the shuttle without breakage prior to the use of cyanoacrylate. We attempted to address this by briefly suspending the breathing cycle during array deployment, but there was insufficient time for the array to fully release from the shuttle before breathing needed to resume. Since the lack of stiff materials in the DRG is one of the primary advantages of our flexible electrodes for chronic use, this issue would need to be solved prior to a long-term implant. One possibility would be to design the shuttle with a controlled breakage point to allow for removal with forceps after the array is securely in place. The natural breakage point of the current shuttle was flush with the DRG surface, making removal difficult. Alternatively, larger “barbs” fabricated as part of the array [167] could hold the array in place during shuttle withdrawal, allowing the shuttle to be removed more quickly.

Assuming these key issues can be addressed, a future chronic study with parallel implant of Utah arrays would be needed to demonstrate the comparative advantage of this technology in both recording longevity and biological response as determined through histological analyses. Continuous neural recording during awake behavior would demonstrate whether the unit tracking demonstrated in this study during array movement would be feasible long-term. This would be a useful feature in developing stable neural decoding for closed-loop neuroprosthesis research. A previous chronic feline study with Utah arrays demonstrated tracking of a bladder DRG neuron over the course of 23 days [13], and computational

algorithms can decode bladder pressure from neural firing of one or several units [81], [149], but the long-term stability of these algorithms depends on the ability to monitor multiple bladder neurons over a long period.

While only single arrays were implanted in this study, broader mapping of DRG afferents would require multiple arrays implanted in parallel. This could mean a single device with multiple shanks and/or multiple devices implanted next to each other. Further, this penetrating array could be used in conjunction with previously demonstrated surface arrays [111]. To simplify the implant process, it is possible to envision a combined penetrating-surface interface that would unfold onto the DRG surface during insertion. A similar approach has been previously demonstrated for chronic brain recording in a rat model [39]. This approach could provide an anchor for the surface array, a challenge discussed in our previous study [111].

Conclusion

This study was the first to demonstrate the use of flexible microelectrode arrays to record from within DRG, and to our knowledge the highest density electrode array reported for use in the DRG or peripheral nervous system. In this study, we recorded a variety cutaneous, bladder, and electrical-stimulus-driven neural signals from feline sacral DRG in acute anesthetized experiments. We used the high-density data along with specialized open-source software to detect individual neurons recorded on clusters of channels, and to track the "movement" of neural units as an array was slowly withdrawn from the DRG. In the future, we will use these arrays to monitor neurons long-term in awake behavioral studies as we continue to drive the development of neuroprosthetic systems for individuals with neural injury and disease.

Chapter 6
Discussion and Conclusion

This thesis has significantly advanced our understanding of DRG, in the critical areas of spatial mapping and tool development. I have demonstrated a novel technique for quantifying spatial density and applied it to both feline and human lumbar and sacral DRG. I have also demonstrated the benefits of novel flexible electrode arrays for recording neural signals at high density from both the DRG surface and interior.

In Chapters 2 and 3, I introduced a novel method to transform neural histological images to a normalized polar plane for statistical comparison. I used this technique to develop models of both feline and human DRG cell body density, with the highest density in the outer 20-25% radially and the dorsal 60-75% angularly. In the extended 3D analysis of human DRG, the highest cell densities were restricted to the inner 85% of the soma-containing region. Also in the human DRG, I further showed with models of axon density that the most myelinated axons are contained in the inner 90% radially, and that there is some evidence for lower density of small myelinated fibers at the dorsal aspect.

The results of these studies are supported by prior qualitative statements about dorsal, superficial clustering of neuronal cell bodies in DRG, including findings from both histology and electrophysiology [32], [73], [168]. Our DRG images appear qualitatively similar to prior

examples of cross-sections in the literature, such as in cats [32], [74] and rats [75], which show characteristic neuronal cell body clustering around the periphery. In the human samples, the quantity of fibers I observed was similar to previously reported values at both lower lumbar levels [28], [106].

A few caveats should be considered in interpreting the results of these studies. Formalin fixation was used to preserve all the tissue samples, sometimes for extended periods. Shrinkage of tissue is a common phenomenon in histology, and while it varies due to tissue volume and type, a study of optic nerve reported a mean 30% shrinkage artifact [169]. Since our main results are reported as proportions, however, this will likely have minimum impact. Other possible artifacts include tissue compression during removal and trimming, misalignment of the sectioning plane (not precisely parallel with nerve axis), and uneven staining over large sections. All images were visually screened for problems, but not all are visually apparent.

The polar transformation and averaging technique assumes that all samples are aligned alike, and while my automated alignment method is consistent, it is likely that the final samples were not all aligned perfectly to each other. The *in situ* orientation of the samples is also unknown, so while the assumption of the DRG as most dorsal is appropriate it may not be exactly correct. The polar transformation also requires distortion of the objects in the image, and while this is accounted for by normalizing to the underlying image warp, for very sparse observations some bias may remain in images that are far from circular.

Opportunities remain for future analyses of DRG cell density. While performance of the GUI and underlying algorithms was demonstrated to be satisfactory for trend analysis, improvements based on machine learning techniques could improve speed and accuracy.

Because NF200 will stain all neural tissue in animals larger than rats, higher resolution imaging of existing slides could allow for detection of the sub-2 μm objects not identified in this study [170]. Other neural stains could enrich the dataset, including Luxol fast blue for myelin [171] and TRPV1/peripherin to stain small nociceptors [110], all of which could provide evidence of sensory function and possibly functional somatotopy. Finally, while this study was limited to 10 donors, mostly older, male, and above normal BMI, a future study could expand this number or focus on other demographics to test for trends for which this study was underpowered. Morphometric changes in the DRG by age, body size, and sex have been identified in previous animal studies [68], [100], [101], [172], and more specific modelling in humans could lead to different therapeutic designs for different patients.

In Chapters 4 and 5, I implanted and recorded neural activity with two different versions of a high-density flexible polyimide microelectrode array, interfacing either with the surface or the interior of feline lumbosacral DRG. Both modalities were capable of recording single-unit activity driven by electrical stimulation, cutaneous brushing, and bladder filling. On closely-spaced channels single neuronal units were recorded on multiple channels. This oversampling was used with surface recordings to estimate the position of neural sources, and with interior recording to improve signal sorting and track neurons across a moving electrode array. Together, these studies represent the first time that high-density recording or use of thin-film arrays have been successfully reported for DRG.

Neural activity was observed in six of eight feline surface array experiments. The two experiments in which no DRG surface recordings were observed were all terminal experiments at the end of chronic implant periods for other objectives [8]. It is possible that a general

increase in scar tissue in the region contributed to a lack of results in those procedures. Neural activity was observed in all penetrating array experiments in which the array was successfully inserted in the DRG. However, in 2 of the 6 experiments the array never properly inserted, typically because the array adhesion was compromised by moisture. The primary issue with the use of flexible arrays to record from DRG in these studies was the general difficulty of successful and repeatable implant, because of the surgical environment, array properties, and shuttling technique. Slow blood pooling impeded visibility of the DRG, caused surface arrays to lift from the DRG surface, and wet the adhesive coating between shuttle and penetrating array. The thin surface arrays were difficult to manipulate and prone to be suctioned during blood removal. The diamond shuttles only allowed a single insertion of each penetrating array, which led to a limited number of recording sessions per experiment.

Future work utilizing these arrays in felines will include chronic implants, taking advantage of the 4 μm thickness to extend recording life by reducing immune and scarring responses. We will also perform experiments to validate the proposed source-localization, using higher stimulation amplitudes to lesion tissue for later histological analysis. These arrays (or similar) could be used with other peripheral and central nerve structures. Conceivably, the surface and penetrating approaches could be combined either in a single experiment, with more advanced surgical fixtures, or into a single integrated device that deploys a surface array as the penetrating component is inserted.

While this thesis was divided between histological analysis and electrophysiological experiments, the findings are connected by the overarching motivation of improving DRG interfaces. For instance, the quantitative description of high somata density in the outer dorsal

region of DRG is part of the motivation behind using surface arrays in the first place. All of the studies performed contribute to an overall understanding of the organization of cells in DRG, whether through numeric densities or through mapping of particular sensory modalities in individual experiments. Future studies could strengthen this connection by using the electrode tools described to test hypotheses suggested by the spatial maps. For example, a series of chronic animal studies with surface and penetrating arrays could determine with electrophysiology whether the outer 25% of the DRG contains more cell bodies available for neural recording than the inner 75%. Alternatively, the microelectrode arrays could be used to specifically target locations within the DRG suggested by the density maps. For example, a study of intraneural DRG stimulation for pain or bladder control could target the dorsal region I predicted to contain low density of small myelinated axons versus the rest of the DRG to test if stimulation was consistently more effective in either case.

The work described in this thesis has provided important new tools and knowledge for both recording from and mapping DRG. Along the vast frontier of the nervous system, there will always be new discoveries to make and obstacles to overcome. We are still in the early days of maximizing the potential of DRG neural interfaces, but the promise of improved clinical therapies will continue to drive the development of ever more advanced technologies and anatomical description. By continuing to explore, navigate, and chart this small but important corner of this great frontier, I hope to be a part of turning those promises into realities.

Appendices

Appendix A
Feasibility study of Utah array implant in ovine sacral DRG

Background

The purpose of this project was to establish the feasibility of dorsal root ganglion (DRG) microelectrode implant for neural recording and decoding of bladder state in a sheep model of bladder neuromodulation. Sheep have provided a useful conscious, large-animal model of bladder function for studying neuromodulation with Medtronic's Interstim® device [173]–[177]. Previous studies in the Bruns lab have used felines as models of sacral DRG interface for investigating bladder function using silicon-based electrodes [13], [149]. My goal was to translate the relevant surgical techniques from the feline to the sheep model.

In a study of human overactive bladder patients, continuous and conditional stimulation based on intravesical pressure measurements were equally effective, but conditional stimulation reduced overall stimulation time by 73% [178]. A variety of methods exist to estimate bladder state, though each has tradeoffs in terms of accuracy (potential chronic effectiveness, power consumption, ease of implant, etc.). In several review studies, it has been postulated that neural or muscular recordings may provide the best compromise for chronic feasibility, power consumption, artifact immunity, and signal size. Muscle signals are superior to whole nerve recordings in terms of signal-to-noise ratio (SNR), but single-unit recordings may

overcome this limitation. [179]–[181]. Access to the dorsal root ganglion in the sheep model would permit the ability to record single-unit action potentials from neural afferents, including a population related to bladder function.

In addition to providing a possible route for estimating bladder state, neural recordings of bladder afferents in the sacral DRG could improve our understanding of the mechanisms behind sacral neuromodulation. The ability of SNM to inhibit bladder contractions and increase capacity appears dependent on intact afferent nerves and not efferent, suggesting the mechanism is mediated via modulation of afferent activity [182]. A leading hypothesis is that, rather than inactivating efferents that directly innervate the bladder muscle, neuromodulation alters activity in neurons within the central nervous system and in spinal reflex pathways to change bladder behavior [183]. This is consistent with evidence from animal experiments which show the effects of neuromodulation persisting after the cessation of electrical afferent stimulation, sometimes for several hours [184]–[186]. Additionally, human patients show decreased activation of brain regions associated with micturition during stimulation [187]. Neural recording from the sacral DRG before, during and, after neuromodulatory stimulation may reveal how afferent activity changes during acute and chronic stimulation and aid in understanding the mechanism of SNM. No comparative study of this nature has yet been reported.

The focus of this study was to determine the feasibility of access to bladder nerve signals. The most commonly evaluated method to date has been electroneurogram (ENG) recording from cuffs on the pelvic nerve, which represent the sum of axonal activity within the nerve trunk [188]–[190]. The pelvic nerve conducts signals from mechanoreceptors in the

bladder muscle (detrusor). However, the SNR of ENG recordings is very low and dominated by skin dermatome signals. This study will attempt to overcome this limitation by implanting sacral DRG rather than the pelvic nerve, using an array of penetrating microelectrodes rather than a nerve cuff. DRG are proximal enlargements of the spinal nerves which contain the cell bodies for primary afferent neurons. DRG at different spinal levels contain sensory components specific to certain organs and skin regions. In humans, the corresponding pelvic nerve soma are located in sacral DRG levels S2-S4 (only S3-S4 in sheep) [191], [192]. DRG are advantageous sites for bladder neuron recording because these cell bodies produce larger electrical signals during action potential conduction, improving SNR relative to recordings from axons found in peripheral nerves [44]. Sacral DRG present a single site for interfacing, rather than a diffuse plexus. They also contain pudendal nerve afferents from the bladder neck and urethra which may provide additional useful signals for neuromodulation feedback (S1-S4 in humans, S3-S4 in sheep).

Previous studies have established that penetrating electrode arrays (such as silicon Utah-style arrays) can record single-unit neural activity from feline DRG, including acute and chronic monitoring of skin sensation, limb position, and bladder activity [9], [13]–[15], [41]. In a chronic study of bladder afferents in feline sacral DRG, bladder-related single-units were recorded for up to 41 days after electrode implant, with a maximum yield of 12/32 electrodes on one array recording bladder afferent activity. These units were identified based on high correlation of their firing rate with separately monitored bladder pressure, and previous studies have shown that a variety of mathematical models can use these firing rates to estimate bladder pressure [149]. Other non-bladder afferents may also be of interest in terms of their

inhibitory effect on bladder circuitry. No studies have yet reported recordings of neural activity from sheep DRG.

Unlike the InterStim sacral lead (model 3889), which is placed percutaneously, DRG microelectrode arrays are placed following surgical exposure of the DRG of interest. While the specific location of sacral DRG in sheep relative to the sacral foramina has not been reported, both felines and humans have either intraspinal (inside the sacral canal) or intraforaminal DRG at this level [193]. Lower sacral DRG, of main interest in this study, are almost exclusively intraspinal across animal models, and we assume the same will be true in sheep. Minimally invasive spinoscopic access to and visualization of intraspinal nerve roots has been demonstrated previously, suggesting it may be possible to access DRG for neural recording in the same way [194], [195]. Given available microelectrode designs and delivery systems, however, feasible access to intraspinal DRG presently requires removal of some of the sacral bone which protects the intraspinal space.

Several surgical routes have been described to access the sacral spine, including posterior and anterior approaches. The most straightforward approach is the posterior midline approach involving an incision directly over the lumbosacral vertebral processes. Relative to anterior approaches, this route poses the least risk to vasculature and the nerves of the sacral plexus, and by starting midline also minimizes risk to dorsal nerves [196]. Few muscle attachments in the region will also simplify the procedure and reduce potential blood loss, though it may prove impossible to avoid damage to the sacrospinous or sacrotuberous ligaments which obscure the dorsal sacral foramina. Procedures for the subsequent DRG exposure have been described in detail in humans (at the sacral level), pigs (at the lumbar

level), and cats (at multiple levels) [13], [197], [198] but not in sheep. These involve bone removal (laminectomy/laminotomy) with care taken to control bleeding from the bone and minimization the risk of nerve damage.

Note on following sections Because this project involved methodological development of a surgical protocol, the "Methods" section will present a detailed qualitative description of each practice procedure, including photographs and lessons carried from one procedure to the next. The "Results" section will present quantitative anatomical measurements described in "Methods," comparative photographs across procedures, and the final recommended surgical procedure.

All animal studies (cadaver dissections and acute surgeries) were carried out at the Medtronic Physiology Research Laboratory (PRL) using internally IACUC approved protocols.

Methods

Utah Array + Insertion Tool Models

Actual neural recording was out of the scope of this study, which sought only to establish the feasibility of microelectrode implant. Because no array functionality was necessary, we 3D printed a 4x8-layout 400 µm-pitch array based on specifications from Blackrock on a DWS 3D printer in Therma ceramic resin. This layout represents the minimum commercially available width (~1.9 mm). The length (~3.7 mm) is twice the minimum available but has been used successfully in feline sacral DRG recording. The array shanks (tapered shanks ~100 um thick) were too fine to print, but the final model accurately represented the footprint of a Utah array and showed dots where electrode shanks would be. For the final acute experiment, we glued an

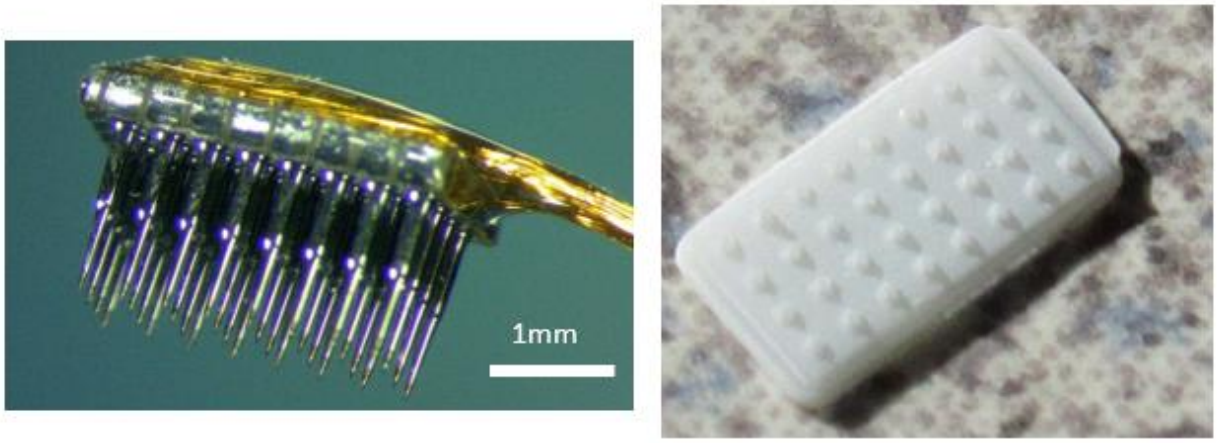

FIGURE 22: Utah array and model (left) 4x8 Blackrock microelectrode array. (right) 3D printed array model. Both at approximately equal scale.

insulated wire to the array model to simulate the actual assembly for implant. No additional sized arrays were necessary. FIGURE 22 shows an actual array (left) and our model (right) to scale.

A pneumatic insertion system from Blackrock is typically used to insert Utah arrays into DRG. To simulate this, we modeled and printed the handheld insertion wand in Vero White Plus on an Object 350/ Connex 3 printer. FIGURE 23 shows the actual inserter (top) and our model insertion wand (bottom).

Cadaver Studies

Female Polypay or Polypay-Mix sheep were euthanized with 90 mg/kg IV pentobarbital following studies for other purposes and then transferred to necropsy for use on this protocol. Sheep were perfusion-fixed with 10% neutral buffered formalin. The abdomen and pelvis caudal to the fifth lumbar spinal body was dissected from the remainder of the animal and immersion-fixed in 10% neutral buffered formal for at least 24 hours. Either an experienced parapathologist or a veterinary surgeon performed all dissections.

FIGURE 23: Insertion wand and model (top) Actual insertion wand, with pneumatic hoses on the left and actuating head on the right. (bottom) 3D printed model. Model length is 17.1 cm.

We performed a total of 4 cadaver dissections. Mean (± std. dev) age was 40 (± 10) months. Mean weight was 82.3 (± 9.9) kg. In all photographs with a ruler visible, the smallest increment shown is 1 mm.

Cadaver 1 (Age: 29 months; Weight: 71.3 kg)

The goal of the first dissection was to expose as much lumbosacral cord as possible, with maximal bone removal for visibility and identification of landmarks. We created an initial dorsal midline incision over the full length of the spine through the skin and fat layers, releasing fascia and cutting away muscle to expose the dorsal and transverse lumbar processes, the dorsal pelvis, and the sacrum. The dorsal lumbar processes (which project cranially) were separated from the sacral processes (which project dorsal-caudally) by a region of muscle. The parapathologist reported that in non-fixed specimens, this region could be palpated through the skin and is referred to as the lumbosacral depression. This depression was just slightly cranial to a line connecting the exposed posterior superior iliac crest (IC) of the pelvis. The lumbosacral depression was identified as a potential landmark for identifying sacral vertebral processes.

We removed additional tissue over the sacrum to expose the sacral processes. In this subject, we observed fusion of the S1-S3 vertebral bodies, but dorsal processes were not very prominent. The parapathologist reported that segment fusion and prominence of dorsal processes varies between subjects and should not be considered a consistent landmark for surgical planning. A small segment (~1 cm) of cauda equina was visible between the unfused S3

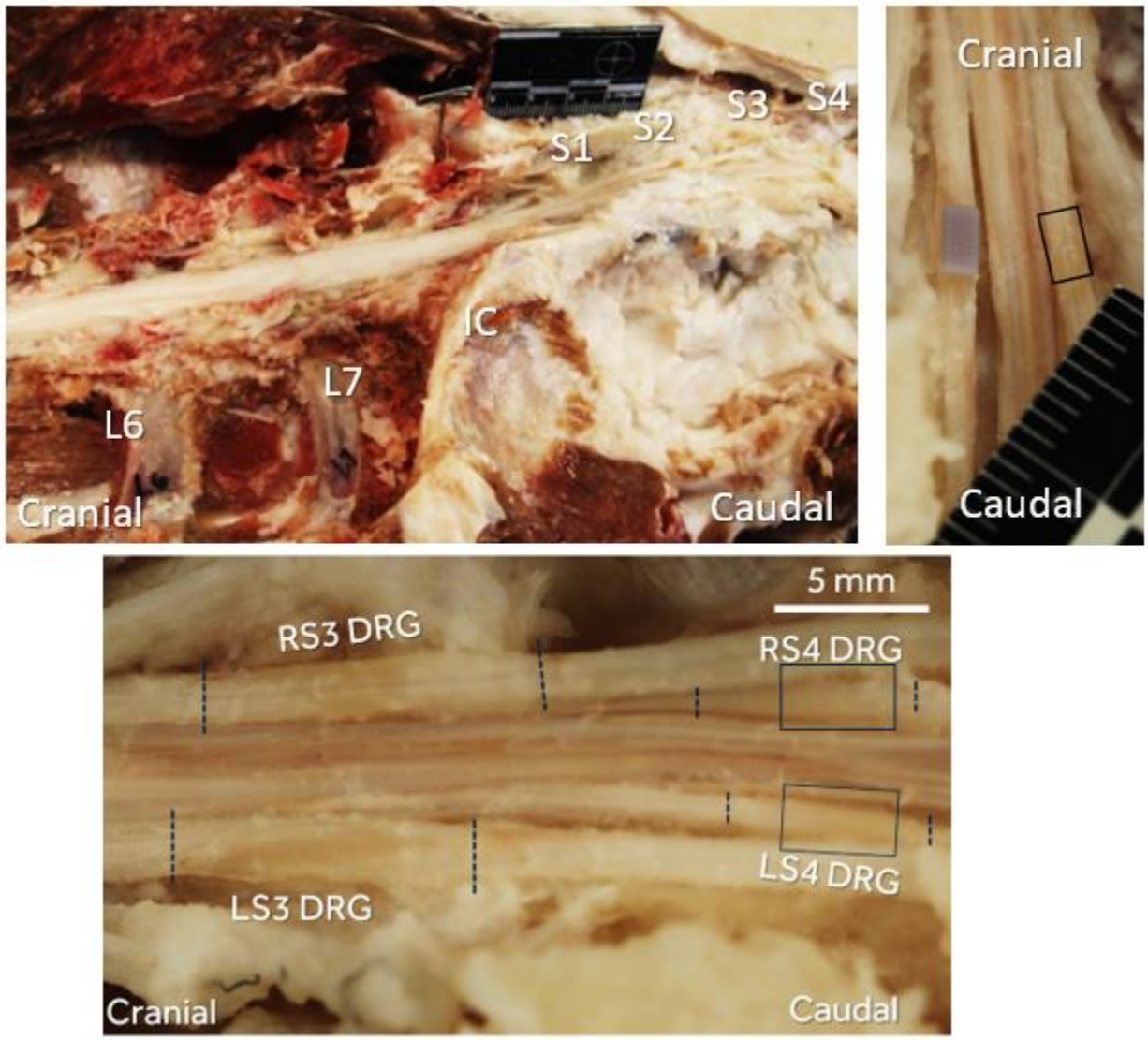

FIGURE 24: Exposure of sheep sacral DRG (top left) Full lumbosacral spinal exposure. L=lumbar, S=sacral, IC=iliac crest. Pin is in lumbosacral depression. (bottom) Exposed S3 and S4 DRG. Dashed lines indicate approximate extent of DRG bulge. Boxes over S4 DRG indicate approximate array footprint. (top right) Model array on left S3 DRG. Box over right S3 DRG indicates approximate array footprint.

and S4 processes, but no DRG were visible. As expected, DRG exposure would require removal of dorsal sacral bone over the spinal canal.

Using a vibrating saw, we cut into the left lateral aspect of the fused dorsal sacral processes, then pried the processes up with a T-bar handle surgical chisel (referred to by the parapathologist as a “T-tool”). We left the supraspinous ligament connecting the dorsal processes intact to maintain relative position. Below the processes was a layer of fat, which we wiped away with a cotton-tip applicator. At this point, with all dorsal sacral bone removed, the DRG became visible as elongated yellowish bulges in the sacral canal. The parapathologist reported that in fresh tissue the DRG appear slightly pink rather than yellowish. We exposed the full lumbosacral cord so all DRG were visible and identifiable by their relative cranial-caudal position in the sacrum (the cranial-most DRG in the sacrum is S1, with S2 and so on located more caudal). See FIGURE 24, top left (full view) and bottom (S3 and S4 DRG close-up).

From this dissection, we determined that the S3 DRG are located between the S2 and S3 dorsal processes and almost directly below the S3 dorsal process. While the exploratory method of process removal made exact distance measurement difficult, replacement of the processes suggested the S3 DRG were 7-10 mm cranial to the S3 foramen. Due to uncertainty, this measurement is not included in the results.

Finally, we placed the Utah array model on the surface of the S3 and S4 DRG, with the long side (length) parallel to the nerve. It appeared that all 32 electrodes of the array were within the footprint of the S3 DRG. On the S4 DRG it was possible to reduce overhang to only 1 or 2 electrodes, which would likely be acceptable in an actual recording experiment. It

appeared that the array was too wide for S4 DRG, rather than too long, and it was previously mentioned that the 4-electrode width is the minimum available.

Our conclusion from this dissection was that a surgical approach removing dorsal spinal processes between the S2 and S3 foramina would expose the S3 and S4 DRG. We also had evidence that the 4x8 Utah array was the appropriate size for neural interface. See FIGURE 24 right for array model on S3 DRG.

Cadaver 2 (Age: 53 months; Weight: 95.3 kg)

For this dissection, our goal was to determine whether a lateral surgical approach could be used to achieve DRG exposure on only one side to achieve less bone removal than a posterior midline approach, which requires removal of the dorsal processes. The veterinary surgeon who would perform the acute surgeries was present to practice and advise on the surgical approach. We used fluoroscopy to identify bony landmarks for surgery. Under fluoroscopic guidance, we identified each process and foramen, and we marked the locations on the skin by occluding the image with surgical tools. The foramina appeared as four pairs of

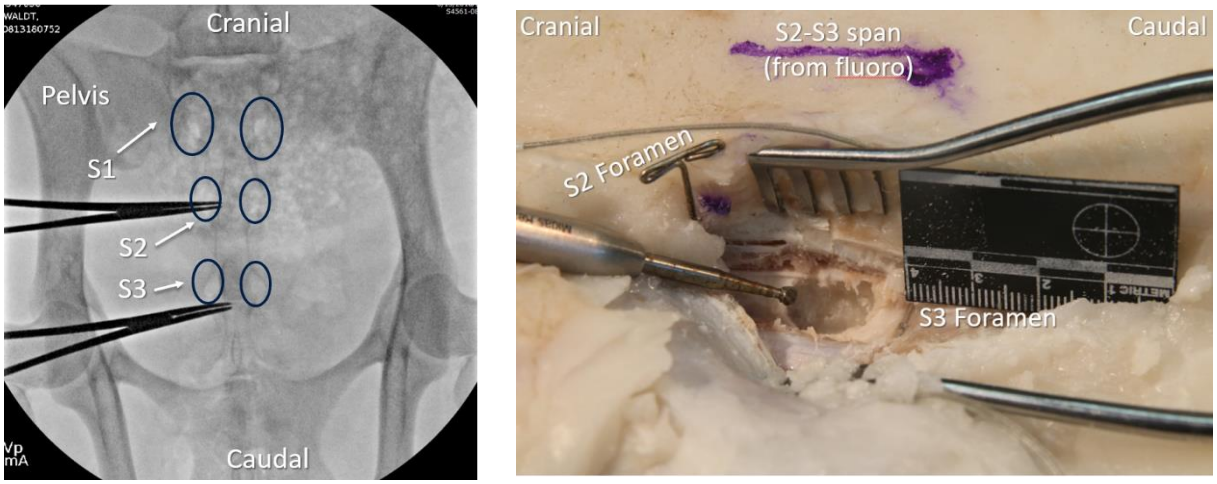

FIGURE 25: Fluoroscopic targeting of sheep sacral DRG (left) Sample fluoroscopy image of sheep pelvis and sacrum, showing labeled landmarks (actually from animal 347838). Bilateral S3 implanted foraminal lead visible at bottom. Hemostats are occluding image at ~S2 and S3 foraminal levels. (right) Hole drilled ventral to spinal canal.

light ovals in the sacral bone. The S2-S3 foraminal distance was about 35 mm cranial-caudally at the skin surface. See FIGURE 25.

Proceeding along this route from the right, we exposed the S2 and S3 foramina. This subject had previously been implanted with bilateral S3 leads, which helped confirm the foraminal identification. The surgeon used a Midas Rex Legend EHS high speed surgical drill with 3mm burr to remove bone, rinsing out fragments with saline and suction. The surgeon advised that a drill is used for speed until nerve is exposed, after which manual tools are used for improved precision and to avoid nerve damage. After removing bone to a depth of 6-7 cm, we determined that the surgical route was ventral to the spinal canal, and missed the cord and DRG entirely. We adjusted our trajectory toward the base of the dorsal processes and exposed the cord and several DRG. The actual bone removal necessary included the dorsal process and lamina within about a centimeter of midline. Based on this, we concluded that a posterior midline approach (that is, an incision starting directly over the dorsal spine) would be better than the lateral approach attempted in this procedure. See FIGURE 25 right. The pre-marked region in the cranial-caudal axis was well aligned with the ultimately exposed DRG, confirming that pre-operative fluoroscopy could be used for locating the nerve targets of interest.

Two pairs of DRG were visible within the exposed region (~1 cm cranial to the S3 foramen to ~2 cm cranial to the S4 foramen). A portion of the nerve structures on the left was accidentally removed during exposure, leaving only the right two DRG. This made positive identification of the remaining DRG difficult. Location and trajectory were insufficient to accurately identify specific DRG, although the more lateral DRG was likely to be S3. Measurements from these DRG are not included in the Results section. The uncertainty in DRG

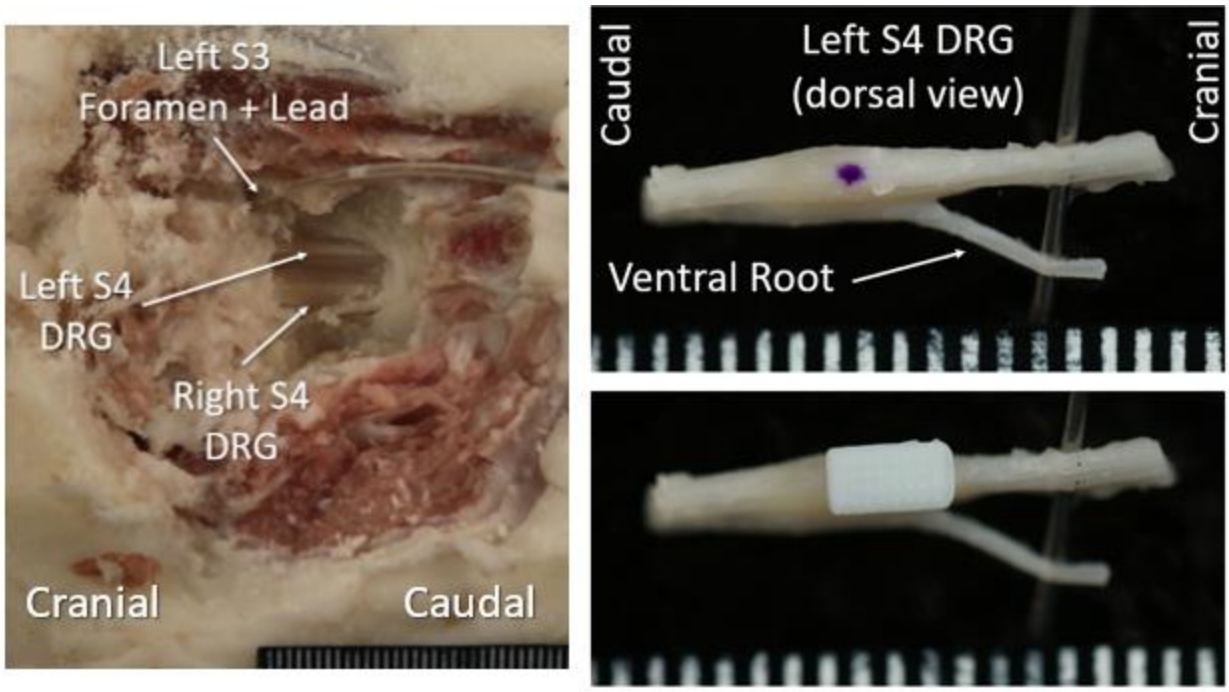

FIGURE 26: Exposed and resected sheep DRG (left) Exposed S4 DRG and lead (top right) Left S4 DRG, highlighting ventral root (bottom right) Same DRG with model array on top.

identity based on location and trajectory highlighted a need for using stimulation-based identification methods in the acute surgeries. The model Utah array seemed well-sized for both visible DRG, covering most of each without overhang.

Our conclusion from this dissection was that we should use a posterior midline rather than lateral surgical approach, using the fluoroscopically identified S2 and S3 foramina as surgical boundaries. We also had evidence that a non-anatomical method, such as electrical stimulation, would be needed to identify DRG *in vivo*.

Cadaver 3 (Age: 38 months*;* Weight: 80.7 kg

Our goal for this dissection was to expose the S3 DRG bilaterally with minimal bone removal via a posterior midline incision. The surgeon used fluoroscopy to identify the S2 and S3 foramina, then made the incision and removed skin and fat to expose the dorsal processes. He removed the caudal portion of the process bone with Ruskin rongeur forceps (see suggested

methods in Results) to the unfused joint between S3 and S4 vertebral bodies. He thinned the medial lamina just cranial to the S3 foramen using the drill with 3 mm burr, switching to a 2 mm burr when the bone began cracking. He increased the laminal opening laterally and about 12 mm cranial to the S3 foramen with the drill and rongeurs until a pair of DRG were exposed. This was achieved without disturbing the left S3 foramen, through which we were able to pass a Model 3889 quadripolar lead. This showed that placement of lead and DRG array unilaterally on the same nerve level was possible.

Based on the position of the first animal's S3 DRG (7-10 mm cranial to the S3 foramen), we initially believed the exposed DRG were S3. However, based on observations from the final cadaver and from the two acute surgeries, it is now apparent that these DRG were most likely S4. The photographs clearly show that the trajectory of these nerves was too medial to meet the S3 foramen (see FIGURE 26 left). Following *in situ* exposure, we resected the S4 DRG region for *ex vivo* photography and measurement. The left S4 DRG region was clearly split into a DRG and a ventral root, which allowed separate measurement for electrode depth planning (see FIGURE 26 right). The ventral root had a diameter of ~0.5 mm.

Our primary conclusion from this dissection, based on discussion of the variation among dissection specimens with the parapathologist, was the following set of anatomical criteria for DRG identification independent of animal size. The S3 DRG will be 1) the most lateral DRG in the spinal canal between the S2 and S3 foramina, 2) the most cranial DRG in the same space, and 3) part of the S3 nerves, identified by their trajectory toward the S3 foramina. The surgeon recommended that to avoid bleeding, bone removal should proceed from medial to lateral about 0.5 mm cranial to the S3 foramen, then caudal to cranial until 2 pairs of DRG are exposed.

Both S3 and S4 should be in the exposed region if this recommendation and the established anatomical criteria are followed.

Cadaver 4 (Age: 40 months; Weight: 81.9 kg)

The goal for the final cadaver was to confirm the findings of the previous 3 as final preparation for acute surgery, with bilateral exposure of S3 and S4 DRG. Because the fluoroscope was unavailable, we used a Faxitron device for X-ray landmark identification. This required shortening the specimen by removing tissue cranial to L5 and caudal to the sacrum. The center of the S2 and S3 foraminal region was marked on the skin with marker and a pin. We cut a posterior midline incision in the skin guided by the marked levels, then removed muscle and fat to expose the full dorsal sacral surface. We used a vibrating saw and T-tool to remove the dorsal process in this region. A layer of periosteal dura was visible beneath the removed bone, which was peeled back. We hadn't observed this layer in previous exposures, as it had likely been removed with the bone. We used a cotton-tipped applicator to wipe out fat, exposing nerves below. See FIGURE 27: Exposed S3 and S4 DRG with surrounding intact bone

Initially, only the S4 DRG and S3 nerves were visible in the sacral canal. Identification of the S3 nerves was possible based on their trajectory toward the pre-identified S3 foramen. In this specimen, the S4 DRG were about 4 mm cranial to the S3 foramen, and without sufficient exposure it would have been possible to mistake them for S3 DRG. Following the criteria established in cadaver 3; however, the S3 DRG were exposed during the additional lateral and cranial bone removal. The S3 DRG were located a full 21 mm cranial to the S3 foramina, and 15 mm caudal to the S2 foramina. We resected both the S3 and S4 DRG for measurement.

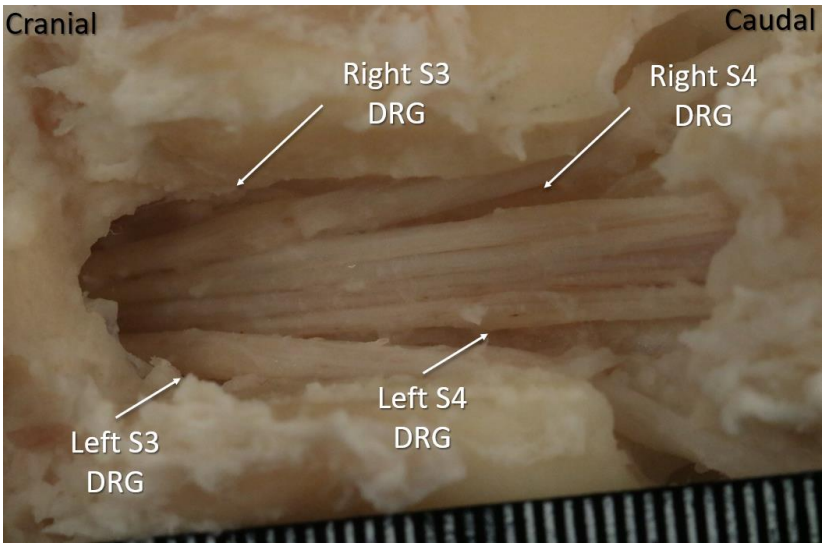

FIGURE 27: Exposed S3 and S4 DRG with surrounding intact bone

Our conclusion from this dissection was confidence that the general surgical plan we had developed could be used to access and identify the S3 and S4 DRG in the future planned acute surgeries. The S2 and S3 foramina were identified using pre-operative imaging as planned, and we exposed the S3 and S4 DRG by removing dorsal spinal bone in this region according to the anatomical criteria described in the conclusion of cadaver 3.

Acute Surgeries

Acute 1 (Age: 16 months; Weight: 64.5kg)

Our goal for this acute surgery was to access the S3 and S4 DRG bilaterally within the pre-operatively identified S2-S3 foraminal region, and to identify any challenges unique to anesthetized surgery. In particular, we wanted to evaluate and mitigate any gross nerve damage and bleeding. Anesthesia and monitoring were conducted per PRL #1 Standard anesthesia plan, which is described here in brief. The subject was induced to anesthesia with ~4 mg/kg propofol and 0.01 mg/kg buprenorphine for intubation, then maintained using 1-3% gaseous isoflurane and a 0.4 mcg/mL fentanyl/0.3 mg/mL ketamine solution in 0.9% saline. A

stomach tube was used to alleviate gas buildup. Vitals were continuously monitored including heart rate (ECG), SPO_2 (tongue), temperature (esophageal), and arterial pressure.

The surgeon used fluoroscopy to identify the S2 and S3 foraminal levels and mark them on the subject's skin, which was shaved prior to surgery. To minimize bleeding, he used cautery to open the posterior midline incision through the skin and subdermal fat, then to separate muscle from the lateral aspects of the dorsal processes. He proceeded with a periosteal elevator to scrape and reflect muscle away from the bone, using retractors cranial and caudal to keep the incision open.

With the sacral bone exposed, the surgeon marked the S3 foramen with a surgical marking pen to avoid damage for eventual lead placement. He used Ruskin rongeurs to remove dorsal process bone, then used the high-speed drill and saline irrigation to remove the dorsal lamina bone below. Some muscle and bone bleeding were observed and were managed by cauterizing. Following initial bone removal, a fat layer was visible in the spinal canal. In order to avoid nerve damage, the surgeon continued widening the spinal opening with Kerrison rongeurs. He used a combination of suction and a hemostat to remove fat until the nerve structures were visible below.

To minimize bone removal, the surgeon at first only worked in the caudal region of the S2-S3 foraminal surgical boundary. In this initial exposure, a pair of DRG were visible that were preliminarily identified as S3. Based on our established criteria, however, the spinal opening was increased laterally to expose an additional nerve more likely to be S3. With more cranial bone removal, the DRG for this nerve were identified. The full exposure of S3 DRG, as predicted, had included exposure of the S4 DRG as well.

To confirm the identity of the nerves, we stimulated each exposed DRG using the Medtronic Nerve Interoperative Monitoring (NIM) system (1 Hz, 100μs pulse width, 0.2-0.5 mA; needle ground placed in left thigh). Stimulation of the putative S3 DRG produced visible contraction of the external anal sphincter (0.2 mA threshold on the right, 0.5 mA on the left). Stimulation of the left putative S4 DRG produced a visible tail twitch at 0.5 mA, while stimulation of the right S4 DRG produced no visible effect. An anal contraction (or "bellows") response with S3 stimulation and a tail twitch with S4 stimulation is consistent with the surgeon's prior experience using stimulating leads, supporting the identification of the corresponding DRG.

The surgeon attempted to use fluoroscopy to introduce a stimulating lead into the left S3 foramen, but the foramen had been accidentally damaged during the procedure. Based on this, in the next surgery the lead will be placed prior to any bone removal and used as a guide to ensure foraminal integrity.

The model array was placed on S3 and S4. It was adequately sized for either DRG, but the bone removal was inadequate to place the array fully on the dorsal side of S3. During additional cranial and lateral bone removal, a large blood vessel was nicked (possibly the S2 intraforaminal vessel). Due to limited visibility in the surgical site and the apparent proximity of the foramen to the S3 DRG, this outcome may be difficult to avoid. However, DRG this close to the foramen were not observed in the previous dissections, so we do not anticipate this issue in every procedure. Significant bleeding in future procedures could be managed with Gelfoam hemostatic material and/or pressure to the bleeding site.

Since surgical goals had been achieved at this point, the animal was terminated with 90 mg/mL IV pentobarbital. Following euthanasia, blood in the surgical site and additional bone was removed to fully expose the S3 DRG. The model pneumatic inserter wand was photographed with the S3 DRG to show that it would be usable in an actual insertion.

Our conclusion from this surgery was that the anatomical approach and DRG location criteria developed in the cadavers was appropriate for surgical access. We also confirmed DRG identity with surface stimulation. In the next surgery, the lead will be implanted prior to laminectomy to avoid foraminal damage and Gelfoam hemostatic material will be used to slow/stop any foraminal vessel bleeding.

For both surgeries, relevant photos are in the Results section referenced to the appropriate surgical step.

Acute 2 (Age: 101 months; Weight: 84.9kg)

With the success of the first acute surgery in exposing and identifying the S3 and S4 DRG bilaterally, the goal for the second was a unilateral exposure of both DRG levels as a less invasive option when bilateral exposure would be unnecessary for study goals. For a unilateral exposure, we discussed the possibility of sparing the dorsal processes. The surgeon's opinion, however, was that this would not allow enough space or visibility for safely maneuvering instruments. He also noted that the DRG were quite midline and unlikely to be exposed if the dorsal processes were not removed. Based on the surgeon's recommendation, we planned to remove the dorsal processes as in the first procedure. We also planned to implant a Model 3889 quadripolar lead in the S3 foramen ipsilateral to the S3 DRG exposure. Considering the

accidental foraminal damage in previous procedures, the surgeon recommended placing the lead prior to bone removal.

Anesthesia for this surgery was the same as for the first. The surgeon again used fluoroscopy to identify the S2 and S3 foramina, then created a posterior midline incision via cautery. A Model 3889 lead was introduced into the left S3 foramen, leaving the introducer sheath in place so as not to deploy the tines. A bioengineer used an external neurostimulator (10 Hz, 210 ms pulse width) to stimulate the lead electrodes. In the $3^-/0^+$, $3^+/0^-$, and $2^-/0^+$ configurations, 1 V stimulation was sufficient to produce the desired bellows response indicating good lead placement. The stimulator dial does not provide resolution below 1 V, so this was considered the motor threshold for all configurations.

Leaving the lead and sheath in place, the surgeon removed the dorsal process and started lamina removal with the high-speed drill on the left side of the spine in the more cranial interforaminal region. During the lamina removal, a bone-perforating blood vessel was cut (smaller than the intraforaminal vessel nicked in the first acute surgery). These vessels are not visible before they are nicked during bone removal. The surgeon used the drill burr in reverse to attempt friction cautery, but ultimately just waited for about 5 minutes for the vessel to clot. On the recommendation of the second surgeon, 40 µg/mL phenylephrine was prepared for IV saline drip to help control bleeding, heart rate, and blood pressure. Some slow bleeding from the bone continued throughout the procedure.

The surgeon exposed the S3 DRG on the left side of the cord while leaving the right-side bone intact. We confirmed the identity of this DRG using the NIM system (threshold for anal wink: ~0.2 mA at 4 Hz, 100 µs pulse width). Stimulating the nerve rather than the DRG resulted

in a leg twitch, though it is possible that stimulation was spreading to the S2 spinal nerve, which contains sciatic innervation for the leg. We also stimulated the S4 nerve (not DRG), producing an anal twitch. Surprisingly, we exposed the S3 DRG without first exposing the S4 DRG. We believe that this was the result of avoiding the S3 foraminal region, which required a more cranial exposure as compared to previous experiments. Since S3 lead stimulation had caused successful motor response and we wanted to evaluate lead location integrity throughout implant, we decided that S3 DRG exposure was sufficient for this surgery without S4 DRG exposure. It is likely that S3 lead placement and S4 DRG implant are mutually exclusive, because bone removal to expose S4 has always led to S3 foraminal damage, but this may be re-evaluated in the future if necessary.

A model array with attached wire was placed over the left S3 DRG. The surgeon elevated the entire nerve with a metallic surgical hook (glass would be preferred for a recording experiment to avoid accidental capacitive discharge) and applied a U-clip anastomotic device around the distal nerve root and the array wire. This kept the model array in place over the DRG. However, for actual implant, the array electrode shanks would most likely have to be inserted without elevating the nerve root. Any disturbance of the root could lead to broken shanks. This test was useful, however, in case the U-clip could be applied prior to array insertion.

As a more representative securement method, the surgeon used 6-0 Prolene suture to secure the array wire to nearby muscle at several points ascending from the surgical cavity. He sprinkled Gelfoam into the cavity to simulate an array covering but noted that for a survival

surgery Gelfoam would not provide adequate structure. He would prefer to use Tisseel fibrin sealant spray.

Test stimulation on the lead yielded a bellows response at the same threshold as initial placement, both before incision closure and following closure with tine deployment. This showed first that the surgery had not greatly disturbed the lead implant location, supporting our ability to implant both the array and the lead at the S3 DRG and S3 foramen unilaterally. It also suggested that there was not a large degree of nerve damage due to nerve exposure. At this point, the surgery ended.

Our conclusion from this procedure was that a unilateral exposure and microelectrode implant of S3 DRG with S3 foraminal lead implant was feasible for a future chronic experiment. The previously developed anatomical approach combined with DRG surface stimulation, allowed exposure and identification of the S3 DRG. The S4 DRG was not exposed in order to leave the S3 foraminal lead in place, suggesting that this combination would be difficult to achieve. While bleeding was encountered, it was managed by waiting for clotting to occur.

Results

Table 1 reports quantitative anatomical measurements made during this study (to the nearest 0.1 millimeter). Measurements were made after the fact from photographic record. Some measurements were not possible in every procedure depending on time and procedure goals, so *n* is reported for each measurement and should be interpreted as the number of unique measurements made (rather than the number of animals).

TABLE 5: Anatomical measurements of DRG and positions

Measurement	Description	Mean ± Std. Dev [n] (mm)
S3 DRG diameter	Width of S3 DRG at widest point, perpendicular to nerve path	2.3 ± 0.1 [4]
S3 DRG length	Length of S3 DRG bulge from proximal to distal taper parallel to nerve path	10.5 ± 1.7 [4]
S4 DRG diameter	Width of S4 DRG at widest point, perpendicular to nerve path	1.5 ± 0.2 [8]
S4 DRG length	Length of S4 DRG bulge from proximal to distal taper parallel to nerve path	7.6 ± 0.8 [6]
S2 foramen-S3 DRG	Distance from S2 foramen to center of S3 DRG, parallel to spine	14.1 [1]
S4 DRG-S3 foramen	Distance from center of S4 DRG to S3 foramen, parallel to spine	6.4 ± 0.8 [2]
S2 foramen-S3 foramen	Distance from S2-S3 foramen, parallel to spine	31.7 ± 2.2 [4]
Inter-S3 DRG	Distance from left to right S3 DRG center, perpendicular to spine	6.6 ± 0.4 [4]
Inter-S4 DRG	Distance from left to right S4 DRG center, perpendicular to spine	4.7 ± 0.5 [4]

Surgical Plan

This section proposes methods for surgical access, device implant, and closure unique to this procedure. While as much detail is provided as possible, the phrase “per usual protocol” is used when parts of the procedure are typical to other PRL activities and not the focus of this study. In these cases, the investigator should refer to the appropriate PRL protocol for guidance.

This procedure is anticipated to require about 3 hours of OR time, not including setup, initial anesthetic knockdown, or any desired intraoperative data collection outside of what is necessary to positively identify nerve targets. Variables that may affect this estimate include

surgeon familiarity and practice, inter-subject anatomical variation, ease of InterStim® lead placement, and management of bleeding.

This procedure was developed in female Polypay sheep (65.5-95.3 kg, 16-101 months). Use of males or significant size/age variation may impact the surgical approach due to anatomical differences. Prior to surgery, the desired locations of recording arrays and leads should be established. Any spinal level configuration of lead(s) contralateral to array(s) should be possible. Not all configurations of lead(s) ipsilateral to array(s) may be feasible, since laminotomy may disrupt the foramina which help anchor stimulating leads. Table 2 suggests feasible and unfeasible ipsilateral configurations for S3 and S4, though anatomical variations may impact outcomes. As summarized, any combination of S3 lead with S4 DRG array has a low probability of success.

TABLE 6: Recommendations on possible lead/array implant combinations for S3 and S4 spinal levels

Recommended		**Not Recommended**	
Lead Foraminal Location(s)	Array Ganglia Location(s)	Lead Foraminal Location(s)	Array Ganglia Location(s)
S3	S3	S3	S4
S4	S3	S3	S3 & S4
S4	S4	S3 & S4	S4
S4	S3 & S4	S3 & S4	S3 & S4
S3 & S4	S3		

Steps

1. Prepare the subject for chronic anesthetized surgery per usual protocol. Induce subject to anesthesia with propofol for intubation per usual protocol. Maintain subject under isoflurane anesthesia with ketamine analgesia, stomach tube, and vital sign monitoring per usual protocol.

2. Conduct pre-operative CT or MRI imaging as desired for experimental goals.
3. Closely shave the subject's lower back and pelvic region, at least the entire area caudal to the palpable lumbosacral depression. Additionally, shave a portion of outer thigh to allow for placement of the NIM system needle reference electrode.
4. Position subject prone (dorsal side up) on the surgical table.
5. Use fluoroscopy to visualize the dorsal sacrum in the frontal plane. The sacral foramina should appear as 4 symmetrical pairs of dark ovals. Use surgical tools on the skin surface to occlude the fluoroscopic image at the levels of the S2 and S3 foramina, marking these levels on the skin as references. See FIGURE 29.
6. Use cautery to open a midline incision between the S2 and S3 reference lines. Cut down to level of supraspinous ligament which connects the spinal dorsal processes.
7. Place InterStim® lead(s) at desired foramina per usual protocol (including fluoroscopy and test stimulation). The only deviations from usual are
    a. Place the lead(s) inside of the midline incision, rather than percutaneously.
    b. Once in desired position, do not fully deploy the lead(s). Instead, leave lead(s) in the introducer(s). Use a temporary loop of suture around the introducer(s) and through the animal skin to retract them caudally. This will decrease the likelihood of disrupting lead location during subsequent steps.
8. Use retractors to increase visibility inside the incision.
9. Create shallow cautery incisions on either side of palpable dorsal processes (as close to midline as possible) to start releasing muscle. See FIGURE 28 (note no lead implanted).

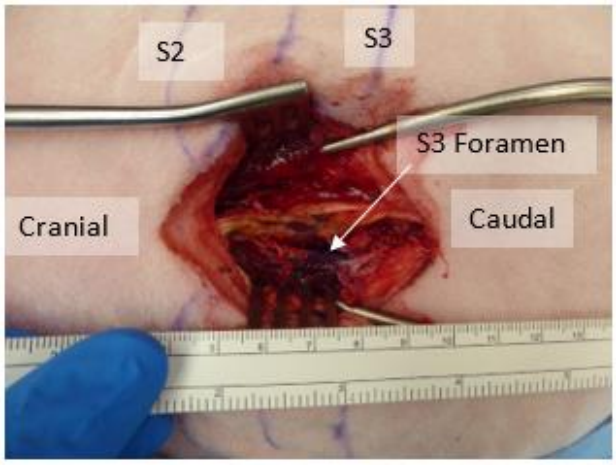

FIGURE 28: Dorsal process exposed. Dark purple is marked S3 foramen. Ruler in cm and inches.

10. Use periosteal elevators to reflect muscle from dorsal processes throughout the length of the incision. Expose the full depth of the processes and as much of the dorsal sacral surface as possible.
11. Use Ruskin rongeur forceps to remove dorsal process throughout the length of the incision. See FIGURE 30 (removed process) and FIGURE 31 left (tool).

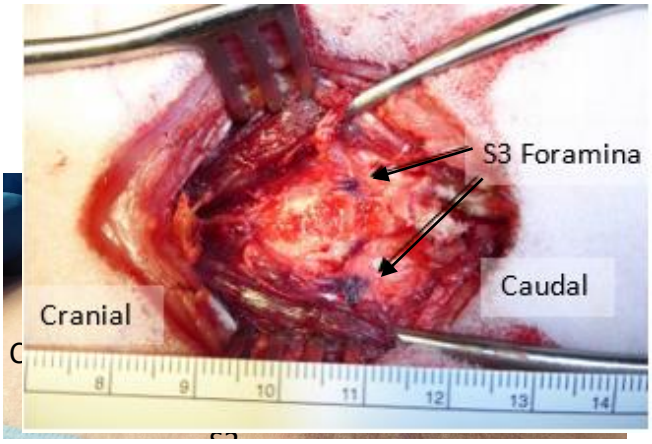

FIGURE 30: Dorsal process removed. S3 foramina marked.

FIGURE 29: S2 and S3 foraminal levels marked

12. Use a high-speed surgical drill with 3-4 mm round carbide or diamond burr to remove the lamina covering the sacral spinal canal. The first tissue exposed beneath the bone will be yellowish-white fat, which can be safely removed with careful suction and

forceps dissection. Once enough fat and bone are removed, the sacral cord/cauda will be visible as a grayish-white column with visible blood vessels.

13. Once the sacral cord/cauda is visible, proceed with lateral bone removal using a combination of drilling and clipping with 2-3 mm Kerrison rongeur forceps (see FIGURE 31: Recommended spinal bone removal tools(left) Example of Ruskin rongeurs with inset of cutting surface (right) Kerrison rongeurs (both from austos.com) right). For any exposure, surgeon should work from the midline outward, as this will maximize visibility of nerve structures while minimizing the risk of bleeding. Spinal nerves can be gently retracted with glass nerve hooks to improve visibility. Surgical magnifying loupes are recommended. While minimizing bone removal is desirable for recovery and control of bleeding, exposure should focus on optimizing visibility of the target DRG. The impact surface of the pneumatic insertion wand will dictate how much nerve must be exposed for proper array placement. DRG will present as ovoid bulges along the spinal nerve. Specific guidance is provided below depending on the type of array placement desired:
    a. For unilateral placements, it is possible to remove bone only on one side.
    b. For S3 DRG array placement, focus on bone removal closer to the S2 foramen, taking care not to nick the transforaminal blood vessels. The S3 DRG will likely be in a more lateral position within the canal relative to the S4 nerve.
    c. For S4 DRG array placement, focus on bone removal closer to the S3 foramen. The S4 DRG will likely be in a very medial position, tucked right next to the central cord.

14. Some bleeding is expected from blood vessels in the spinal bone. Cotton applicators or absorption spears/triangles can help soak up blood to improve nerve visibility. Electrical cautery for bleeding control should be avoided near nerves. The following methods may be used to safely control bleeding:

    a. Direct pressure with small cotton applicator for several minutes.

FIGURE 31: Recommended spinal bone removal tools(left) Example of Ruskin rongeurs with inset of cutting surface (right) Kerrison rongeurs (both from austos.com)

    b. Packing surgical site with gauze and waiting for bleeding to abate.

    c. Running the surgical drill with round carbide burr in reverse (frictional cautery).

    d. Pressing bone wax into bleeding site.

15. Once the target DRG is visible, confirm its identity using the NIM system. Use the bipolar stimulator wand for surface stimulation (0-1 mA, 1-10 Hz, 100 µs cathode leading biphasic waveform). Stimulation of the S3 DRG should lead to ipsilateral bellows (anal sphincter or levator ani contractions). Stimulation of the S4 DRG should lead to ipsilateral tail pulling. Note that off-DRG stimulation may lead to other effects. See FIGURE 32 for identified DRG in unilateral and bilateral exposure.

16. Place the 4x8 (preferred) or 4x4 Utah array with shank length 1.5 mm (preferred for S3) or 1 mm (preferred for S4) over the target DRG, shank-side down and long edge parallel to the nerve root (being careful not to touch the delicate electrodes with bone or

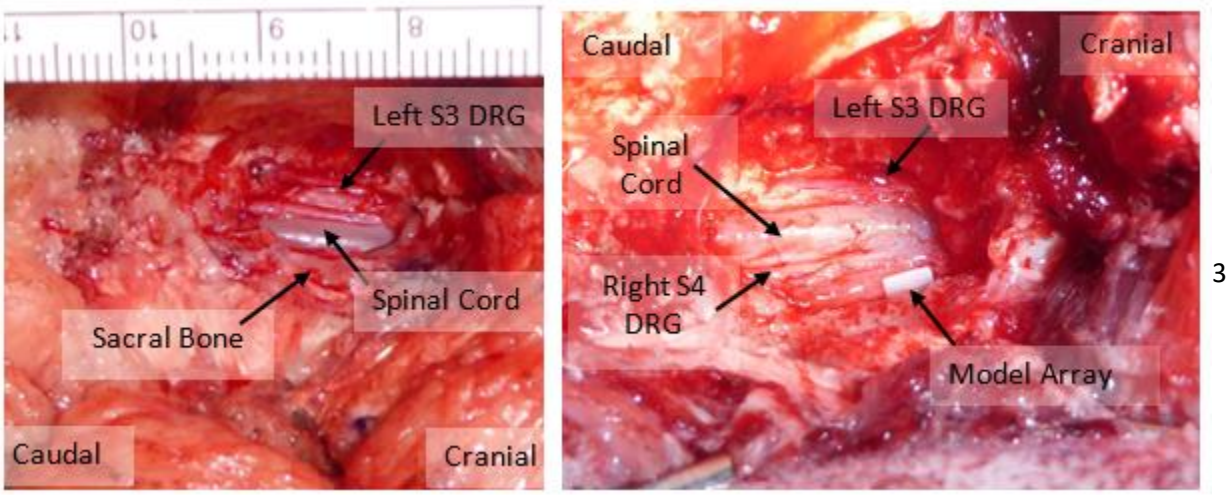

3

FIGURE 32: Surgical exposure of sheep sacral DRG (left) Unilateral left S3 DRG exposure (right) Bilateral S3 and S4 exposure with model array. Scale: array length=3.7 mm

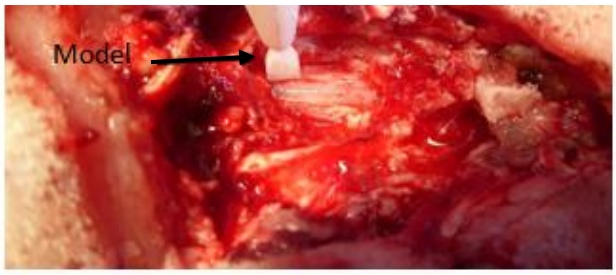

FIGURE 33: Bilateral S3 and S4 exposure with model insertion wand over left S4

20. Carefully remove surgical tools and evaluate array insertion. With proper placement, bond-side of the array will be parallel with the nerve surface, no shanks should be visible, and the array will remain in place even with light vertical tugging on the gold recording wire. If necessary, repeat insertion.

21. Evaluate array impedance (functional sites should have impedance <100 kΩ). If desired, connect array to neural recording system and look for unit responses to dermatome brushing in anal and genital region. If necessary, repeat insertion.
22. While keeping the array connector stabilized, suture loops around the gold recording wire to secure it to nearby tissue (usually muscle, but dural suture or tying through drilled bone eyelets is also acceptable).
23. Use DuraSeal®, Tisseal®, and/or sterilized plastic wrap over the array site to protect it from tissue ingrowth and promote healing.
24. Re-test lead function and remove introducer sheath to deploy.
25. Route array and lead wires out of incision site, and suture fat and muscle layers closed.
26. Install ground wires and chronic housing and suture skin incision closed.
27. Conduct post-operative imaging as desired and allow animal to recover under observation.

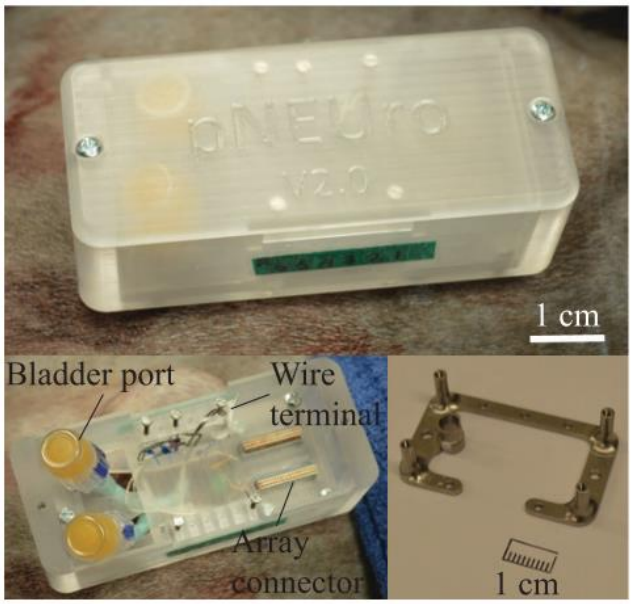

FIGURE 34: Panel from Khurram et al. 2017 showing chronic instrument housing. (top) Backpack closed and implanted in a feline. (bottom left) Backpack open to show electrode-headstage interface. (bottom right) Metal baseplate to be implanted subdermally for housing anchoring.

The goal of this study was to develop a surgical protocol for access to the S3 and S4 DRG and to assess the feasibility of microelectrode array implant. We developed a method for DRG access and identification in four female Polypay cadaver specimens, then tested and refined that method in two acute surgeries. These procedures demonstrated that it is possible to consistently locate the DRG of interest in the sacral canal between the S2 and S3 foraminal levels. We also showed that these DRG may be appropriately targeted with a commercially available 4x8 penetrating microelectrode array with 1-1.5 mm shanks.

The protocol presented assumes that the ultimate goal is chronic neural recording. Future studies will be needed to develop and assess protective housing for the electrode-headstage interface. Previous studies in felines have utilized a plastic “backpack” with a cover secured by screws (see FIGURE 34). This device is mounted to a metal baseplate implanted below the skin and anchored to the posterior superior pelvic crest with bone screws [13]. A

different design will likely be desired for sheep which takes into account their unique anatomy and husbandry needs.

This protocol also did not assess the method of implanting array ground wires, which originate at the electrode-headstage interface. These wires are typically anchored inside bone (such as the posterior superior pelvic crest) using a bone screw. The bone selected will depend on the chronic housing design, which may or may not use the same bone for anchoring. If the pelvis is not an available option, sufficient bony mass should be available at an unresected dorsal spinal process.

While we tried to keep the delicate nature of the microelectrode array in mind, the final protocol may need to be adjusted to avoid damaging this equipment. Chronic recovery from surgery will also need to be considered, including both the subject's potential pain as well as stability of the implanted array.

Overall, this study was an important first step toward the ultimate goal of DRG neural recording in a sheep model of SNM. These recordings could help reveal the mechanisms underlying SNM and might suggest opportunities to improve existing therapy.

Funding

This study was performed as part of an internship funded by Medtronic Inc.

Appendix B
Design and implant of chronic housing for surface DRG array

Objective

The objective of this project was to design and test a housing capable of securing and providing access to the interface for the ganglionic surface electrode array (GSEA) described in Chapter 4. This housing was to be used in chronic feline experiments with neural recording from sacral dorsal root ganglia (DRG). The design requirements were as follows:

1. Allow for the modular implant of 1 or 2 GSEAs, for either a unilateral or bilateral implant, as well as up to 2 Utah-style electrode arrays with Omnetics dual row horizontal SMT Nano Strip connectors and up to 2 bladder catheters.
2. Position the array circuit board(s) outside of the animal with the array contacts on the dorsal surface of sacral DRG and the array connector ribbon passing through a sutured surgical incision.
3. Stabilize the array circuit board(s) relative to the sacral DRG during array positioning on the DRG and for the duration of the chronic experiment to follow.
4. Protect the array circuit board(s) from manipulation by the implanted feline and from gross environmental damage (ex. litter box contents, co-housed felines, outside liquid, etc.).

5. Allow temporary access to the circuit boards, Utah array connectors, and bladder catheters for recording with Grapevine Neural Interface Processor headstages.

Design and Surgical Testing

To satisfy the design requirements, I designed a modular 3D printed plastic "backpack" to hold the array circuit boards in place underneath a removable cover. The backpack was modeled in SolidWorks computer-aided design (CAD) software (Dassault Systèmes, Vélizy-Villacoublay, France). The backpack was designed to be held in place using machined metal struts that would be secured subcutaneously to the feline's lumber vertebrae and posterior superior pelvic iliac crest using stainless steel bone screws. I performed a test implant of the backpack in an acute feline experiment and, based on its success, proceeded to a sterile implant with the intention of monitoring neural activity following surgical recovery. In both implants, a Dremel cordless rotary tool (Dremel, Racine, WI, USA) with 0.9mm burr tip (Fine Science Tools, Foster City, CA, USA) was used to drill 2 vertical holes in each pelvic crest for the pelvic struts and 1 horizontal hole through the L7 dorsal vertebral process. Following strut securement, the DRG were exposed via spinal laminectomy and implanted with Utah arrays. Implanted bladder catheters were tunneled around the animal's side to exit the dorsal incision. The right half of the backpack body was mounted to its strut, and horizontal support bars were added to hold the circuit boards in place. The circuit boards were mounted in jackets designed to adapt to these support bars. After placement and securing of the surface arrays, the dorsal incision was sutured closed, as further backpack assembly would block the surgical opening. Finally, the left half of the backpack body was fitted in place and secured to its pelvic strut and the vertebral strut. The Utah array connectors and bladder catheters were mounted to the

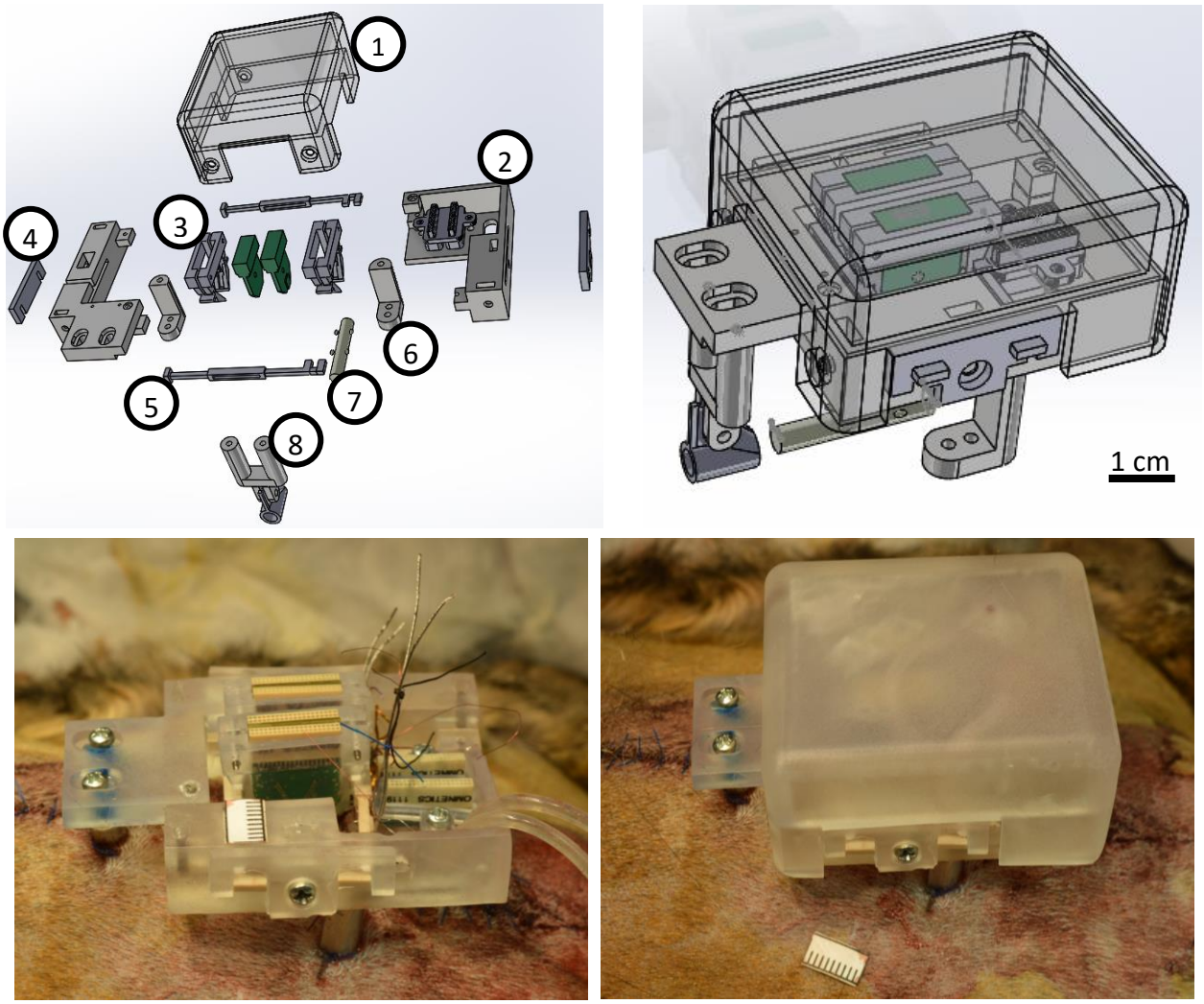

FIGURE 35: Chronic housing for surface arrays (top left) Exploded view of backpack, viewed from the rostral side as implanted, with components numbered. No scale given because of image perspective depth, see right for approximate component scale (1) Backpack cover (2) Left half of backpack body, other side visible on image left (3) Circuit board "jacket," next to green model of circuit board (4) Right support bar lock, other lock visible on image right (5) Rostral support bar (6) Left pelvic strut (7) Spinal cord and sacral DRG modeled from surgical photographs (8) Vertebral strut, supported by model of L7 vertebral process. (top right) Backpack assembly, oriented rostral-left and caudal-right. Cover is transparent for interior visibility. (bottom left) Cover removed (bottom right) Cover in place. Scale bar increments are 1 mm.

caudal side of the backpack body. Finally, the cover of the backpack was screwed in place.

FIGURE 35 shows several views of the backpack design with anatomical models for reference, as well as *in vivo* images of the backpack secured during the chronic implant surgery.

The physical implant of the device was successful in both acute and chronic surgeries, with minor design modifications following the acute surgery and improvised adjustments during the chronic surgery to correct mild warping of the plastic components following ethylene oxide sterilization. However, during the first few hours of recovery following the chronic implant, the cat rolled over in the recovery cage and broke the connection between the metal struts and the underlying bone. In a post-mortem veterinary analysis of the case, it was determined that the subject had developed a neurological condition during surgery leading to nystagmus (loss of balance and coordination). This may have been a rare reaction to ketamine anesthesia affecting motor function [199] or an underlying condition not identified prior to surgery. If the implant had been allowed more time to heal, strength of the bone-screw interface would have been expected to increase significantly across the following days or weeks [200].

While I expect that a future implant of this backpack in the absence of nystagmus would have been more successful, there are a few changes I would recommend. First, more restraint of the animal immediately after surgery would improve the odds of healing and recovery regardless of other circumstances. Second, a different choice of 3D print material would avoid warping during the sterilization process (we have observed that Formlab Clear Resin can be safely sterilized with ethylene oxide without significant shape change). Finally, re-design of the array circuit backend could allow for the design of a more streamlined implant. In our previous chronic study using Utah arrays, the circuit interface was connected to the array with a flexible wire [13], negating the need for the stiff bone fixation which failed in this experiment.

Bibliography

[1] R. V. Haberberger, C. Barry, N. Dominguez, and D. Matusica, “Human Dorsal Root Ganglia,” *Front. Cell. Neurosci.*, vol. 13, no. June, pp. 1–17, 2019.

[2] M. Hanani, “Satellite glial cells in sensory ganglia: From form to function,” *Brain Res. Rev.*, vol. 48, no. 3, pp. 457–476, 2005.

[3] V. Belzer and M. Hanani, “Nitric oxide as a messenger between neurons and satellite glial cells in dorsal root ganglia,” *Glia*, vol. 67, no. 7, pp. 1296–1307, 2019.

[4] T. R. Deer *et al.*, “Dorsal root ganglion stimulation yielded higher treatment success rate for complex regional pain syndrome and causalgia at 3 and 12 months: A randomized comparative trial,” *Pain*, vol. 158, no. 4, pp. 669–681, 2017.

[5] NSCISC, “Spinal Cord Injury Facts and Figures at a Glance,” *Natl. Spinal Cord Inj. Stat. Center, Birmingham, Alabama*, 2017.

[6] K. D. Anderson, “Targeting recovery: priorities of the spinal cord-injured population.,” *J. Neurotrauma*, vol. 21, no. 10, pp. 1371–1383, 2004.

[7] J. L. Collinger, M. L. Boninger, T. M. Bruns, K. Curley, W. Wang, and D. J. Weber, “Functional Priorities, Assistive Technology, and Brain-Computer Interfaces after Spinal Cord Injury,” *J Rehabil Res Dev*, vol. 50, no. 2, pp. 145–160, 2014.

[8] R. A. Gaunt, J. A. Hokanson, and D. J. Weber, “Microstimulation of primary afferent neurons in the L7 dorsal root ganglia using multielectrode arrays in anesthetized cats: thresholds and recruitment properties.,” *J. Neural Eng.*, vol. 6, no. 5, p. 055009, 2009.

[9] J. A. Hokanson, C. A. Ayers, R. A. Gaunt, T. M. Bruns, and D. J. Weber, “Effects of spatial and temporal parameters of primary afferent microstimulation on neural responses evoked in primary somatosensory cortex of an anesthetized cat,” in *33rd Annual International Conference of the IEEE Engineering in Medicine and Biology Society*, 2011, pp. 7533–7536.

[10] L. E. Fisher, C. A. Ayers, M. Ciollaro, V. Ventura, D. J. Weber, and R. A. Gaunt, “Chronic recruitment of primary afferent neurons by microstimulation in the feline dorsal root ganglia,” *J. Neural Eng.*, vol. 11, no. 3, p. 036007, 2014.

[11] C. A. Ayers, L. E. Fisher, R. A. Gaunt, and D. J. Weber, “Microstimulation of the lumbar DRG recruits primary afferent neurons in localized regions of lower limb,” *J. Neurophysiol.*, vol. 116, no. 1, pp. 51–60, 2016.

[12] T. M. Bruns, D. J. Weber, and R. A. Gaunt, “Microstimulation of afferents in the sacral dorsal root ganglia can evoke reflex bladder activity,” *Neurourol. Urodyn.*, vol. 34, no. September 2013, pp. 65–71, 2014.

[13] A. Khurram *et al.*, “Chronic monitoring of lower urinary tract activity via a sacral dorsal root ganglia interface,” *J. Neural Eng.*, vol. 14, no. 3, p. 036027, 2017.
[14] T. M. Bruns, R. A. Gaunt, and D. J. Weber, “Multielectrode array recordings of bladder and perineal primary afferent activity from the sacral dorsal root ganglia,” *J. Neural Eng.*, vol. 8, no. 5, p. 056010, Oct. 2011.
[15] T. M. Bruns, J. B. Wagenaar, M. J. Bauman, R. A. Gaunt, and D. J. Weber, “Real-time control of hind limb functional electrical stimulation using feedback from dorsal root ganglia recordings.,” *J. Neural Eng.*, vol. 10, no. 2, p. 026020, 2013.
[16] D. J. Weber, R. B. Stein, D. G. Everaert, and A. Prochazka, “Decoding sensory feedback from firing rates of afferent ensembles recorded in cat dorsal root ganglia in normal locomotion,” *IEEE Trans. Neural Syst. Rehabil. Eng.*, vol. 14, no. 2, pp. 240–243, 2006.
[17] R. B. Stein *et al.*, “Coding of position by simultaneously recorded sensory neurones in the cat dorsal root ganglion.,” *J. Physiol.*, vol. 560, no. 3, pp. 883–896, 2004.
[18] B. J. Holinski, D. G. Everaert, V. K. Mushahwar, and R. B. Stein, “Real-time control of walking using recordings from dorsal root ganglia.,” *J. Neural Eng.*, vol. 10, no. 5, p. 056008, 2013.
[19] T. Umeda, K. Seki, M. Sato, Y. Nishimura, M. Kawato, and T. Isa, “Population Coding of Forelimb Joint Kinematics by Peripheral Afferents in Monkeys,” *PLoS One*, vol. 7, no. 10, pp. 1–15, 2012.
[20] A. E. Snellings, P. B. Yoo, and W. M. Grill, “Urethral flow-responsive afferents in the cat sacral dorsal root ganglia.,” *Neurosci. Lett.*, vol. 516, no. 1, pp. 34–38, 2012.
[21] R. Amir and M. Devor, “Electrical excitability of the soma of sensory neurons is required for spike invasion of the soma, but not for through-conduction.,” *Biophys. J.*, vol. 84, no. 4, pp. 2181–2191, 2003.
[22] C. H. Alleyne, C. M. Cawley, D. L. Barrow, and G. D. Bonner, “Microsurgical anatomy of the dorsal cervical nerve roots and the cervical dorsal root ganglion/ventral root complexes,” *Surg. Neurol.*, vol. 50, no. 3, pp. 213–218, 1998.
[23] M. S. Cohen, E. J. Wall, R. A. Brown, B. Rydevik, and S. R. Garfin, “Cauda equina anatomy II: Extrathecal nerve roots and dorsal root ganglia,” *Spine (Phila. Pa. 1976).*, vol. 15, no. 12, pp. 1248–51, 1990.
[24] S. Kikuchi, K. Sato, S. Konno, and M. Hasue, “Anatomic and radiographic study of dorsal root ganglia.,” *Spine (Phila. Pa. 1976).*, vol. 19, no. 1, pp. 6–11, 1994.
[25] C. Hamanishi and S. Tanaka, “Dorsal root ganglia in the lumbosacral region observed from the axial views of mri,” *Spine*, vol. 18, no. 13. pp. 1753–1756, 1993.
[26] T. Hasegawa, Y. Mikawa, R. Watanabe, and H. S. An, “Morphometric analysis of the lumbosacral nerve roots and dorsal root ganglia by magnetic resonance imaging,” *Spine (Phila. Pa. 1976).*, vol. 21, no. 9, pp. 1005–1009, 1996.
[27] J. Shen, H.-Y. Wang, J.-Y. Chen, and B.-L. Liang, “Morphologic analysis of normal human lumbar dorsal root ganglion by 3D MR imaging.,” *AJNR. Am. J. Neuroradiol.*, vol. 27, no. 10, pp. 2098–103, 2006.
[28] Y. Liu, X. Zhou, J. Ma, Y. Ge, and X. Cao, “The diameters and number of nerve fibers in spinal nerve roots,” *J. Spinal Cord Med.*, vol. 38, no. 4, pp. 532–537, 2015.
[29] E. F. Hauck, M. Schwefer, W. Wittkowski, and H. W. Bothe, “Measurements and mapping of 282,420 nerve fibers in the S1-5 nerve roots.,” *J. Neurosurg. Spine*, vol. 11, no. 3, pp.

255–263, 2009.
[30] M. Ohta, K. Offord, and P. J. Dyck, “Morphometric evaluation of first sacral ganglia of man,” *J. Neurol. Sci.*, vol. 22, no. 1, pp. 73–82, 1974.
[31] J. Bossy, *Atlas of Neuroanatomy and Special Sense Organs*, 1st ed. Philadelphia: WB Saunders, 1970.
[32] M. Sato, G. Austin, S. Makoto, and A. George, “Intracellular Potentials of Mammalian Dorsal Root Ganglion Cells,” *J. Neurophysiol.*, vol. 24, no. 6, pp. 569–582, 1961.
[33] H. Burton and J. J. McFarlane, “The organization of the seventh lumbar spinal ganglion of the cat.,” *J. Comp. Neurol.*, vol. 149, no. 2, pp. 215–232, 1973.
[34] A. Puigdellívol-Sánchez, A. Prats-Galino, D. Ruano-Gil, and C. Molander, “Sciatic and femoral nerve sensory neurones occupy different regions of the L4 dorsal root ganglion in the adult rat,” *Neurosci. Lett.*, vol. 251, no. 3, pp. 169–172, 1998.
[35] W. J. T. Wessels, H. K. P. Feirabend, and E. Marani, “Evidence for a rostrocaudal organization in dorsal root ganglia during development as demonstrated by intra-uterine WGA-HRP injections into the hindlimb of rat fetuses,” *Dev. Brain Res.*, vol. 54, no. 2, pp. 273–281, 1990.
[36] M. Kausz and M. Rethelyi, “Lamellar Arrangement of Neuronal Somata in the Dorsal Root Ganglion of the Cat,” *Somatosens. Res.*, vol. 2, no. 3, pp. 193–204, 1985.
[37] J. Yan, R. Tian, and M. Horiguchi, “Distribution of sensory neurons of ventral and dorsal cervical cutaneous nerves in dorsal root ganglia of adult rat - a double-label study using DiO and DiI,” *Okajimas Folia Anat. Jpn.*, vol. 79, no. 5, pp. 129–133, 2002.
[38] M. A. Moffitt and C. C. McIntyre, “Model-based analysis of cortical recording with silicon microelectrodes,” *Clin. Neurophysiol.*, vol. 116, pp. 2240–2250, 2005.
[39] D. N. Hill *et al.*, “Intracellular Features Predicted by Extracellular Recordings in the Hippocampus In Vivo Intracellular Features Predicted by Extracellular Recordings in the Hippocampus In Vivo,” pp. 390–400, 2011.
[40] A. I. Kashkoush, R. A. Gaunt, L. E. Fisher, T. M. Bruns, and D. J. Weber, “Recording single- and multi-unit neuronal action potentials from the surface of the dorsal root ganglion,” *Sci. Rep.*, vol. 9, no. 1, p. 2786, 2019.
[41] R. A. Gaunt, T. M. Bruns, D. J. Crammond, N. D. Tomycz, J. J. Moossy, and D. J. Weber, “Single- and multi-unit activity recorded from the surface of the dorsal root ganglia with non-penetrating electrode arrays,” *Proc. Annu. Int. Conf. IEEE Eng. Med. Biol. Soc. EMBS*, pp. 6713–6716, 2011.
[42] R. D. Graham, T. M. Bruns, B. Duan, and S. F. Lempka, “Dorsal root ganglion stimulation for chronic pain modulates Aβ-fiber activity but not C-fiber activity: A computational modeling study,” *Clin. Neurophysiol.*, vol. 130, pp. 941–951, 2019.
[43] D. J. Bourbeau, J. A. Hokanson, J. E. Rubin, and D. J. Weber, “A computational model for estimating recruitment of primary afferent fibers by intraneural stimulation in the dorsal root ganglia,” *J. Neural Eng.*, vol. 8, no. 5, p. 056009, 2011.
[44] Y. Aoyagi, R. B. Stein, A. Branner, K. G. Pearson, and R. A. Normann, “Capabilities of a penetrating microelectrode array for recording single units in dorsal root ganglia of the cat,” *J. Neurosci. Methods*, vol. 128, pp. 9–20, 2003.
[45] A. Prochazka and M. Gorassini, “Models of ensemble firing of muscle spindle afferents recorded during normal locomotion in cats,” *J. Physiol.*, vol. 507, no. 1, pp. 277–291,

1998.
[46] D. J. Edell, V. Van Toi, V. M. McNeil, and L. D. Clark, “Factors Influencing the Biocompatibility of Insertable Silicon Microshafts in Cerebral Cortex,” *IEEE Trans. Biomed. Eng.*, vol. 39, no. 6, pp. 635–643, 1992.
[47] V. S. Polikov, P. A. Tresco, and W. M. Reichert, “Response of brain tissue to chronically implanted neural electrodes,” *J. Neurosci. Methods*, vol. 148, no. 1, pp. 1–18, 2005.
[48] H. A. C. Wark, K. S. Mathews, R. A. Normann, and E. Fernandez, “Behavioral and cellular consequences of high-electrode count Utah Arrays chronically implanted in rat sciatic nerve.,” *J. Neural Eng.*, vol. 11, no. 4, p. 046027, 2014.
[49] A. K. Ostrowski, Z. J. Sperry, G. Kulik, and T. M. Bruns, “Quantitative models of feline lumbosacral dorsal root ganglia cell density,” *Neurosci. Methods*, vol. 290, pp. 116–124, 2017.
[50] V. Miletic and G. W. Lu, “Characteristics of action potentials recorded from cat spinal ganglion neurons in vivo.,” *Brain Res. Bull.*, vol. 31, no. 5, pp. 531–538, 1993.
[51] S. M. Lawrence, G. S. Dhillon, W. Jensen, K. Yoshida, and K. W. Horch, “Acute peripheral nerve recording characteristics of polymer-based longitudinal intrafascicular electrodes,” *IEEE Trans. Neural Syst. Rehabil. Eng.*, vol. 12, no. 3, pp. 345–348, 2004.
[52] T. Boretius *et al.*, “A transverse intrafascicular multichannel electrode (TIME) to interface with the peripheral nerve.,” *Biosens. Bioelectron.*, vol. 26, no. 1, pp. 62–69, Sep. 2010.
[53] J. R. Lachapelle *et al.*, “An implantable, designed-for-human-use peripheral nerve stimulation and recording system for advanced prosthetics,” in *Engineering in Medicine and Biology Society (EMBC), 2016 IEEE 38th Annual International Conference of the*, 2016, pp. 1794–1797.
[54] B. Rubehn and T. Stieglitz, “In vitro evaluation of the long-term stability of polyimide as a material for neural implants,” *Biomaterials*, vol. 31, no. 13, pp. 3449–3458, 2010.
[55] J. J. Jun *et al.*, “Fully integrated silicon probes for high-density recording of neural activity,” *Nature*, vol. 551, no. 7679, pp. 232–236, 2017.
[56] B. C. Raducanu *et al.*, “Time multiplexed active neural probe with 678 parallel recording sites,” *Eur. Solid-State Device Res. Conf.*, vol. 2016-Octob, pp. 385–388, 2016.
[57] C. W. Lee, A. a Szymanska, S. C. Wu, A. L. Swindlehurst, and Z. Nenadic, “A Method for Neuronal Source Identification,” p. 14, 2013.
[58] J. J. Jun, C. Mitelut, C. Lai, S. L. Gratiy, C. A. Anastassiou, and T. D. Harris, “Real-time spike sorting platform for high-density extracellular probes with ground-truth validation and drift correction,” *bioRxiv*, pp. 1–29, 2017.
[59] M. Pachitariu, N. Steinmetz, S. Kadir, M. Carandini, and K. D. Harris, “Kilosort: realtime spikesorting for extracellular electrophysiology with hundreds of channels,” pp. 1–14, 2016.
[60] J. E. Chung *et al.*, “A Fully Automated Approach to Spike Sorting,” *Neuron*, vol. 95, no. 6, pp. 1381-1394.e6, 2017.
[61] M. S. Cohen, E. J. Wall, R. A. Brown, B. Rydevik, and S. R. Garfin, “Cauda Equina Anatomy II: Extrathecal Nerve Roots and Dorsal Root Ganglia,” in *North American Spine Society*, 1989, vol. 15, no. 12, pp. 1248–1251.
[62] S. Kikuchi, K. Sato, S. Konno, and M. Hasue, “Anatomic and radiographic study of dorsal root ganglia,” *Spine (Phila. Pa. 1976).*, vol. 19, no. 1, pp. 6–11, 1994.

[63] N. A. Ebraheim and J. Lu, “Morphometric evaluation of the sacral dorsal root ganglia. A cadaveric study.,” *Surg. Radiol. Anat.*, vol. 20, no. 2, pp. 105–108, 1998.
[64] M. Devor, “Unexplained peculiarities of the dorsal root ganglion.,” *Pain*, vol. Suppl 6, pp. S27–S35, Aug. 1999.
[65] A. A. Harper and S. N. Lawson, “Conduction velocity is related to morphological cell type in rat dorsal root ganglion neurones.,” *J. Physiol.*, vol. 359, pp. 31–46, 1985.
[66] U. Hoheisel, S. Mense, A. I. Iii, U. Heidelberg, and F. R. G. Heidelberg, “Observations on the morphology of axons and somata of slowly conducting dorsal root ganglion cells in the cat,” *Brain Res.*, vol. 423, pp. 269–278, 1987.
[67] K. H. Lee, K. Chung, J. M. Chung, and R. E. Coggeshall, “Correlation of cell body size, axon size, and signal conduction velocity for individually labelled dorsal root ganglion cells in the cat,” *J. Comp. Neurol.*, vol. 243, no. 3, pp. 335–346, 1986.
[68] H. H. Aldskogius and M. M. Risling, “Number of dorsal root ganglion neurons and axons in cats of different ages,” *Exp. Neurol.*, vol. 106, no. 1, pp. 70–73, 1989.
[69] K. Chung and R. E. Coggeshall, “The ration of dorsal root ganglion cells to dorsal root axons in sacral segments of the cat,” *J. Comp. Neurol.*, vol. 225, no. 1, pp. 24–30, 1984.
[70] T. Tandrup, “Unbiased estimates of number and size of rat dorsal root ganglion cells in studies of structure and cell survival,” vol. 192, pp. 173–192, 2004.
[71] H. Burton and J. J. McFarlane, “The Organization of the Seventh Lumbar Spinal Ganglion of the Cat,” *J. Comp. Neurol.*, vol. 149, no. 2, pp. 215–232, 1986.
[72] J. Yan, R. Tian, and M. Horiguchi, “Distribution of Sensory Neurons of Ventral and Dorsal Cervical Cutaneous Nerves in Dorsal Root Ganglia of Adult Rat - A Double-Label Study Using DiO and DiI.,” *Okajimas Folia Anat. Jpn.*, vol. 79, no. 5, pp. 129–133, 2002.
[73] H. Lu, C. A. Chestek, K. M. Shaw, and H. J. Chiel, “Selective extracellular stimulation of individual neurons in ganglia,” *J. Neural Eng.*, vol. 5, no. 3, pp. 287–309, 2009.
[74] P. S. Spencer, C. S. Raine, and H. Wiśniewski, “Axon diameter and myelin thickness. Unusual relationships in dorsal root ganglia.,” *Anat. Rec.*, vol. 176, no. 2, pp. 225–243, Jun. 1973.
[75] M. Dobretsov, S. L. Hastings, T. J. Sims, J. R. Stimers, and D. Romanovsky, “Stretch receptor-associated expression of alpha-3 isoform of the Na+,K+-ATPase in rat peripheral nervous system,” *Neuroscience*, vol. 116, no. 4, pp. 1069–1080, 2003.
[76] R. F. McLain and J. N. Weinstein, “Morphometric Model of Normal Rabbit Dorsal Root Ganglia,” *Spine J.*, vol. 18, no. 13, pp. 1746–1752, 1993.
[77] G. Kulik, Z. J. Sperry, A. K. Ostrowski, and T. M. Bruns, “DRG Cross Section Analysis,” *Open Science Framework*, 2017. .
[78] Z. J. Sperry *et al.*, “Dorsal root ganglia neural recordings with a novel non-penetrating thin-film microelectrode array,” in *Society for Neuroscience Annual Meeting*, 2015, p. 540.04.
[79] T. R. Deer, E. Grigsby, R. L. Weiner, B. Wilcosky, and J. M. Kramer, “A prospective study of dorsal root ganglion stimulation for the relief of chronic pain,” *Neuromodulation*, vol. 16, no. 1, pp. 67–72, 2013.
[80] E. S. Krames, “The dorsal root ganglion in chronic pain and as a target for neuromodulation: A review,” *Neuromodulation*, vol. 18, no. 1, pp. 24–32, 2015.
[81] Z. Ouyang, Z. J. Sperry, N. D. Barrera, and T. M. Bruns, “Real-time Bladder Pressure

Estimation for Closed-loop Control in a Detrusor Overactivity Model," *IEEE Trans. Neural Syst. Rehabil. Eng.*, 2019.
[82] C. Harrison, S. Epton, S. Bojanic, A. L. Green, and J. J. FitzGerald, "The Efficacy and Safety of Dorsal Root Ganglion Stimulation as a Treatment for Neuropathic Pain: A Literature Review," *Neuromodulation*, vol. 21, no. 3, pp. 225–233, 2018.
[83] W. Kneist, D. W. Kauff, M. Schröder, K. P. Koch, and H. Lang, "Percutaneous nerve evaluation based on electrode placement under control of autonomic innervation," *Tech. Coloproctol.*, vol. 18, no. 8, pp. 725–730, 2014.
[84] C. C. McIntyre and W. M. Grill, "Excitation of central nervous system neurons by nonuniform electric fields," *Biophys. J.*, vol. 76, no. 2, pp. 878–888, 1999.
[85] A. E. Dubin and A. Patapoutian, "Nociceptors: the sensors of the pain pathway," *J. Clin. Invest.*, vol. 120, no. 11, pp. 3760–3772, 2010.
[86] D. L. Winter, "Receptor characteristics and conduction velocites in bladder afferents.," *J. Psychiatr. Res.*, vol. 8, no. 3, pp. 225–235, Aug. 1971.
[87] E. P. Gardner and K. O. Johnson, "The Somatosensory System: Receptors and Central Pathways," in *Principles of Neural Science, Fifth Edition*, New York, NY: McGraw-Hill Education, 2014.
[88] W. J. T. Wessels, H. K. P. Feirabend, and E. Marani, "Somatotopic organization in the sensory innervation of the rat hindlimb during development, using half dorsal root ganglia as subsegmental units.," *Eur. J. Morphol.*, vol. 28, no. 2–4, pp. 394–403, 1990.
[89] A. Prats-Galino, A. Puigdellívol-Sánchez, D. Ruano-Gil, and C. Molander, "Representations of hindlimb digits in rat dorsal root ganglia," *J. Comp. Neurol.*, vol. 408, no. 1, pp. 137–145, 1999.
[90] M. Kausz and M. Rethelyi, "Lamellar arrangment of neuronal somata in the dorsal root ganglion of the cat," *Somatosens. Res.*, vol. 2, no. 3, pp. 193–204, 1985.
[91] J. Peyronnard, J. Messier, M. Dubreuil, L. Charron, and F. Lebel, "Three-dimensional computer-aided analysis of the intraganglionic topography of primary muscle afferent neurons in the rat," *Anat. Rec.*, vol. 227, no. 4, pp. 405–417, 1990.
[92] J. A. Vega, J. M. Humara, F. J. Naves, I. Esteban, and M. E. Del Valle, "Immunoreactivity for phosphorylated 200-kDa neurofilament subunit is heterogeneously expressed in human sympathetic and primary sensory neurons," *Anat. Embryol. (Berl).*, vol. 190, no. 5, pp. 453–459, 1994.
[93] C. Rostock, K. Schrenk-Siemens, J. Pohle, and J. Siemens, "Human vs. Mouse Nociceptors - Similarities and Differences," *Neuroscience*, vol. 387, pp. 13–27, 2018.
[94] A. A. Taha and A. Hanbury, "Metrics for evaluating 3D medical image segmentation: Analysis, selection, and tool," *BMC Med. Imaging*, vol. 15, no. 1, 2015.
[95] S. Wienert *et al.*, "Detection and segmentation of cell nuclei in virtual microscopy images: A minimum-model approach," *Sci. Rep.*, vol. 2, pp. 1–7, 2012.
[96] K. Offord, M. Ohta, R. F. Oenning, and P. J. Dyck, "Method of morphometric evaluation of spinal and autonomic ganglia," *J. Neurol. Sci.*, vol. 22, no. 1, pp. 65–71, 1974.
[97] M. P. Silverstein, L. J. Romrell, E. C. Benzel, N. Thompson, S. Griffith, and I. H. Lieberman, "Lumbar Dorsal Root Ganglia Location: An Anatomic and MRI Assessment," *Int. J. Spine Surg.*, vol. 9, p. 3, Jan. 2015.
[98] A. Josephson, J. Widenfalk, A. Trifunovski, H. R. Widmer, L. Olson, and C. Spenger, "GDNF

and NGF family members and receptors in human fetal and adult spinal cord and dorsal root ganglia," *J. Comp. Neurol.*, vol. 440, no. 2, pp. 204–217, 2001.
[99] K. M. Flegal, M. D. Carroll, B. K. Kit, and C. L. Ogden, "Prevalence of Obesity and Trends in the Distribution of Body Mass Index Among US Adults, 1999-2010," *JAMA*, vol. 307, no. 5, p. 491, Feb. 2012.
[100] M. Devor and R. Govrin-Lippmann, "Neurogenesis in adult rat dorsal root ganglia," *Neurosci. Lett.*, vol. 61, no. 1–2, pp. 189–194, 1985.
[101] M. Devor and R. Govrin-Lippmann, "Neurogenesis in adult rat dorsal root ganglia: On counting and the count," *Somatosens. Mot. Res.*, vol. 8, no. 1, pp. 9–12, 1991.
[102] H. Aldskogius and M. Risling, "Effect of sciatic neurectomy on neuronal number and size distribution in the L7 ganglion of kittens," *Exp. Neurol.*, vol. 74, no. 2, pp. 597–604, 1981.
[103] L. A. Langford and R. E. Coggeshall, "Branching of sensory axons in the dorsal root and evidence for the absence of dorsal root efferent fibers," *J. Comp. Neurol.*, vol. 184, no. 1, pp. 193–204, 1979.
[104] L. A. Langford and R. E. Coggeshall, "Branching of sensory axons in the peripheral nerve of the rat," *J. Comp. Neurol.*, vol. 203, no. 4, pp. 745–750, Dec. 1981.
[105] M. Risling, H. Aldskogius, C. Hildebrand, and S. Remahl, "Effects of sciatic nerve resection on L7 spinal roots and dorsal root ganglia in adult cats," *Exp. Neurol.*, vol. 82, no. 3, pp. 568–580, 1983.
[106] H. A. Davenport and R. T. Bothe, "Cells and fibers in spinal nerves. II. A study of C2, C6, T4, T9, L3, S2, and S5 in man," *J. Comp. Neurol.*, vol. 59, no. 1, pp. 167–174, Feb. 1934.
[107] A. S. Koopmeiners, S. Mueller, J. Kramer, and Q. H. Hogan, "Effect of Electrical Field Stimulation on Dorsal Root Ganglion Neuronal Function," *Neuromodulation Technol. Neural Interface*, vol. 16, no. 4, pp. 304–311, Jul. 2013.
[108] A. R. Kent, X. Min, Q. H. Hogan, and J. M. Kramer, "Mechanisms of Dorsal Root Ganglion Stimulation in Pain Suppression: A Computational Modeling Analysis," *Neuromodulation*, vol. 21, no. 3, pp. 234–246, 2018.
[109] C. A. West, A. McKay Hart, G. Terenghi, and M. Wiberg, "Sensory neurons of the human brachial plexus: A quantitative study employing optical fractionation and in vivo volumetric magnetic resonance imaging," *Neurosurgery*, vol. 70, no. 5, pp. 1183–1194, 2012.
[110] W. Chang, T. Berta, Y. H. Kim, S. Lee, S. Y. Lee, and R. R. Ji, "Expression and Role of Voltage-Gated Sodium Channels in Human Dorsal Root Ganglion Neurons with Special Focus on Nav1.7, Species Differences, and Regulation by Paclitaxel," *Neurosci. Bull.*, vol. 34, no. 1, pp. 4–12, 2018.
[111] Z. J. Sperry *et al.*, "Flexible microelectrode array for interfacing with the surface of neural ganglia," *J. Neural Eng.*, vol. 15, no. 3, p. 036027, 2018.
[112] S. Hamid and R. Hayek, "Role of electrical stimulation for rehabilitation and regeneration after spinal cord injury: An overview," *Eur. Spine J.*, vol. 17, no. 9, pp. 1256–1269, 2008.
[113] R. Van Den Brand *et al.*, "Restoring voluntary control of locomotion after paralyzing spinal cord injury.," *Science*, vol. 336, no. 6085, pp. 1182–5, 2012.
[114] J. L. Collinger, S. Foldes, T. M. Bruns, B. Wodlinger, R. Gaunt, and D. J. Weber, "Neuroprosthetic technology for individuals with spinal cord injury," *J. Spinal Cord Med.*, vol. 36, no. 4, pp. 258–272, 2013.

[115] S. E. Ross, Z. J. Sperry, C. M. Mahar, and T. M. Bruns, “Hysteretic behavior of bladder afferent neurons in response to changes in bladder pressure,” *BMC Neurosci.*, vol. 17, no. 57, pp. 1–12, 2016.
[116] A. C. Patil and N. V. Thakor, “Implantable neurotechnologies: a review of micro- and nanoelectrodes for neural recording,” *Med. Biol. Eng. Comput.*, vol. 54, no. 1, pp. 23–44, 2016.
[117] D. J. Tyler and D. M. Durand, “Functionally selective peripheral nerve stimulation with a flat interface nerve electrode,” *IEEE Trans. Neural Syst. Rehabil. Eng.*, vol. 10, no. 4, pp. 294–303, 2002.
[118] J. Perez-Orive and D. M. Durand, “Modeling study of peripheral nerve recording selectivity.,” *IEEE Trans. Rehabil. Eng.*, vol. 8, no. 3, pp. 320–329, 2000.
[119] D. M. Durand, “Selective Fascicular Recording of the Hypoglossal Nerve Using a Multi-Contact Nerve Cuff Electrode,” *Image (Rochester, N.Y.)*, pp. 2172–2175, 2003.
[120] D.-H. Kim *et al.*, “Dissolvable films of silk fibroin for ultrathin conformal bio-integrated electronics.,” *Nat. Mater.*, vol. 9, no. 6, pp. 511–517, 2010.
[121] I. R. Minev *et al.*, “Electronic dura mater for long-term multimodal neural interfaces,” *Science (80-.).*, vol. 347, no. 6218, pp. 159–163, 2015.
[122] D. C. Rodger *et al.*, “Flexible parylene-based multielectrode array technology for high-density neural stimulation and recording,” *Sensors Actuators, B Chem.*, vol. 132, no. 2, pp. 449–460, 2008.
[123] J. Ordonez, M. Schuettler, C. Boehler, T. Boretius, and T. Stieglitz, “Thin films and microelectrode arrays for neuroprosthetics,” *MRS Bull.*, vol. 37, no. 6, pp. 590–598, 2012.
[124] M. J. Cullins and H. J. Chiel, “Electrode fabrication and implantation in Aplysia californica for multi-channel neural and muscular recordings in intact, freely behaving animals.,” *J. Vis. Exp.*, no. 40, p. e1791, 2010.
[125] A. R. Duke, M. W. Jenkins, H. Lu, J. M. McManus, H. J. Chiel, and E. D. Jansen, “Transient and selective suppression of neural activity with infrared light.,” *Sci. Rep.*, vol. 3, p. 2600, 2013.
[126] J. L. Novak and B. C. Wheeler, “Recording from the Aplysia abdominal ganglion with a planar microelectrode array.,” *IEEE Trans. Biomed. Eng.*, vol. 33, no. 2, pp. 196–202, 1986.
[127] C. A. Harris, P. A. Passaro, I. Kemenes, G. Kemenes, and M. O’Shea, “Sensory driven multi-neuronal activity and associative learning monitored in an intact CNS on a multielectrode array,” *J. Neurosci. Methods*, vol. 186, no. 2, pp. 171–178, 2010.
[128] J. Yang, H. Lu, N. Kodama, T. Feng, R. Fernandez Galen, and H. J. Chiel, “Neural dynamics of a feeding pattern-generating circuit in the marine mollusk Aplysia californica,” in *Society for Neuroscience 47th Annual Meeting*, 2017.
[129] I. Hurwitz, D. Neustadter, D. W. Morton, H. J. Chiel, and A. J. Susswein, “Activity patterns of the B31/B32 pattern initiators innervating the I2 muscle of the buccal mass during normal feeding movements in Aplysia californica.,” *J. Neurophysiol.*, vol. 75, no. 4, pp. 1309–26, 1996.
[130] H. Ye, D. W. Morton, and H. J. Chiel, “Neuromechanics of multifunctionality during swallowing in Aplysia californica.,” *J. Neurosci.*, vol. 26, no. 5, pp. 1470–85, 2006.
[131] D. W. Morton and H. J. Chiel, “The timing of activity in motor neurons that produce

radula movements distinguishes ingestion from rejection in Aplysia," *J. Comp. Physiol. A*, vol. 172, no. 1, pp. 17–32, 1993.
[132] H. Lu, J. M. McManus, and H. J. Chiel, "Extracellularly identifying motor neurons for a muscle motor pool in Aplysia californica," *J Vis Exp*, vol. 73, no. March, p. e50189, 2013.
[133] R. A. Kuhn, "Organization of Tactile Dermatomes in Cat and Monkey," *J. Neurophysiol.*, vol. 16, pp. 169–182, 1952.
[134] R. Q. Quiroga, Z. Nadasdy, and Y. Ben-Shaul, "Unsupervised Spike Detection and Sorting with Wavelets and Superparamagnetic Clustering," *Neural Comput.*, vol. 16, no. 8, pp. 1661–1687, 2004.
[135] A. M. Bruno, W. N. Frost, and M. D. Humphries, "Modular deconstruction reveals the dynamical and physical building blocks of a locomotion motor program," *Neuron*, vol. 86, no. 1, pp. 304–318, 2015.
[136] D. G. Bonett and T. A. Wright, "Sample size requirements for estimating Pearson, Kendall and Spearman correlations," *Psychometrika*, vol. 65, no. 1, pp. 23–28, 2000.
[137] C. W. Lee, H. Dang, and Z. Nenadic, "An efficient algorithm for current source localization with tetrodes.," *Conf. Proc. IEEE Eng. Med. Biol. Soc.*, vol. 2007, pp. 1282–1285, 2007.
[138] Y. Zhao, D. O. Wang, and K. C. Martin, "Preparation of Aplysia sensory-motor neuronal cell cultures.," *J. Vis. Exp.*, no. 28, pp. 7–9, 2009.
[139] N. Peck-Dimit, Z. J. Sperry, and T. M. Bruns, "Flexible microelectrode array recordings from neural ganglia," *Open Sci. Framew.*, 2018.
[140] G. W. Gross, "Simultaneous Single Unit Recording in vitro with a Photoetched Laser Deinsulated Gold Multimicroelectrode Surface," *IEEE Trans. Biomed. Eng.*, vol. BME-26, no. 5, pp. 273–279, 1979.
[141] J. M. McManus, H. Lu, and H. J. Chiel, "An in vitro preparation for eliciting and recording feeding motor programs with physiological movements in Aplysia californica.," *J. Vis. Exp.*, no. 70, p. e4320, 2012.
[142] D. Khodagholy *et al.*, "NeuroGrid : recording action potentials from the surface of the brain," *Nat. Neurosci.*, vol. 18, no. 2, pp. 310–315, 2014.
[143] S. Lee *et al.*, "Selective stimulation and neural recording on peripheral nerves using flexible split ring electrodes," *Sensors Actuators, B Chem.*, vol. 242, pp. 1165–1170, 2017.
[144] A. S. Caravaca *et al.*, "A novel flexible cuff-like microelectrode for dual purpose, acute and chronic electrical interfacing with the mouse cervical vagus nerve," *J. Neural Eng.*, vol. 14, no. 6, p. 066005, 2017.
[145] C. A. Diaz-Botia *et al.*, "A silicon carbide array for electrocorticography and peripheral nerve recording," *J. Neural Eng.*, vol. 14, p. 056006, 2017.
[146] C. M. Gray, P. E. Maldonado, M. Wilson, and B. McNaughton, "Tetrodes markedly improve the reliability and yield of multiple single-unit isolation from multi-unit recordings in cat striate cortex," *J. Neurosci. Methods*, vol. 63, no. 1–2, pp. 43–54, 1995.
[147] C. W. Lee, A. a. Szymanska, Y. Ikegaya, and Z. Nenadic, "The accuracy and precision of signal source localization with tetrodes," *Proc. Annu. Int. Conf. IEEE Eng. Med. Biol. Soc. EMBS*, pp. 531–534, 2013.
[148] A. A. Schendel *et al.*, "The effect of micro-ECoG substrate footprint on the meningeal tissue response.," *J. Neural Eng.*, vol. 11, no. 4, p. 046011, 2014.
[149] S. E. Ross, Z. Ouyang, S. Rajagopalan, and T. M. Bruns, "Evaluation of Decoding

Algorithms for Estimating Bladder Pressure from Dorsal Root Ganglia Neural Recordings," *Ann. Biomed. Eng.*, vol. 46, no. 2, pp. 233–246, Feb. 2018.
[150] D. J. Weber, R. B. Stein, D. G. Everaert, and A. Prochazka, "Limb-state feedback from ensembles of simultaneously recorded dorsal root ganglion neurons.," *J. Neural Eng.*, vol. 4, no. 3, pp. S168–S180, 2007.
[151] J. Rigosa, D. J. Weber, A. Prochazka, R. B. Stein, and S. Micera, "Neuro-fuzzy decoding of sensory information from ensembles of simultaneously recorded dorsal root ganglion neurons for functional electrical stimulation applications," in *Journal of Neural Engineering*, 2011, vol. 8, no. 4.
[152] P. J. Rousche, D. S. Pellinen, D. P. Pivin, J. C. Williams, R. J. Vetter, and D. R. Kipke, "Flexible polyimide-based intracortical electrode arrays with bioactive capability," *IEEE Trans. Biomed. Eng.*, vol. 48, no. 3, pp. 361–371, 2001.
[153] W.-C. Huang *et al.*, "Ultracompliant Hydrogel-Based Neural Interfaces Fabricated by Aqueous-Phase Microtransfer Printing," *Adv. Funct. Mater.*, vol. 1801059, p. 1801059, 2018.
[154] K. Na *et al.*, "Novel diamond shuttle to deliver flexible bioelectronics with reduced tissue compression," *bioRxiv*, p. 435800, Jan. 2018.
[155] P. R. Patel *et al.*, "Chronic in vivo stability assessment of carbon fiber microelectrode arrays," *J. Neural Eng.*, vol. 13, no. 6, p. 066002, Dec. 2016.
[156] A. Rodriguez and A. Laio, "Clustering by fast search and find of density peaks," *Science (80-.).*, vol. 344, no. 6191, pp. 1492–1496, 2014.
[157] A. Rodriguez, M. D'Errico, E. Facco, and A. Laio, "Computing the Free Energy without Collective Variables," *J. Chem. Theory Comput.*, vol. 14, no. 3, pp. 1206–1215, 2018.
[158] J. P. Seymour, F. Wu, K. D. Wise, and E. Yoon, "State-of-the-art mems and microsystem tools for brain research," *Microsystems Nanoeng.*, vol. 3, no. March 2016, pp. 1–16, 2017.
[159] A. Juavinett, G. Bekheet, and A. Churchland, "Chronically-implanted Neuropixels probes enable high yield recordings in freely moving mice," *Protoc. Exch.*, pp. 1–17, 2019.
[160] G. A. Clark, N. M. Ledbetter, D. J. Warren, and R. R. Harrison, "Recording sensory and motor information from peripheral nerves with Utah Slanted Electrode Arrays," *Proc. Annu. Int. Conf. IEEE Eng. Med. Biol. Soc. EMBS*, pp. 4641–4644, 2011.
[161] P. J. Rousche and R. A. Normann, "A method for pneumatically inserting an array of penetrating electrodes into cortical tissue," *Ann. Biomed. Eng.*, vol. 20, no. 4, pp. 413–422, 1992.
[162] A. Branner, R. B. Stein, E. Fernandez, Y. Aoyagi, and R. A. Normann, "Long-Term Stimulation and Recording with a Penetrating Microelectrode Array in Cat Sciatic Nerve," *IEEE Trans. Biomed. Eng.*, vol. 51, no. 1, pp. 146–157, 2004.
[163] M. B. Christensen, S. M. Pearce, N. M. Ledbetter, D. J. Warren, G. A. Clark, and P. A. Tresco, "The foreign body response to the Utah Slant Electrode Array in the cat sciatic nerve," *Acta Biomater.*, vol. 10, no. 11, pp. 4650–4660, 2014.
[164] D. McCreery, S. Cogan, S. Kane, and V. Pikov, "Correlations between histology and neuronal activity recorded by microelectrodes implanted chronically in the cerebral cortex," *J. Neural Eng.*, vol. 13, no. 3, p. 036012, 2016.
[165] T. D. Y. Kozai *et al.*, "Reduction of neurovascular damage resulting from microelectrode

insertion into the cerebral cortex using in vivo two-photon mapping," *J. Neural Eng.*, vol. 7, no. 4, pp. 1–22, 2010.
[166] T. L. Hanson, C. A. Diaz-Botia, V. Kharazia, M. M. Maharbiz, and P. N. Sabes, "The 'sewing machine' for minimally invasive neural recording," *bioRxiv*, no. 1, p. 578542, 2019.
[167] V. Gaillet *et al.*, "Spatially selective activation of the visual cortex via intraneural stimulation of the optic nerve," *Nat. Biomed. Eng.*, 2019.
[168] V. Miletic and G.-W. W. Lu, "Characteristics of action potentials recorded from cat spinal ganglion neurons in vivo.," *Brain Res. Bull.*, vol. 31, no. 5, pp. 531–538, 1993.
[169] D. H. Abramson, A. C. Schefler, D. Almeida, and R. Folberg, "Optic nerve tissue shrinkage during pathologic processing after enucleation for retinoblastoma," *Arch. Ophthalmol.*, vol. 121, no. 1, pp. 73–75, 2003.
[170] C. Rostock, K. Schrenk-Siemens, J. Pohle, and J. Siemens, "Human vs. Mouse Nociceptors – Similarities and Differences," *Neuroscience*, vol. 387, pp. 13–27, 2018.
[171] T. N. Salthouse, "Luxol fast blue arn: A new solvent azo dye with improved staining qualities for myelin and phospholipids," *Biotech. Histochem.*, vol. 37, no. 5, pp. 313–316, 1962.
[172] S. Hatai, "Number and size of the spinal ganglion cells and dorsal root fibers in the white rat at different ages," *J. Comp. Neurol.*, vol. 12, no. 2, pp. 107–124, 1902.
[173] L. Zirpel, J. Herron, T. S. Brink, B. Isaacson, S. Stanslaski, and T. Denison, "Peripheral nerve neuromodulation of urological function using a distributed sensing and stimulation system," *Soc. Neurosci. 47th Annu. Meet.*, 2017.
[174] L. Zirpel and T. S. Brink, "Increasing bladder capacity in a fully-conscious, large animal model: sacral nerve stimulation targeted to late stages of bladder fill-cycle has efficacy similar to continuous stimulation," in *Society for Neuroscience 47th Annual Meeting*, 2017.
[175] L. Zirpel *et al.*, "Correlation of sacral nerve lead targeting and urological efficacy: motor mapping, electrode position, and stimulation amplitude," *Transl. Androl. Urol.*, vol. 5, no. S2, pp. AB291–AB291, 2016.
[176] T. S. Brink, P. L. Zimmerman, M. A. Mattson, X. Su, and D. E. Nelson, "A chronic, conscious large animal platform to quantify therapeutic effects of sacral neuromodulation on bladder function," *J. Urol.*, vol. 194, no. 1, pp. 252–258, 2015.
[177] T. S. Brink, X. Su, P. L. Zimmerman, and D. E. Nelson, "Development and Use of a Large Animal Model for Chronic Testing of Sacral Neuromodulation Therapies Using Conscious Cystometry To Quantify Urological Effects," in *International Continence Society*, 2014, p. 713.
[178] E. E. Horvath, P. B. Yoo, C. L. Amundsen, G. D. Webster, and W. M. Grill, "Conditional and continuous electrical stimulation increase cystometric capacity in persons with spinal cord injury," *Neurourol. Urodyn.*, vol. 29, no. 3, pp. 401–407, 2010.
[179] L. E. Tennyson, C. Tai, and C. J. Chermansky, "Using the Native Afferent Nervous System to Sense Bladder Fullness : State of the Art," *Curr. Bladder Dysfunct. Rep.*, vol. 11, no. 4, pp. 346–349, 2017.
[180] A. Mendez and M. Sawan, "Chronic monitoring of bladder volume: a critical review and assessment of measurement methods.," *Can. J. Urol.*, vol. 18, no. 1, pp. 5504–16, Feb. 2011.

[181] J. Melgaard and N. J. M. Rijkhoff, “Detecting Urinary Bladder Contractions: Methods and Devices,” *J. Sens. Technol.*, vol. 4, no. December, pp. 165–176, 2014.
[182] F. Zhang *et al.*, “Neural pathways involved in sacral neuromodulation of reflex bladder activity in cats,” *Am. J. Physiol. Physiol.*, vol. 304, no. 6, pp. F710–F717, 2013.
[183] B. Amend, K. E. Matzel, P. Abrams, W. C. de Groat, and K.-D. Sievert, “How does neuromodulation work.,” *Neurourol. Urodyn.*, vol. 30, no. 5, pp. 762–5, Jun. 2011.
[184] C. H. Jiang and S. Lindström, “Prolonged enhancement of the micturition reflex in the cat by repetitive stimulation of bladder afferents,” *J. Physiol.*, vol. 517, no. 2, pp. 599–605, 1999.
[185] C. Tai, B. Shen, M. Chen, J. Wang, J. R. Roppolo, and W. C. de Groat, “Prolonged poststimulation inhibition of bladder activity induced by tibial nerve stimulation in cats.,” *Am. J. Physiol. Renal Physiol.*, vol. 300, no. 2, pp. F385-92, Feb. 2011.
[186] X. Su, A. Nickles, and D. E. Nelson, “Comparison of neural targets for neuromodulation of bladder micturition reflex in the rat,” *AJP Ren. Physiol.*, vol. 303, no. 8, pp. F1196–F1206, 2012.
[187] B. C. Gill *et al.*, “Real-Time Changes in Brain Activity during Sacral Neuromodulation for Overactive Bladder,” *J. Urol.*, vol. 198, no. 6, pp. 1379–1385, 2017.
[188] S. Jezernik, J. Wen, N. J. M. Rijkhoff, M. Haugland, J. C. Djurhuus, and T. Sinkjaer, “Whole Nerve Cuff Recordings from Nerves Innervating the Urinary Bladder,” *Proc. 2nd Annu. Conf. Int. Funct. Electr. Stimul. Soc.*, pp. 8–9, 1997.
[189] S. Namasivayam, I. Eardley, and J. Morrison, “A novel in vitro bladder pelvic nerve afferent model in the rat,” *Br. J. Urol.*, vol. 82, pp. 902–905, 1998.
[190] Y. Yu and W. C. de Groat, “Sensitization of pelvic afferent nerves in the in vitro rat urinary bladder-pelvic nerve preparation by purinergic agonists and cyclophosphamide pretreatment,” *AJP Ren. Physiol.*, vol. 294, no. 5, pp. F1146–F1156, 2008.
[191] F. B. Hofmann *et al.*, Eds., *Handbook of experimental pharmacology*, vol. 222, no. April. 2014.
[192] N. G. Ghoshal and R. Getty, “The lumbosacral plexus (plexus lumbosacralis) of the sheep (Ovis Aries),” *N. Z. Vet. J.*, vol. 19, no. 5, pp. 85–90, 1971.
[193] G. Sengul and C. Watson, *Spinal Cord: Regional Anatomy, Cytoarchitecture and Chemoarchitecture*, Third Edit. Elsevier, 2012.
[194] M. Goos, J. Haberstroh, T. Baumann, U. Hopt, G. Ruf, and M. Oberst, “New selective endoscopic sacral nerve root stimulation - an advance in the treatment of fecal incontinence,” *Neurogastroenterol. Motil.*, vol. 23, no. 2, pp. 104–109, 2011.
[195] N. Tanaka, Y. Fujimoto, H. S. An, Y. Ikuta, and M. Yasuda, “The anatomic relation among the nerve roots, intervertebral foramina, and intervertebral discs of the cervical spine.,” *Spine (Phila. Pa. 1976).*, vol. 25, no. 3, pp. 286–291, 2000.
[196] S. Accardo and R. Gonzalez, “Anatomy and Surgical Approaches to the Sacrum,” in *Tumors of the Sacrum*, 2017, pp. 247–254.
[197] D. H. Seo, K. W. Yoon, S. K. Lee, and Y. J. Kim, “Microsurgical excision of symptomatic sacral perineurial cyst with sacral recapping laminectomy: A case report in technical aspects,” *J. Korean Neurosurg. Soc.*, vol. 55, no. 2, pp. 110–113, 2014.
[198] M. D. Unger, T. P. Maus, R. C. Puffer, L. K. Newman, B. L. Currier, and A. S. Beutler, “Laminotomy for Lumbar Dorsal Root Ganglion Access and Injection in Swine,” *J. Vis.*

Exp., no. 128, pp. 1–6, Oct. 2017.
[199] M. Shamir, G. Goelman, and O. Chai, “Postanesthetic Cerebellar Dysfunction in Cats,” *J. Vet. Intern. Med.*, vol. 18, pp. 368–369, 2004.
[200] S. Parithimarkalaignan and T. V. Padmanabhan, “Osseointegration: An update,” *J. Indian Prosthodont. Soc.*, vol. 13, no. 1, pp. 2–6, 2013.